TOPOLOGICAL PHENOMENA IN MAGNETIC THIN FILMS

BY WENBO WANG

A dissertation submitted to the

School of Graduate Studies

Rutgers, The State University of New Jersey

in partial fulfillment of the requirements

for the degree of

Doctor of Philosophy

Graduate Program in Physics and Astronomy

Written under the direction of

Weida Wu

and approved by

_____

_____

_____

_____

_____

New Brunswick, New Jersey

OCTOBER, 2018

© 2018

Wenbo Wang

ALL RIGHTS RESERVED

ABSTRACT OF THE DISSERTATION

Topological phenomena in magnetic thin films

by Wenbo Wang

Dissertation Director: Weida Wu

This thesis covers the study of various topological phenomena in magnetic thin films by utilizing magnetic force microscopy (MFM) at cryogenic temperature. In the first part, we will focus on the magnetic topological insulators (TI) which exhibit quantum anomalous Hall effect (QAHE). The QAHE is of great fundamental interest and potential application because of their dissipationless conduction without the need of external magnetic field. Up to now, this fascinating effect has been achieved in magnetic topological insulators, e.g. Cr- and V-doped $(Bi,Sb)_2Te_3$ thin films, at extremely low temperature ($T < 50\,\mathrm{mK}$). The magnetic inhomogeneity has been proposed as one of the main reasons that limit the temperature for realization of QAHE. In the first part, we will present direct visualization of long-range ferromagnetism in the Cr,V co-doped BST films, by using the MFM and *in-situ* transport measurement. The magnetization reversal process reveals typical ferromagnetic domain behavior, *i.e.* domain nucleation and domain wall propagation. The ferromagnetic behavior at charge neutral point is consistent with the Van Vleck exchange mechanism. Furthermore, this ferromagnetism is robust against significant change in bulk charge carriers, though exchange interaction is enhanced by hole doping. This indicates a significant contribution from the Ruderman-Kittel-Kasuya-Yosida (RKKY) exchange coupling. The

direct evidence of long-range ferromagnetic order eases the concern of the fragility of QAHE due to magnetic inhomogeneity, alleviating the need for ultra-low temperature to achieve full quantization. Our results encourage further exploration of QAHE and related phenomena in magnetically doped topological materials for disspationless conduction at elevated temperature.

In the second part, we will discuss topological Hall effect (THE), which is a real space Berry phase phenomenon originated from scalar spin chirality. The THE has been observed in static spin texture with integer Berry phase (skyrmions)in chiral magnets. Recently, this effect has been also observed in some ultra-thin film systems. The existence of static skyrmions in these systems is still unknown. While thermally driven spin chirality fluctuation in 2 dimensional chiral magnets has been predicted to exist, the resultant THE have not been observed. In this thesis, we report a surprising observation of substantial THE around the ferromagnetic transition T_{C} of ultra-thin films of $SrRuO_3$, a uniaxial ferromagnet with very weak chiral interaction. The temperature, magnetic field, and thickness dependence of THE are in good agreement with our Monte-Carlo simulations, which unambiguously confirms the emergence of net topological charges driven by spin chirality fluctuation. Our discovery opens a new paradigm of exploring the chirality fluctuations with topological Hall transport in 2D ferromagnets. In addition to the chiral fluctuation driven THE (fTHE) in SRO films around T_{C}, the THE is also observed at low temperature in the ultra-thin SRO films, as they approach the critical thickness (3 u.c.). MC simulations indicate the magnetic disorder plays an important role in the low-temperature THE. This disorder-driven THE (dTHE) will be briefly discussed at the end of this thesis.

Acknowledgements

Completing a Ph.D. thesis is not an individual work; rather it involves efforts from other people, to whom I would like to express my sincere gratitude.

First, I would like to give my special thanks to my advisor, Prof. Weida Wu. Weida is always the role model for me as an authentic physicist, who constantly and convincingly conveys a spirit of adventure in regard to research, and an excitement in regard to teaching. Within almost six-year learning and working with him, his diligence and persistence continuously encourage me to focus on the research, no matter what difficulties I encountered. He has the great passion to dig deep into the underlying mechanisms governing interesting physics phenomena, letting me feel the beauty of physics. Consequently, I determined to continue my career as a researcher in condensed matter physics. With his guidance and persistent help, I was able to complete several interesting research projects, which led to several publications in high profile journals and finally this Ph.D. thesis.

Secondly, I would like to thank my research collaborators, who are exceedingly efficient and cooperative. I need to thank Cui-zu Chang, Jagadeesh S. Moodera, Yunbo Ou, Chang Liu, Ke He, Yayu Wang, Julia Mundy, Darrell G. Schlom, Lorenzo Vistoli, Vincent Garcia, Manuel Bibes, Zaiyao Fei, Xiaodong Xu, Zhaoliang Liao, Jun Wang, Matthew W. Daniels, Di Xiao. Without their fruitful collaborations, I would never succeed in any projects.

I also would like to express my thanks to the former and current members in Wu's lab: Yanan Geng, Jing Chen, Jixia Dai, Ying Sun, Fernando Garcia, Maggie Xiao, Zheng Ju, Liqun Yan, Wenhan Zhang, Chen Chen, Paul Sass, Wenbo Ge, Zengle Huang. Thank you guys for helping me both in my research and everyday life, and making the lab a pleasant environment for doing experiments.

It has never been easy for me to live alone in a country thousands of miles away from my hometown. So I would like to thank all of my friends, who make my tedious life more colorful and meaningful: Theodore Siu, Yazhong Wang, Jianpeng Liu, Yue Liu, Bin Gao, Qiang Han, Shucheng Zhu, Xiaocheng Fang, Xianghan Xu, Xiaoli Zhou, Weilu Zhang, De Zeng.

At last, I sincerely express my gratitude to my family for their endless love, support, and understanding. Without their support, it is almost impossible for me to fulfill my dream in the United States.

Dedication

I would like to dedicate this thesis to my parents and grandparents, who raised me, supported me and always have faith in me.

Table of Contents

List of Tables

List of Figures

Chapter 1

Prologue

Topology is a mathematical concept, which describes the properties of manifold that are robust against continuous deformations. A simple example to illustrate the essence of topology is that you can deform a ball into a bowl, however, you can never deform a ball into a donut without poking a hole in it. Herein, the number of holes inside an object, which is termed genus number (g), is an appropriate quantity to describe the topology of the geometry of a three-dimensional object. Mathematically, the genus number is a topological invariant, which can be calculated by taking an integral of the Gauss curvature K over the entire surface:

$$g = 1 - \frac{1}{4\pi} \iint_S K dS \tag{1.1}$$

In the last two decades, the concept of topology has become one of the most popular topics in condensed matter physics. The 2016 Nobel prize in physics was awarded to J. M. Kosterlitz, D. Haldane and D. J. Thouless, as quoted, "for theoretical discoveries of topological phase transitions and topological phases of matter". In condensed matter physics, people use topological invariants to characterize the physical properties of a solid. In the scope of this thesis, I would like to loosely classify the topological phenomena into two categories. One is related to the Berry phase in momentum space, including quantum Hall effect, quantum spin Hall effect, quantum anomalous Hall effect, topological insulators, axion insulators, and *etc.* The other one is related to the Berry phase in real space, *e.g.* topological Hall effect, which originates from the non-coplanar spin textures in real space.

1.1 Berry phase in momentum space

1.1.1 Some basic concepts

In the crystal momentum ($\mathbf{k}$) space, the eigen equation of a crystalline solid with translational symmetry can be written as: $H(\mathbf{r})\psi_{n\mathbf{k}}(\mathbf{r}) = \varepsilon_{n\mathbf{k}}\psi_{n\mathbf{k}}(\mathbf{r})$, where $H(\mathbf{r})$ is the Hamiltonian, $\varepsilon_{n\mathbf{k}}$ is the eigen energy,$\psi_{n\mathbf{k}}(\mathbf{r})$ is the eigen wave function, and n is the band index. Due to the periodic boundary conditions, $\mathbf{k}$ can only take discrete values in the first Brillouin zone(BZ). According to the Bloch's theory, the wave function of a free electron in a period potential should take the form of Bloch states $\psi_{n\mathbf{k}}(\mathbf{r}) = e^{i\mathbf{k}\cdot\mathbf{r}}u_{n\mathbf{k}}(\mathbf{r})$, where $u_{n\mathbf{k}}(\mathbf{r})$ is a periodic function with the periodicity of the lattice constant $\mathbf{T}$,*i.e.*, $u_{n\mathbf{k}}(\mathbf{r}+\mathbf{T}) = u_{n\mathbf{k}}(\mathbf{r})$. The eigen equation ,therefore, can be rewritten as $H_{\mathbf{k}}(\mathbf{r})u_{n\mathbf{k}}(\mathbf{r}) = \epsilon_{n\mathbf{k}}u_{n\mathbf{k}}(\mathbf{r})$, where the Hamiltonian $H_{\mathbf{k}}(\mathbf{r}) = e^{-i\mathbf{k}\cdot\mathbf{r}}H(\mathbf{r})e^{i\mathbf{k}\cdot\mathbf{r}}$ becomes $\mathbf{k}$ dependent. The Berry connection $\mathbf{A}_n(\mathbf{k})$ and Berry curvature $\mathbf{\Omega}_n(\mathbf{k})$ in momentum space can be defined as following[17, 18]:

$$\mathbf{A}_n(\mathbf{k}) = i < u_{n\mathbf{k}}|\nabla_{\mathbf{k}}|u_{n\mathbf{k}} > \tag{1.2}$$

$$\mathbf{\Omega}_n(\mathbf{k}) = \nabla_{\mathbf{k}} \times \mathbf{A}_n(\mathbf{k}) \tag{1.3}$$

The Berry connection $\mathbf{A}_n(\mathbf{k})$ behaves as a vector potential in momentum space. Herein, the Berry curvature $\mathbf{\Omega}_n(\mathbf{k})$ can be regarded as an effective magnetic field in momentum space. The symmetries of a system determine whether it possesses non-zero Berry curvature. In condensed matter systems, there are two important symmetries: spacial inversion symmetry (IS) and time reversal symmetry (TRS). In a system where IS is prevserved,

$$\mathbf{\Omega}_n(\mathbf{k}) = \mathbf{\Omega}_n(-\mathbf{k}) \tag{1.4}$$

In a system where TRS is prevserved,

$$\mathbf{\Omega}_n(\mathbf{k}) = -\mathbf{\Omega}_n(-\mathbf{k}) \tag{1.5}$$

So, if both IS and TRS are preserved, $\mathbf{\Omega}_n(\mathbf{k}) \equiv 0$. In other words, either IS or TRS symmetry has to be broken, in order to have non-zero Berry curvature in momentum space.

For the next part, the relation between the berry curvature and the intrinsic anomalous Hall effect(AHE) will be discussed. We can rewrite Eq. (1.2) in terms of each component of the vector:

$$\mathbf{\Omega}(\mathbf{k}) = \epsilon_{\mu\nu\xi}\partial_{k_\nu} A_\xi(\mathbf{k})\mathbf{e}_\mu \tag{1.6}$$

where $\epsilon_{\mu\nu\xi}$ is the Levi-Civita symbol, and μ, ν, ξ can be treated as the direction indices x, y, z. In the context of quantum mechanics, the position operator $\hat{r}_\mu = i\partial_{k_\mu}$ should be rewrite as $\hat{r}_\mu = i\partial_{k_\mu} - A_\mu(\mathbf{k})$, in the present of vector potential (*i.e.* berry connection) $\mathbf{A}(\mathbf{k})$. The position operators $\hat{r}_\mu$ and $\hat{r}_\nu$ are no longer commutable, $[\hat{r}_\mu, \hat{r}_\nu] = -i(\partial_{k_\mu} A_\nu - \partial_{k_\nu} A_\mu) = -i\epsilon_{\mu\nu\xi}\Omega_\xi$.

Assume an electric field $\mathbf{E}$ is applied to a 3D system, the whole Hamiltonian $H(\mathbf{r}) = H_0(\mathbf{r}) + e\mathbf{E}\cdot\mathbf{r}$. The velocity operator can be written as $\dot{\mathbf{r}} = -(i/\hbar)[\mathbf{r}, H] = -(i/\hbar)[\mathbf{r}, H_0] - (i/\hbar)[\mathbf{r}, e\mathbf{E}\cdot\mathbf{r}]$, having an additional term

$$-(i/\hbar)[\mathbf{r}, e\mathbf{E}\cdot\mathbf{r}] = -(i/\hbar)[r_\mu, eE_\nu r_\nu]\mathbf{e}_\mu = -\frac{e}{\hbar}\epsilon_{\mu\nu\xi}E_\nu\Omega_\xi\mathbf{e}_\mu = -\frac{e}{\hbar}\mathbf{E}\times\mathbf{\Omega}. \tag{1.7}$$

This $\mathbf{E}\times\mathbf{\Omega}$ term is the origin of intrinsic anomalous Hall effect. It's known as the anomalous velocity, first proposed by Karplus and Luttinger in 1954[19].

For a ferromagnetic metal, the TRS is spontaneously broken, giving rise to a non-zero Berry curvature $\Omega_n(\mathbf{k})$ in $\mathbf{k}$ space. The current density $\mathbf{j}$ in the presence of electric field $\mathbf{E}$ takes the form:

$$\mathbf{j} = -e\mathbf{v} = -\frac{e^2}{\hbar}\sum_n \int_{BZ} \frac{d^3\mathbf{k}}{(2\pi)^3} f_n(\mathbf{k})(\mathbf{E}\times\mathbf{\Omega}_n(\mathbf{k})) \tag{1.8}$$

where $f_n(\mathbf{k})$ is the Fermi distribution function. Let's consider a system under a electric field $E_y \neq 0$, but without magnetic field $\mathbf{B} = 0$. The Hall current j_x , which is transverse to E_y, should be

$$j_x = -\frac{e^2}{\hbar}\sum_n \int_{BZ} \frac{d^3\mathbf{k}}{(2\pi)^3} f_n(\mathbf{k})(E_y\Omega_{n,z}(\mathbf{k})) \tag{1.9}$$

Thus, the Hall conductivity σ_{xy} can be written as:

$$\sigma_{xy} = j_x/E_y = -\frac{e^2}{\hbar}\sum_n \int_{BZ} \frac{d^3\mathbf{k}}{(2\pi)^3} f_n(\mathbf{k})\Omega_{n,z}(\mathbf{k}) \tag{1.10}$$

which is a integral of Berry curvature over BZ weighted by the occupation factor $f_n(\mathbf{k})$ of each state. The Berry phase in the momentum space manifests the topological property of the band structure, which could be directly probed by the Hall measurements.

1.1.2 A brief history of the quantum Hall family

In 1980, K.V. Klitzing discovered that the Hall conductance was quantized into integer numbers of e^2/h, when a perpendicular magnetic field was applied to a 2D electron gas (2DEG)[20]. This fascinating phenomenon, which was later called integer quantum Hall effect (IQHE), is a manifestation of the topology of the electronic band structures. The band structures of a 2D electron gas in a strong magnetic field will be quantized into Landau levels, as shown in Fig. 1.1(a). The energy spacing between Landau levels is $\Delta = \hbar\omega_c$, where ω_c is cyclotron frequency of electron, $\omega_c = \frac{eB}{m_e}$. In semiclassical picture, when the Fermi level is tuned inside the energy gap, the electrons are localized into circular orbits, as shown in Fig. 1.1(b). The 2D electron gas is, therefore, insulating inside the bulk. The electrons on the sample edge, however, will bounce off the edge and continue this skipping motion in one direction. This one-way electric conducting channel is called chiral edge mode. It is chiral in the sense that the electrons can only move in one direction, determined by the direction of external magnetic field. Experimentally, the longitudinal resistance drops to zero when the Hall resistance reaches the quantized plateaus, indicating this chiral edge mode is energetically dissipationless. This fascinating phenomenon has potentially great applications in electronic devices.

This IQHE is the first great example of a topological band structure. The Berry phase of a 2D electron gas in the presence of a strong magnetic field can be derived from Eq.

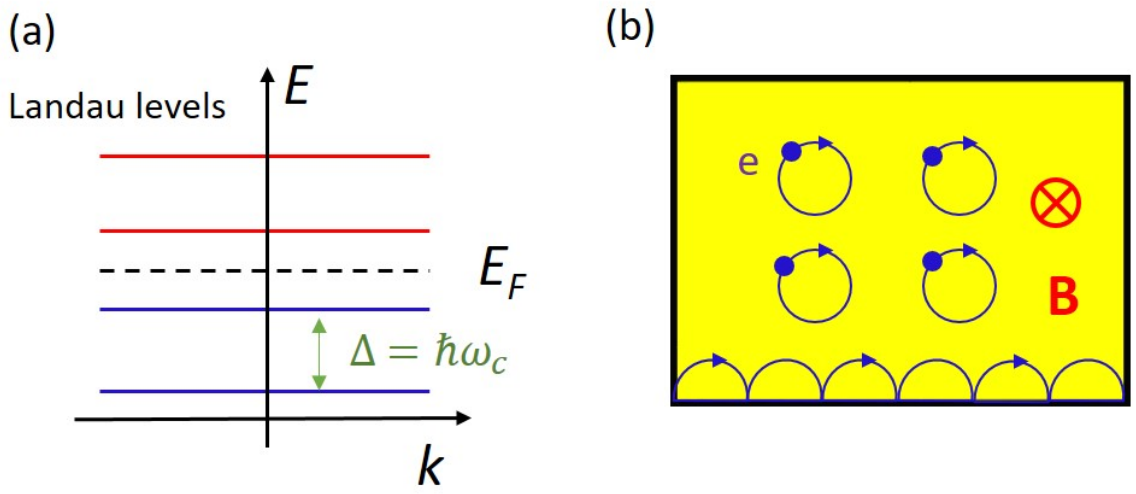

Figure 1.1: **Schematics of the quantum Hall effect.** (a), Schematic of the formation of landau levels in the presence of large external magnetic fields. (b), Schematic of the insulating bulk states and chiral edge states of a quantum Hall insulator.

(1.10) :

$$\sigma_{xy} = \frac{e^2}{\hbar}\int_{BZ}\frac{dk_x dk_y}{(2\pi)^2}\Omega_z(\mathbf{k}) = C\frac{e^2}{h} \tag{1.11}$$

where

$$C = \int_{BZ}\frac{dk_x dk_y}{2\pi}\Omega_z(\mathbf{k}) \tag{1.12}$$

is an integer number, called Chern number (TKNN invariant)[21]. This topological invariant has been widely used to characterize the topologically non-trivial band structure. In the case of IQHE, each LL carries Chern number $C = 1$. So, the Chern number corresponds to the number of filled Landau levels.

The realization of quantum Hall states requires large external magnetic fields, which limits the potential applications. In 1988, Haldane proposed the first theoretical prediction of a QHE system in the absence of external magnetic field, which is later termed quantum anomalous Hall effect(QAHE)[22]. He constructed a tight-binding model of a 2D graphene-like honeycomb lattice with the TRS broken by a hypothetical periodic magnetic flux. The broken TRS will open a mass gap at Dirac point and lead to a Chern insulator with C=1. This toy model demonstrates, for the first time, it is possible to realize a non-trivial band

structure without application of external magnetic field. However, it is very challenging to implement this idea in real materials.

Interesting, the quantum spin Hall effect (QSHE), the cousin of QAHE was realized earlier than the QAHE. A QSH state can be regarded as two copies of QAH states with opposite magnetization directions, *i.e.*, two counter-propagating chiral edge states (helical edge states), as shown in Fig. 1.2(a),(b). The first demonstration of QSHE was realized in the HgTe quantum wells.[1] These materials, now known as 2D topological insulators, belong to a new class of topological materials, different from the Chern insulators. A new topological invariant ν, a Z_2 invariant, was utilized to describe the topology of the band structures of a 2D TI. For a normal insulator or the vacuum, the $\nu = 0$ or even. However, the presence of strong spin-orbital coupling (SOC) can possibly cause the band inversion, which will give rise to a topologically non-trivial band structure with $\nu = 1$ or odd, as shown in Fig. 1.2(c). On the physical boundary of the sample, where the Z_2 invariant varies from 0 to 1, the spin-polarized helical edge states emerge, giving rise to two units of quantum Hall conductance e^2/h, *i.e.*, $\sigma_{xy} = 2e^2/h$, as shown in Fig. 1.2(d). Starting from a 2D TI, it is straightforward to realize QAHE by breaking TRS, which lifts one copy of chiral edge mode. Immediately after the discovery of QSHE, C. Liu *et al.* proposed a theoretical prediction to realize QAHE in a 2D TI by doping magnetic element Mn into the HgTe quantum well systems.[23] Unfortunately, the attempts to introduce ferromagnetism in this quantum well system were unsuccessful.

The idea of Z_2 topological insulator was generalized to a 3-dimension (3D), where the electrons have the freedom to move in a 3D space (k_x, k_y, $k_z \neq 0$)[24]. Up to now, various 3D TIs have been reported, including Bi_xSb_{1-x}[25], Bi_2Se_3[26, 27], Bi_2Te_3[28], Sb_2Te_3[29, 30] and *etc.* Among these 3D TI, Bi_2Se_3 family TIs are the most popular ones, due to the large bulk band gaps and simple surface band structures. Fig. 1.3 shows a schematic of the surface conduction both in real space and momentum space. In the real space, the 3D TI is insulating in the bulk, while conducting on the surface. The surface band structure

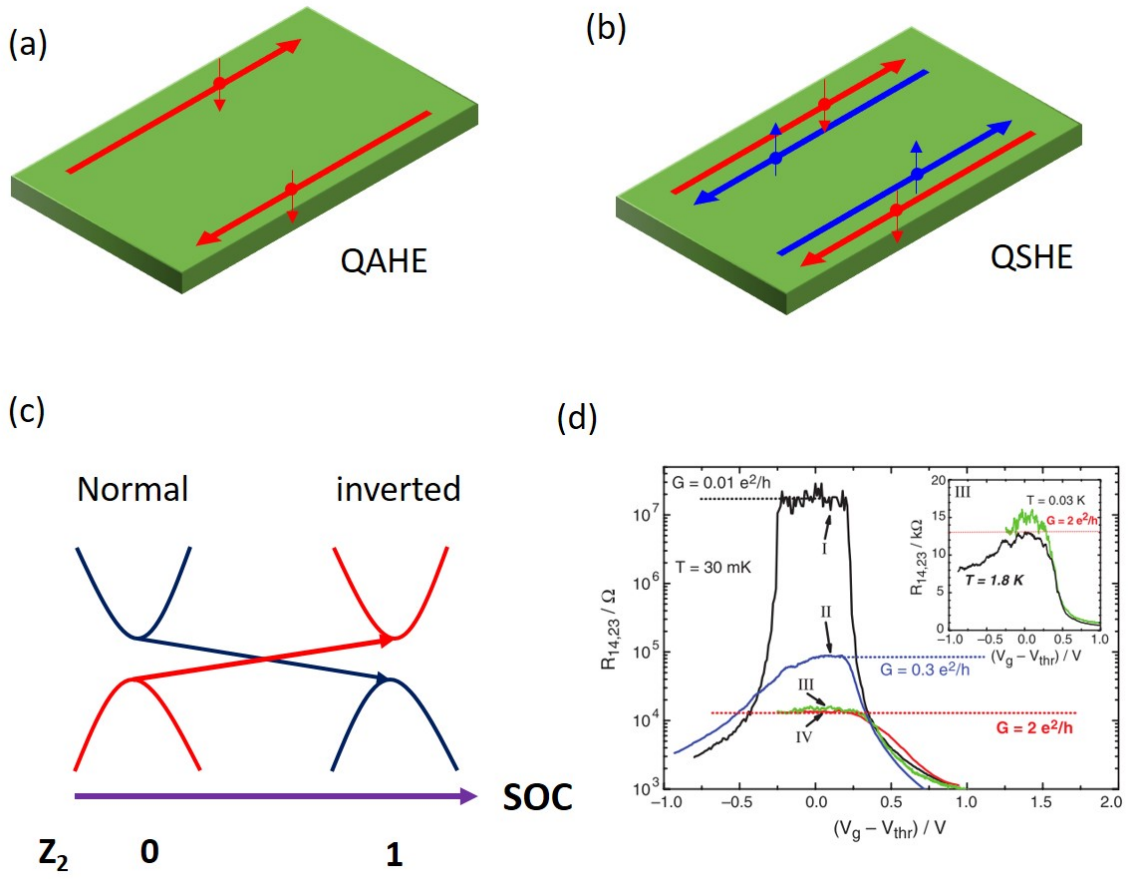

Figure 1.2: **Schematics of the quantum anomalous Hall effect and quantum spin Hall effect.** (a), Schematic of a quantum anomalous Hall insulator with spin-polarized chiral edge states. (b), Schematic of a 2D topological insulator (QSH insulator) with spin-polarized helical edge states. (c), Schematic of a transition from a normal band to a inverted band, as SOC increases. (d), Quantized Hall conductance observed in a 2D TI, the HgTe quantum well system. Adapted from Ref.[1].

in the momentum space shows a Dirac-cone-like structure, similar to the bulk band of a graphene. Different from a graphene, the surface states (SS) of a 3D TI have the spin-momentum locking, *i.e.*, the direction of the spin always perpendicular to the direction of the momentum. This feature enables the 3D TIs to have wide potential applications in spintronics.

By introducing ferromagnetism in a 3D TI, the TRS is spontaneously broken, which opens up a mass gap at the Dirac point. The size of the mass gap is proportional to the exchange coupling J. If the Fermi level is tuned into this mass gap and bulk states

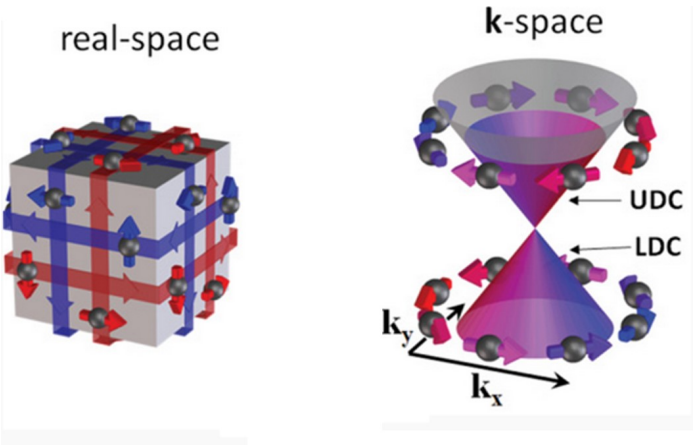

Figure 1.3: **Schematics of the surface states conduction of a 3D TI in both real space and momentum space.** Adapted from Ref.[2].

are absent, the QAHE with one chiral edge state can be realized, as shown in Fig. 1.4. Up to now, there are two main routes to introduce ferromagnetism in a 3D TI, including doping magnetic elements into 3D TI and using magnetic proximity effect in a ferromagnetic insulator (FMI)/TI heterostructure. In the scope of this thesis, I will focus on the magnetic TI systems, where the QAHE has been experimentally realized. The ferromagnetism has been introduced in various magnetic TI systems, namely Mn-doped Bi_2Te_3[31], Cr- and V-doped Sb_2Te_3[32–34], Cr-doped Bi_2Se_3[35] and etc. However, it is challenging to realize QAHE in these systems. Firstly, it is not trivial to find a TI with the Fermi level very close to the Dirac point. Since Bi_2Te_3 is a hole-doped and Sb_2Te_3 is electron-doped, one way to resolve this issue is to dope Bi into a Sb_2Te_3 TI. The second critical issue is to control the thickness of 3D TI samples. It should be as thin as possible to localize other dissipative bulk and surface states. But at the same time, it should not be so thin that the top and bottom surfaces hybridize with each other. Finally, in 2013, the QAHE was firstly observed in 5QL Cr-doped $(Bi,Sb)_2Te_3$ (BST) thin films by C. Chang *et al.*[3] and later confirmed by other groups[36, 37].

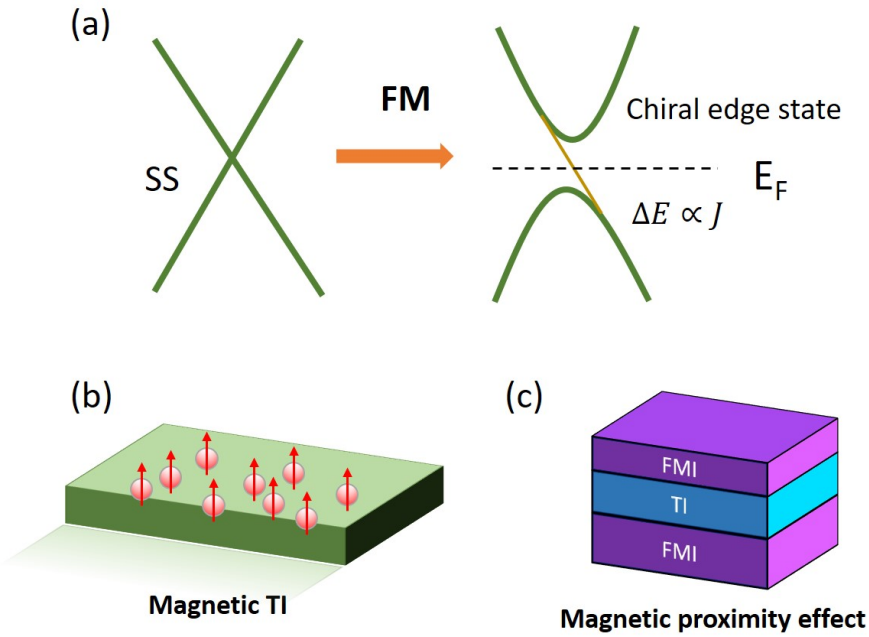

Figure 1.4: (a) Introducing ferromagnetism in a 3D TI opens up a mass at Dirac point. Two routes to introducing ferromagnetism (FM) in a 3D TI, including magnetic doping (b) and magnetic proximity effect(c).

1.1.3 Experimental observations of quantum anomalous Hall effect

Fig. 1.5 shows the transport data of 5QL $Cr_{0.15}(Bi_{0.1}Sb_{0.9})_2Te_3$ at various back-gate voltages[3]. When the Fermi level is tuned to the Dirac point (V_g^0=-1.5V), at 30 mK, the Hall resistance ρ_{yx} is quantized into h/e^2 at zero field and remains constant under external magnetic field, except around coercive field H_C when the film undergoes a transition from one quantum state to the other. At the same time, the longitudinal resistance ρ_{xx} dramatically deceases, indicating one dissipationless conducting channel at sample edge. The ρ_{xx} finally drops to zero at high magnetic field $\sim$ 10 T. Although this QAH state is quite robust against high magnetic field, it is very fragile at elevated temperature. Activation energy estimated from the temperature dependence of the longitudinal conductance is $\sim$ 0.1 K.

Soon after the discovery of QAHE in Cr-doped BST films, a more robust QAHE was achieved in V-doped BST films[38]. Compared Cr-doped systems, V-doped ones have a larger magnetic anisotropy K, resulting in a larger coercive field ($H_C \sim$ 1 T at 120 mK)

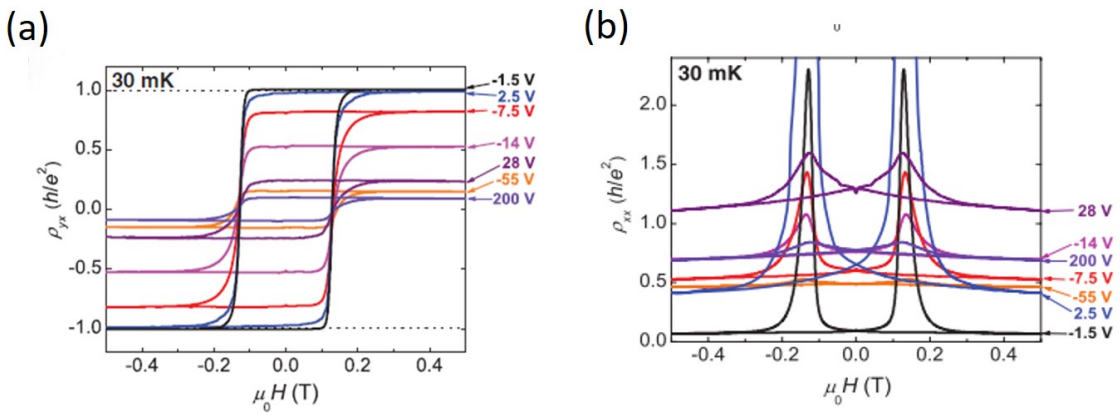

Figure 1.5: **Quantum anomalous Hall effect in 5 QL $(Bi_{0.1}Sb_{0.9})_2Te_3$.**(a)Hall resistance ρ_{yx} loops at various back-gate voltages.(b) Longitudinal resistance ρ_{xx} loops at various back-gate voltages. Adapted from Ref.[3]

and a higher Curie temperature T_C. Still, ultra-low temperature ($T < 50\,\text{mK}$) is needed to achieve full quantization. Therefore, it is imperative to understand the origin of the need of ultra-low temperature for full quantization.

Magnetic inhomogeneity has been proposed to be one of the main factors that limit the QAH temperature. Disordered ferromagnetic or superparamagnetic behavior, and electronic inhomogeneity have been reported in Cr-doped BST thin films[4, 5, 39, 40]. Since the mass gap is proportional to the strength of exchange interaction, the reduced QAH temperature is likely limited by the regions with the weakest exchange[4, 40]. While modulation doping of Cr was shown to improve the quantization temperature in penta-layer thin films [41], it is unclear whether it really reduces magnetic inhomogeneity. On the other hand, recent angle-resolved photoemission spectroscopy (ARPES) studies of V-doped BST thin films suggest that the valence band maximum (VBM) is above the Dirac point[42]. Therefore, ultra-low temperature is needed to localize the bulk states near the Dirac point along with sufficient disorders[43]. These mechanisms of lowering quantization temperature indicate that Cr and V co-doping could be a viable way to reduce magnetic inhomogeneity while enhancing the mobility gap of localized states. Empirically, alloy doping is commonly known as an effective route to improve ferromagnetic order in a diluted magnetic semiconductor[44, 45].

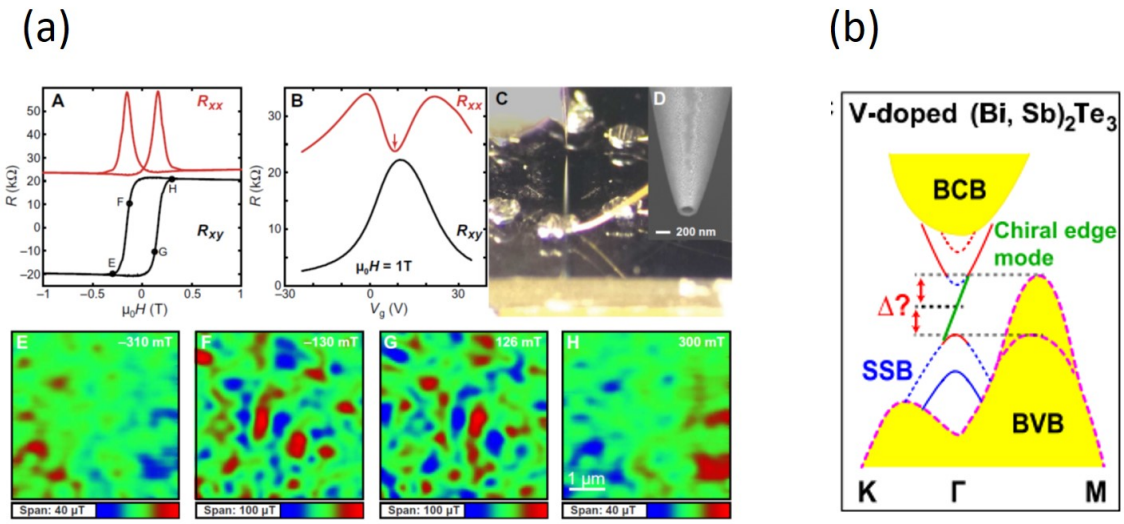

Figure 1.6: **Possible scenarios that limit QAH temperature:** (a) Superparamagnetism observed in Cr-doped BST films. Adapted from Ref.[4].(b)ARPES data shows VBM is above Dirac point in V-doped BST films. Adapted from Ref.[5]

Indeed, enhanced QAH temperature was observed in Cr- and V-doped BST thin films[14].

1.1.4 Axion insulators

Another theoretical interpretation of the QAHE originates from the axion term. In a 3D TI, the Maxwell equation has to be modified by an additional term called axion term, which gives rise to a unique electromagnetic response[46–48].

$$S_\theta = \frac{\theta}{2\pi}\frac{e^2}{h}\int d^3x dt \mathbf{E}\cdot\mathbf{B} \tag{1.13}$$

where $\mathbf{E}$ and $\mathbf{B}$ are the conventional electric and magnetic field inside an insulator and θ is the dimensionless pseudoscalar parameter describing the Z_2 topology of the insulator. For a trivial insulator, $\theta = 0$, while for a TI, $\theta = \pi$. As the TRS is preserved, θ can take a value of either 0 or π. As the TRS is broken, the surface states of a TI will be gapped out and give rise to a half-integer of quantum anomalous Hall effect on the TI surface. The existence of axion term can lead to a variety of quantum phenomenon, including quantum anomalous Hall effect[3, 36, 37], the quantized magneto-optical effect[49, 50], the topological

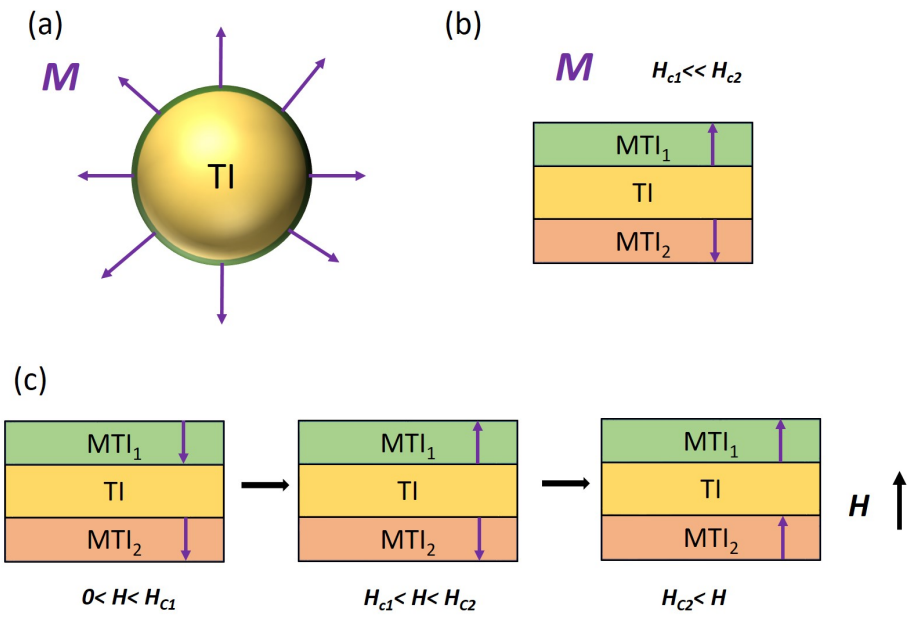

Figure 1.7: **Realization of axion insulating state.** (a) An ideal model of an axion insulator. (b)Realization of axion insulating state with MTI/TI/MTI heterostructure. (c)The process of preparation of axion insulating state by applying magnetic field.

magneto-electric effect (TME)[3, 36, 37], and the magnetic monopole[51]. The TME effect is the quantized version of magnetoelectric effect, *i.e.* the quantized response of the electric polarization to the applied magnetic fields or the quantized response of the magnetization to the applied electric fields. The realization of TME requires three conditions: (1) The TI should be in a 3D regime. (2) All the surface states should be gapped out. (3) The TRS should be preserved in the bulk with $\theta = \pi$. The insulator which satisfies all these conditions is called axion insulator.

Fig. 1.7(a) shows an ideal model of an axion insulator: a 3D TI is shaped into a sphere and the surface layer of the TI possess a magnetization perpendicular to the surface, always pointing outward. However, it is very challenging to fabricate a device like this in practice. Inspired by the idea of realizing QAHE in the MTI thin films, people try to use MTI/TI/MTI heterostructures to achieve the axion insulating state, as shown in Fig. 1.7(b). The top and bottom MTIs should have antiparallel magnetization alignment to eliminate the chiral edge states.

A viable method to realize the antiparallel magnetization alignment is to use two different MTIs with a substantially different coercive field, *e.g.*, $H_{C1} \ll H_{C2}$. First, the QAH state can be prepared by using a sufficiently large negative magnetic field. As the magnetic field is swept to positive fields, the tri-layer structure will undergo a two-step transition: the top layer with smaller H_C will reverse first and the bottom layer will reverse subsequently. The intermediate state is the axion insulating state with the antiparallel magnetization alignment.

The first experimental indication of the axion insulator is reported in the heterostructure of BST thin films with modulation doping of Cr[52]. It was claimed that the vertical asymmetry of the heterostructure causes a slight difference of the coercive field of the top and bottom layers. At extremely low temperature $\sim 40\,\mathrm{mK}$, the Hall loop exhibits a zero Hall conductance plateau (ZHCP) in the range ($0.12\,\mathrm{T} < H < 0.15\,\mathrm{T}$). However, the ZHCP is not a direct proof of the axion insulating state. In fact, the ZHCP has been observed in a QAH system, due to the metal-to-insulator transition during the reversal process where the magnetic domains form[53–55]. Experimentally, it is easier to measure resistance than conductance. Thus, the Hall conductance (σ_{xy}) comes from measured Hall resistance (ρ_{yx}) and longitudinal resistance (ρ_{xx}). The σ_{xy} can be expressed as a function of ρ_{yx} and ρ_{xx}:

$$\sigma_{xy} = \frac{\rho_{yx}}{\rho_{xx}^2 + \rho_{yx}^2} \tag{1.14}$$

If the system is very insulating, *i.e.*, $\rho_{xx} \ll \rho_{xy}$, the Hall conductance will approach zero $\sigma_{xy} \approx 0$, even though $\rho_{yx} \neq 0$. Shortly afterward, Mogi *et al.*[56] and Xiao *et al.*[15] independently observed more convincing axion insulating state in the tri-layer heterostructure Cr-doped BST/BST/V-doped BST. As mentioned in the Chapter 1.1.3, the Cr-doped BST and V-doped BST films have substantially different coercive fields. By controlling the thickness of the spacing TI layer (BST layer) to minimize the interlayer exchange coupling, it is very likely to realize the antiparallel magnetization alignment. Although zero Hall resistance plateau has been observed in the heterostructure[15], the magnetic characterization

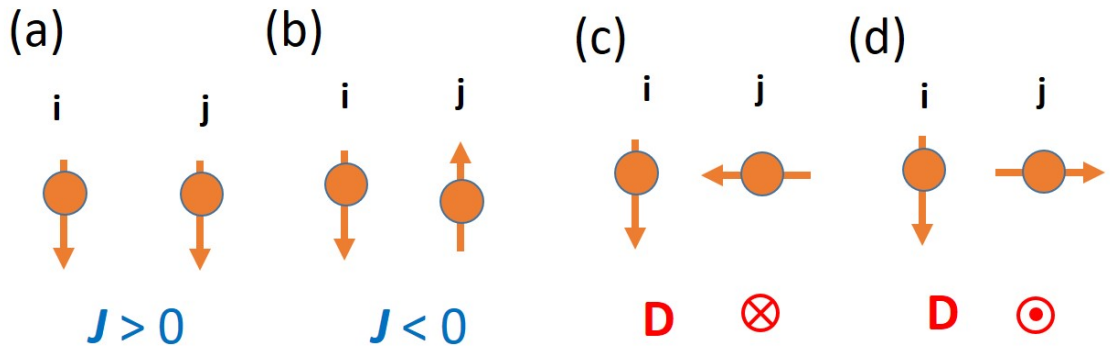

Figure 1.8: (a)(b)The neighboring spin alignment in the presence of exchange coupling J. (c)(d)The neighboring spin alignment in the presence of DM interaction $\mathbf{D}$.

of the magnetization alignment provides the direct evidence.

1.2 Berry phase in real space

For this section, we will discuss the Berry phase in real space, related to the non-coplanar spin textures. To have an overall view of this field, I would like to start from one of the origins of the non-coplanar spin textures, i.e., the antisymmetric off-diagonal exchange term, Dzyaloshinskii-Moria (DM) interaction. The related materials, called magnetic skyrmions, including both B20 compounds and multi-layer structures, will also be discussed briefly. In the end, the topological Hall effect, which reflects the presence of the non-coplanar spin textures, will be discussed in detail.

1.2.1 Twisting of spins

In magnets with Heisenberg exchange coupling J, the neighboring spins prefers co-linear alignment, due to the presence of the free energy term:

$$E_J = -J(\mathbf{S}_i \cdot \mathbf{S}_j) \tag{1.15}$$

where i and j correspond to the site index of the neighboring spins. Depending on the sign of J, the neighboring spins have parallel or antiparallel alignment, leading to a ferromagnetic

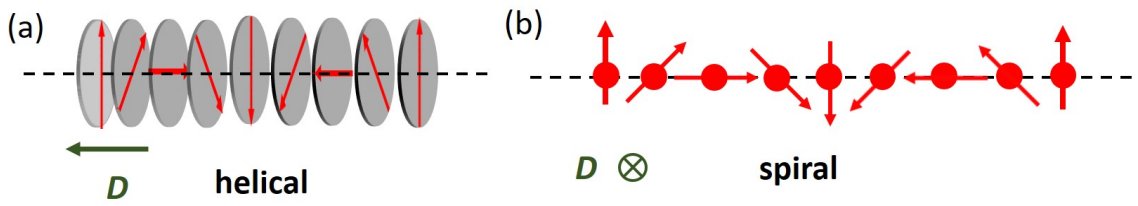

Figure 1.9: Formation of helical (a) and spiral (b) ordering in the presence of DM interaction, depending on the direction of **D**.

or antiferromagnetic ordering

In 1954, Dzyaloshinsky proposed a phenomenological theory of the spin-orbital coupling and the magnetic dipole interaction to explain the weak ferromagnetism in certain antiferromagnetic crystals, *e.g.*, $\alpha-Fe_2O_3$, $MnCO_3$ and $CoCO_3$[57]. Based on Dzyaloshinsky's idea, in 1960, Moriya developed a general theory of the anisotropic superexchange interaction including the spin-orbital coupling. This antisymmetric interaction, later coined the DM interaction, prefers the perpendicular alignment of the neighboring spins[58]. The free energy term due to DM interaction can be expressed as:

$$E_D = -\mathbf{D} \cdot (\mathbf{S}_i \times \mathbf{S}_j) \tag{1.16}$$

The emergence of the DM vector **D** requires the local inversion symmetry broken and a finite SOC. More specifically, the local inversion symmetry broken determines the direction of **D** and SOC determines the magnitude of **D**. The competition between J and D will result in non-collinear spin structure. In a simple 1D model, a helical or spiral ordering will form. The wavelength of the helical (or spiral) ordering is determined by the ratio of D/J. The total energy of two neighboring spins in the presence of J and D can be written as:

$$E = -(JS^2 \cos\theta + DS^2 \sin\theta) \tag{1.17}$$

where θ is the angle between neighboring spins. The total free energy E can be minimized with $\tan\theta = D/J$. When $D \ll J$, $\theta \approx D/J$. Given the lattice constant a of the 1D chain,

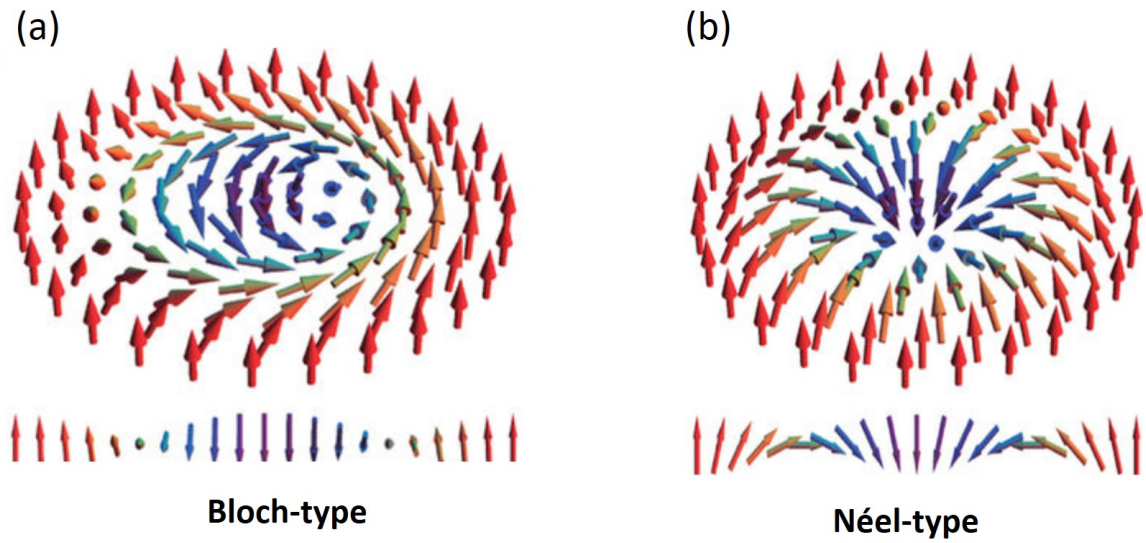

Figure 1.10: The schematic of a Bloch-type (a) and Néel-type (b) skyrmion. Adapted from Ref.[6].

the wavelength of the helical order should be $\lambda \approx 2\pi aD/J$. In real systems, the wavelength usually falls in the range 1 nm∼100 nm. If this helical wave with single wavevector **q** can propagate in a 2D system, it will form a helical phase with stripe domains. If the 2D system has multiple-**q** helical waves propagating in the plane, in certain circumstances, it is possible to form skyrmion lattices. An individual skyrmion is a topologically stable spin texture, where the spins point in all the directions in the 3D space, wrapping a sphere. Depending on the direction of **D**, it will form two types of skyrmions, namely Bloch-type and Néel-type, which are the 2D version of helical and spiral order.

1.2.2 Formation of skyrmions in B20 compounds and metallic multilayers

B20-type transition-metal silicides and germanides, *e.g.*, MnSi, (Fe,Co)Si and FeGe, are helical magnets with cubic but non-centrosymmetric crystal structure. This class of materials are famous for the existence of a mysterious 'A phase', later known as the skyrmion phase. The so-called 'A phase' was first identified in MnSi[59] and $Fe_{1-x}Co_xSi$[60] single crystals by using neutron scattering. The neutron diffraction pattern shows a six-fold symmetry, indicating the formation of a 2D hexagonal skyrmion lattice. The 'A phase' exists in a

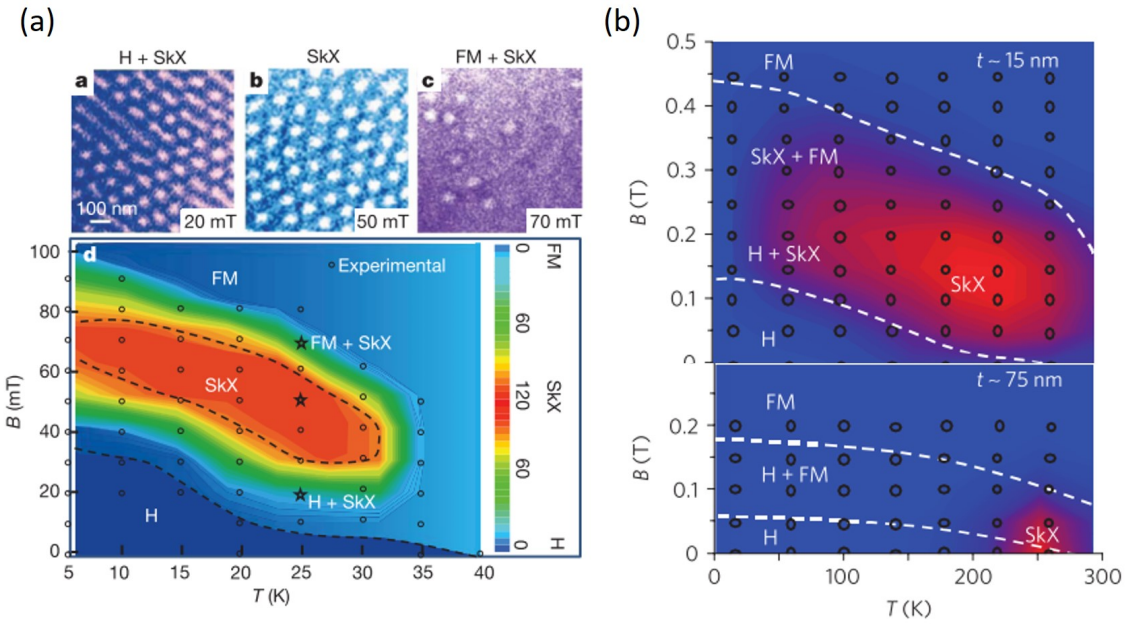

Figure 1.11: (a) Phase diagrams of magnetic structure in a thin film of $Fe_{0.5}Co_{0.5}Si$. Spin textures were observed by busing Lorentz TEM. As the magnetic field applied, the thin film evolves from helical phase (H) to skyrmion phase (SkX) and finally to ferromagnetic phase (FM). Adapted from Ref.[7]. (b) Thickness dependence of the SkX phase diagram of FeGe thin films. The SkX extends to a lower temperature for thinner films. Adapted from Ref.[8].

small region of the phase diagram just below Curie temperature T_C in the presence of a small perpendicular magnetic field. The hexagonal skyrmion lattice can be interpreted as the superposition of three helical phase with the wave vector $\mathbf{Q}$ 120° to each other. So sometimes it is called 3-$\mathbf{Q}$ phase.

Shortly after, this hexagonal skyrmion lattice was observed in real-space, using the Lorentz transmission electron microscopy (TEM) in various B20 compounds[7, 8]. The Lorentz TEM images show a helical ground state with the formation of stripe domains. As a small magnetic field applied, these stripes break up into small skyrmion bubbles, forming a hexagonal skyrmion lattice. Higher magnetic fields will erase these skyrmion bubbles and the sample finally enters the ferromagnetic phase with the spins all aligned by the external magnetic field. A small magnetic field is usually required to stabilize the skyrmion phase. Since the net magnetization of skyrmion is non-zero, applying a small magnetic field will

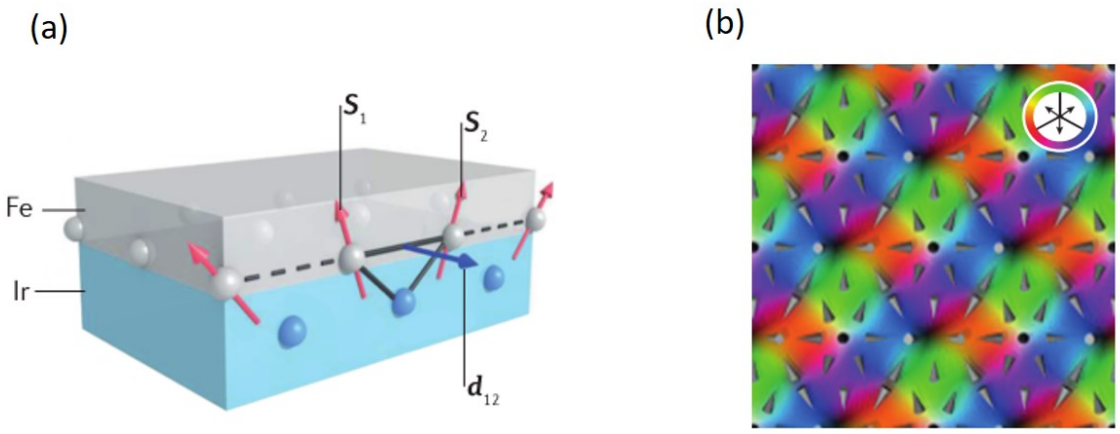

Figure 1.12: **Formation skyrmions in a multilayer structure.** (a) DM interaction on the interface of Fe and Ir layers. Adapted from Ref.[9].(b) Square skyrmion lattice detected by spin-polarized STM. Adapted from Ref.[10].

gain some Zeeman energy, making the skyrmion phase energetically favorable. In addition, thermal fluctuation also helps the stabilization of skyrmion phase. Since skyrmion phase is a high-entropy phase, high temperature usually favors the formation of skyrmion lattice. The thickness dependence of the phase diagram indicates the skyrmion phase can be extended to low temperature in thin samples. This indicates a crossover between 2D to 3D skyrmion formation. In the 3D case, the wave vector is smaller than thickness. The conical phase with the wave vector Q parallel to the perpendicular external magnetic field is energetically favorable at low temperature. Such conical phase, however, is suppressed in a 2D case. That explains why the skyrmion phase is able to extend to low temperature in thin samples.

In addition to the B20 skyrmions, the skyrmions can be artificially created in the metallic multilayers. These multilayers usually consist of a layer of 3d ferromagnet (*e.g.* Fe, Co) to provide magnetism and a layer of 5d element (*e.g.* Ir, Ta, and Pt) to provide strong SOC[9]. On the interface, where the inversion symmetry is broken, a large DM interaction $[\mathbf{D}_{ij} \propto \lambda_{soc}(\hat{\mathbf{z}} \times \hat{\mathbf{r}}_{ij})]$ is induced, leading to the formation of Néel-type skyrmions. Various real-space magnetic imaging techniques have been used to visualize the skyrmion lattice in metallic multilayers, *e.g.*, spin-polarized scanning tunneling microscopy (STM)[10], scanning

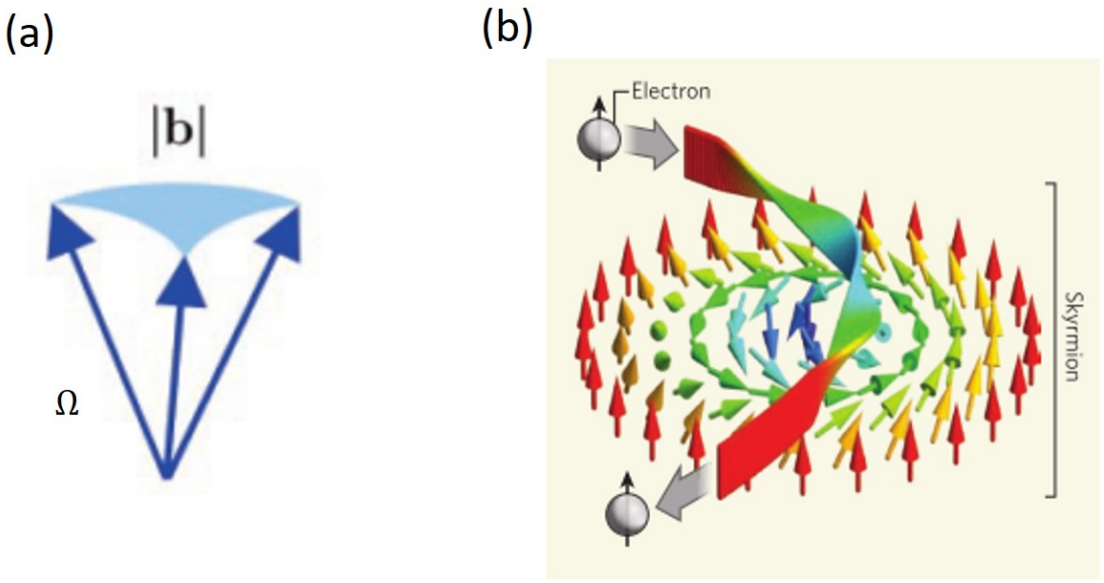

Figure 1.13: **Schematics of the origin of topological Hall effect :** (a) The spin triad subtends a solid angle Ω, which provides an effective magnetic field **b** in real space. Adapted from Ref.[11].(b) The electron, passing through a skyrmion, is deflected due to the Berry phase acquired.

transmission X-ray microscopy (STXM)[61] and magnetic force microscopy (MFM)[62]. These skyrmions have wide potential applications in memory and logic devices, because they can be easily moved by electric current, compared to the domain walls. Extensive studies have been done to write and read these skyrmions[9].

1.2.3 Topological Hall effect in skyrmion systems

The skyrmions are of great interests to physicists, not only due to the wide potential applications, but also due to the exotic topological properties. The concept of Berry phase due to spin chirality was proposed by Taguchi *et al.* in 2001[11]. As an electron hops on non-coplanar spin sites, it will acquire a complex phase factor (Berry phase) that acts as an effective magnetic field, which will contribute to Hall effect.

Fig. 1.13(a) shows three non-coplanar spins which subtend a solid angle Ω. The Berry phase acquired by the electron hopping on these three spins is equal to this solid angle Ω:

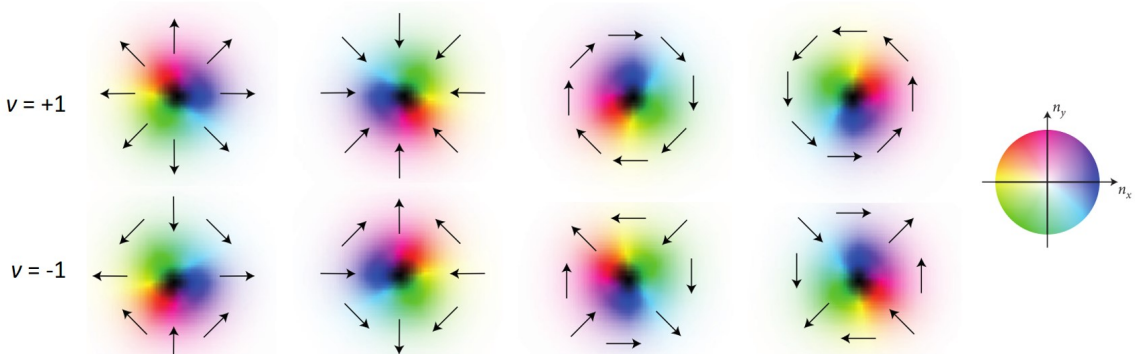

Figure 1.14: **The spin textures of skyrmions ($v = +1$) and anti-skyrmions ($v = -1$).** The arrows indicate the direction of the in-plane spin components, and the brightness indicates the normal component to the plane, with white denoting the up direction and black the down direction. Here, $p = +1$ for all skyrmions depicted. Adapted from Ref.[12].

$$\Omega = \int d^2 r \mathbf{n} \cdot (\partial_x \mathbf{n} \times \partial_y \mathbf{n})) \tag{1.18}$$

where $\mathbf{n}$ is the unit vector of local spins. The topological charges (TC)or winding numbers in terms of magnetic skyrmions can be expressed as:

$$Q = \frac{\Omega}{4\pi} \tag{1.19}$$

where $|Q| = 1$ for one skyrmion, as the spin textures of one skyrmion cover 4π solid angle. The sign of the Q, however, is non-trivial. Taking into account the symmetry of the skyrmion, the unit vector $\mathbf{n}$ can be written as:

$$\mathbf{n}(\mathbf{r}) = (\cos\Phi(\varphi)\sin\Theta(r), \sin\Phi(\varphi)\sin\Theta(r), \cos\Theta(r)) \tag{1.20}$$

Using the polar coordinates $\mathbf{r} = (r\cos\varphi, r\sin\varphi)$, we can rewrite topological charge Q as:

$$Q = \frac{1}{4\pi}\int_0^\infty dr \int_0^{2\pi} d\varphi \frac{d\Theta(r)}{dr}\frac{d\Phi(\varphi)}{\varphi}\sin\Theta(r) = \frac{1}{4\pi}[\cos\Theta(r)]_{r=0}^{r=\infty}[\Phi(\varphi)]_{\varphi=0}^{\varphi=2\pi} \tag{1.21}$$

The $p = [\cos\Theta(r)]_{r=0}^{r=\infty}/2$ is defined as the polarity of a skyrmion. It essentially depends on the out-of-plane component of the spins. Suppose the spins point up at $r \to \infty$ while

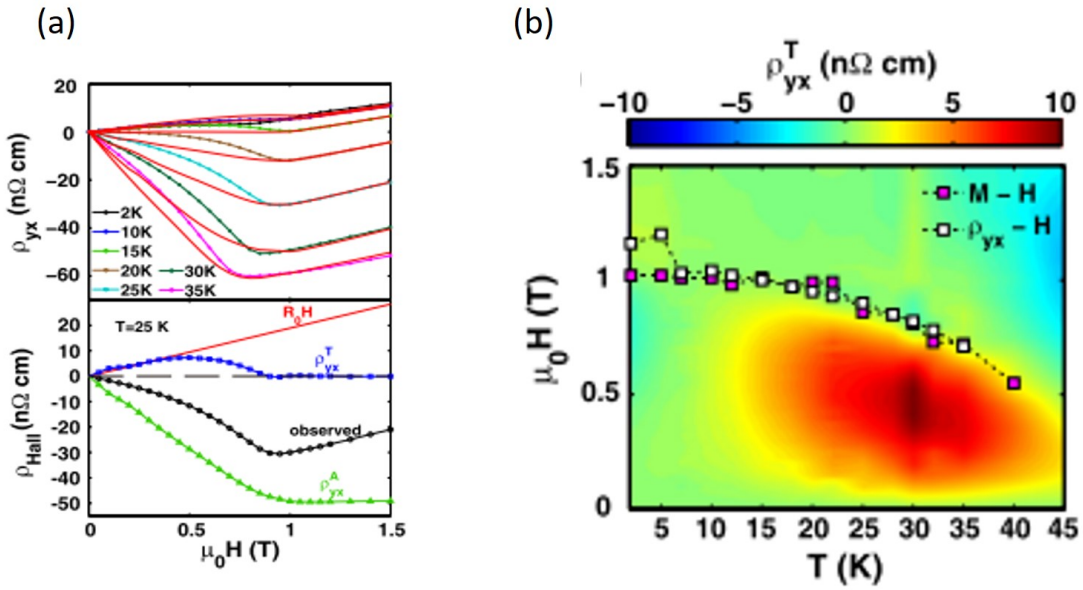

Figure 1.15: (a) ρ_{yx} of 50 nm MnSi film at various temperature. The decomposition of Hall data into R_0H, ρ_{yx}^A and ρ_{yx}^T at 25 K. (b) The contour map of ρ_{yx}^T of 50 nm MnSi film. Adapted from Ref.[13].

they point down at $r = 0$. Then, $p = +1$. It can be negative one, if the spins point down at $r \to \infty$ while they point up at $r = 0$. On the other hand, $v = [\Phi(\varphi)]_{\varphi=0}^{\varphi=2\pi}/2\pi$ is usually called vorticity of a skyrmion, which is relative to in-plane component of the spins. Looking at the in-plane component of the spins along the perimeter of a skyrmion clockwisely. If the spins also rotate clockwisely, the skyrmion has positive vorticity, *i.e.* $v = +1$. Otherwise, the skyrmion has negative vorticity, *i.e.* $v = -1$. This type of skyrmions is also called anti-skyrmion. Figure 1.14 shows the cartoon pictures of the spin textures of skyrmions ($v = +1$) and anti-skyrmions ($v = -1$), with $p = +1$[12]. The topological charges Q determined by the product of p and v, *i.e.*, $Q = p \cdot v$.

The topological charges of one skyrmion will provide an effective magnetic field, quantitatively equal to one flux quanta ϕ_0, giving

$$\mathbf{b} = Q \cdot \boldsymbol{\phi_0} \tag{1.22}$$

This effective magnetic field leads to the so-called topological Hall effect (THE), in

analogy to, the ordinary Hall effect caused by external magnetic field. Thus, the topological Hall resistivity can be written as:

$$\rho_{yx}^{T} = PR_0 n(Q)\phi_0 \tag{1.23}$$

where P is the spin polarization, R_0 is the ordinary Hall effect and $n(Q)$ is the density of topological charges. This relation has been widely used to quantitatively estimate the THE in skyrmion systems. In fact, THE has been observed in many skyrmion systems, *e.g.* MnSi[13, 63], FeGe[64]. For a long time, THE is regarded as a hallmark of formation of static skyrmions. Recently, THE has been reported in some ultra-thin films, such as Cr-doped $(Bi_{1-x}Sb_x)Te_3$[65], Mn-doped Bi_2Te_3[66], CrTe[67], and $SrIrO_3/SrRuO_3$ bilayer structures[68, 69]. Although the formation of Néel-type skyrmions was claimed in these papers, there is no direct evidence from the real-space imaging. It is urgent to combine the magnetic imaging techniques and *in-situ* transport measurements to investigate the origin of the THE in these ultrathin magnetic films.

Chapter 2

Methods

In this chapter, we will present a powerful scanning probe technique, called magnetic force microscopy (MFM) to characterize magnetic domain structures in thin film systems. An introduction of the basic principles of MFM will be discussed first. Next, a sophisticated homemade MFM setup to simultaneously measure MFM and in-situ transport will be discussed. At the end, two examples will be demonstrated to exhibit the high sensitivity of our setup and the reliability to characterize M-H loops by using our setup.

2.1 Introduction to MFM

Understanding the magnetism in materials is at the heart of condensed matter physics. By introducing magnetism into certain systems, some exotic phenomena can be achieved. For example, the possible coupling of ferromagnetic order and ferroelectric order may lead to giant magnetoelectric effect[70, 71]. Introducing ferromagnetism in the topological insulators can lead to many fascinating quantum phenomena, such as quantum anomalous Hall effect[3], and topological magnetoelectric effect[15]. In the presence of DM interaction or frustration in a ferromagnet, more complex spin textures can be achieved, which might lead to more intriguing properties, such as topological Hall effect[63], the spin liquids[72], and the Devil's staircase[73]. In these exotic magnetic systems, where magnetic domains form, the net magnetization is averaged out, which is unlikely to be detected by the bulk measurements, such as superconducting quantum interference device (SQUID). On the other hand, studying the magnetism at nanoscale is very useful to understand the properties of small magnetic objects, such as skyrmions, magnetic domain walls, and magnetic quantum

dots.

Up to now, many magnetic imaging techniques enable the real-space characterization of magnetism at nanoscale. For example, MFM[74], scanning SQUID techniques[75] and nitrogen-vacancy (NV) magnetometry[76] directly measure the magnetic field or field gradient. Other optical techniques for magnetic imaging are also very popular, such as magneto-optical Kerr effect (MOKE) microscopy [77] and scanning transmission X-ray microscopy (STXM)[61]. Among them, MFM, which is a relatively traditional technique, is still widely used in the field of condensed matter physics and material sciences. Although it may not have the same high-sensitivity as scanning SQUID and lateral resolution as NV magnetometry, MFM can be used in a wider range of temperature and magnetic fields. This enables the study of a wide variety of magnetic materials. Compared to those optical techniques, MFM usually has a better lateral resolution. In addition, it is a table-top microscope, which can be realized in most labs without the need of the synchrotron-based sources. Moreover, the optical method, by utilizing Kerr effect to probe magnetism, is an indirect magnetometry, which effectively measures the AC anomalous Hall effect.

The MFM, built on the basis of atomic force microscopy (AFM), belongs to the scanning probe techniques[78]. AFM was invented by Binnig *et al.* in 1986[79], shortly after the invention of scanning tunneling microscopy (STM)[80], which is a powerful technique to image individual atoms. Although the traditionally AFM does not have the atomic resolution, it is less sensitive to surface contaminations and mechanical vibrations, therefore can be used at ambient conditions. The basic principle of AFM is to detect the atomic force, which typically consists of long-range attractive van der Waals force and short-range repulsive Coulomb force. Different operation modes are utilized for different purposes. For topographic imaging, a contact mode and tapping mode are often used. In the contact mode, the AFM tip, on the end of a cantilever, is pressed on the sample surface. The repulsive atomic force causes the bending of the cantilever. Such small deflection can be accurately detected by various methods, *e.g.*, the laser-based position sensors, piezoresistive cantilevers,

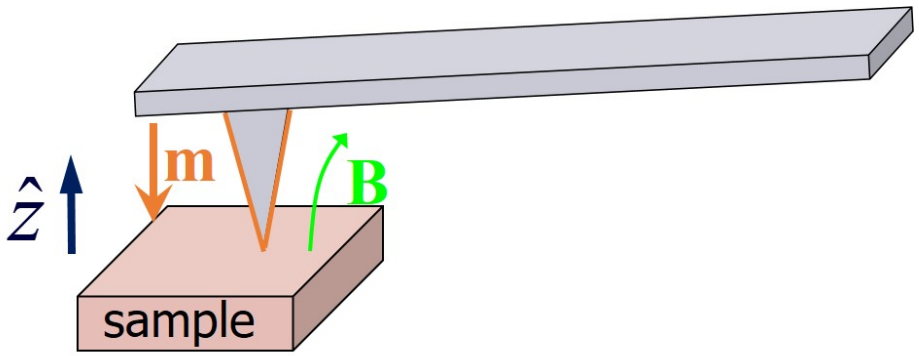

Figure 2.1: **Schematics of a standard MFM setup.**

quartz crystal tuning forks, and interferometric sensors. During the scanning process, the deflection keeps constant, by controlling the z position of the cantilever. The mapping of z value manifests the topography of the surface. In addition to topographic imaging, the contact modes are widely used in other scanning probe techniques, such as piezoresponse force microscopy (PFM)for imaging ferroelectric domains and conductive atomic force microscopy (cAFM) for probing the local electric conductance. The drawback of contact mode is the contact force exerted is relatively high. This usually causes the damage of a soft sample surface and the reduced lifetime of the AFM tips. To circumvent this problem, a tapping mode (or intermittent-contact mode) is used for topographic imaging. The AFM tip is driven at its resonance frequency. The amplitude of the oscillation is used as the feedback parameter in this case. This mode is more commonly used for topographic imaging, due to the less damage to both the samples and AFM tips. A standard AFM setup can have high lateral resolution $\sim$10 nm and high vertical resolution $\sim$1 nm. If the tip is lifted above the surface $\sim$50 nm, the short-range atomic force is negligible and the long-range interactions, such as magnetic force or electric force, dominate. The MFM or electrostatic force microscopy (EFM)[81] operates in this so-called non-contact mode.

Figure 1.15 shows a schematic MFM setup. A standard procedure of MFM imaging is the interleave mode: it first scans the topography in the tapping mode, then the tip is lifted to maintain the constant height from the surface in the non-contact mode. This interleave

mode minimize the topographic contamination in the MFM images, which is widely used to scan a rough surface. However, scanning the topography sometimes alters the magnetic domain structures, if the sample is magnetically soft and tip moment is large. For instance, the magnetic thin films usually have relatively lower magnetic moments per unit area, which requires a large moment tip to probe. If the thin films have a coercive field H_C smaller than the stray field near the magnetic tip, the topographic scanning can modify the domain patterns, leading to some artifacts in the MFM images. Thus, the interleave mode is not preferable. In the thin film samples, the surface is usually quite flat, with a roughness $\sim$ 1 nm. Thus, the *in-situ* topographic imaging is not necessary. However, the slope of the sample surface should still be determined. The typical scanning procedure for a thin film sample can be described by two steps: first, scan the topography of the sample surface in the other area, away from the area for MFM scanning; next, lift the tip up and move the tip to the desired area. During the MFM imaging, the tip always follows the slope of the surface to maintain a constant lift height.

The interaction between the sample and magnetically coated AFM tip can be approximated by a dipole-dipole interaction[82]. The interaction energy U can be expressed as the dot product of the moment of either dipole into the field from the other dipole:

$$U = -\mathbf{m} \cdot \mathbf{B} \tag{2.1}$$

where $\mathbf{m}$ is the magnetic moment of the tip and $\mathbf{B}$ is the magnetic stray field from the sample. Since the magnetic moment of the tip usually points to z direction, the equation can be rewritten as $U = -m_z \cdot B_z$. The interaction between the sample and the tip is the gradient of the interaction energy:

$$F = -\nabla U = m_z \cdot \frac{\partial B_z}{\partial dz} \tag{2.2}$$

This force acting on the tip has a z dependence. Such force gradient effectively changes the spring constant of the cantilever, leading to the resonance frequency shift. Consider the

cantilever as a spring with a spring constant k_0. The total force F_t acting on the cantilever includes both restoring force and magnetic force:

$$F_t = -k_0 \cdot z + F = -k_0 \cdot z + F_0 + F_z' \cdot z + \frac{1}{2} F_z'' \cdot z^2 + ... \tag{2.3}$$

Take into account the 1st order term of F, the magnetic force gradient effectively changes the spring constant of the cantilever: $k = k_0 - F_z'$. The resonance frequency of the cantilever can be expressed as

$$f = \frac{1}{2\pi}\sqrt{\frac{k}{m}} = \frac{1}{2\pi}\sqrt{\frac{k_0 - F_z'}{m}} \approx \frac{1}{2\pi}\sqrt{\frac{k_0}{m}}(1 - \frac{F_z'}{m}) = f_0(1 - \frac{F_z'}{2k_0}) \tag{2.4}$$

So the resonance frequency shift Δf caused by magnetic force gradient can be expressed as:

$$\frac{\Delta f}{f_0} = -\frac{F_z'}{2k_0} = -\frac{m_z}{2k_0}\frac{\partial^2 B_z}{\partial z^2} \tag{2.5}$$

The MFM measures the resonance frequency shift Δf of the cantilever, which is proportional to the second derivative of the stray magnetic field in z direction. The up and down magnetic domains lead to opposite MFM signals, *i.e.*, attractive (repulsive) force decreases (increases) resonance frequency.

2.2 Homemade cryogenic magnetic force microscope with *in-situ* transport

Figure 2.1 shows a schematic picture of the homemade cryogenic MFM system. This instrument is able to perform magnetic imaging in a wide temperature ($2.5\,\mathrm{K} \sim 300\,\mathrm{K}$) with *in-situ* high magnetic field ($8.0\,\mathrm{T}$) and high voltage ($1.0\,\mathrm{kV}$) The scanning probe has a compact design, a circular cylinder with an 8-inch height and a 1-inch base radius, and it is suitable for liquid helium experiments. The apparatus is interfaced with a Nanonis controller and Phase Locked Loop. The deflection of the cantilever is sensed by the piezo-resistive

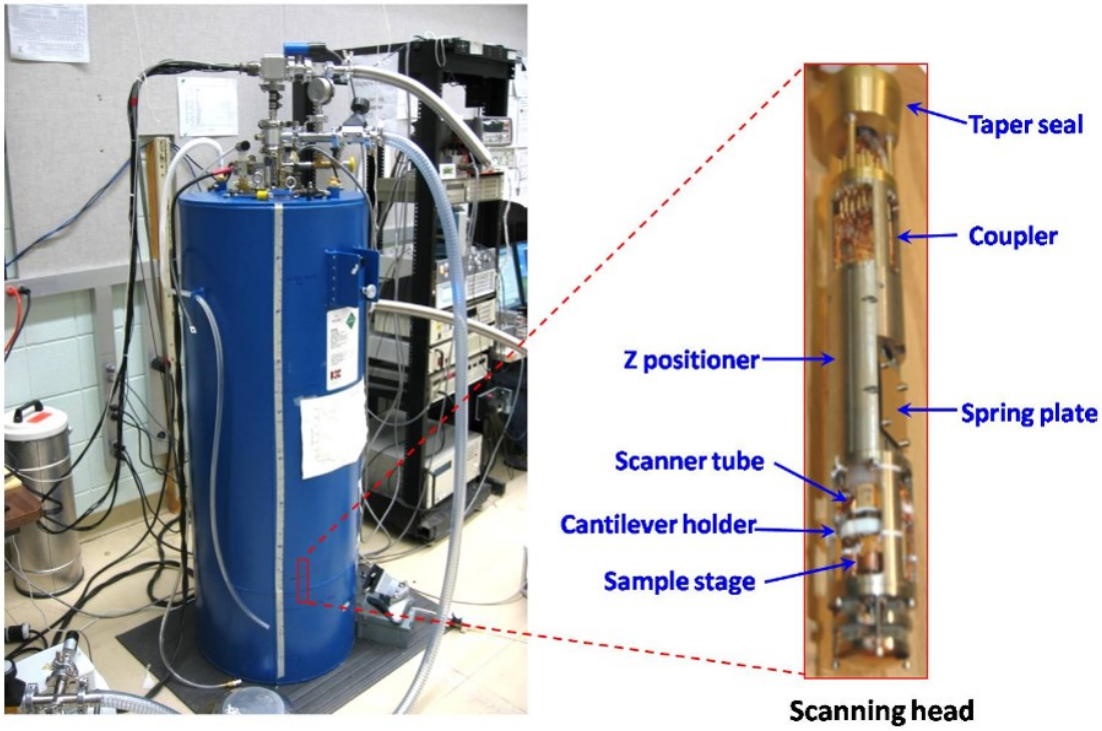

Figure 2.2: **Schematics of home-made cryogenic MFM setup.**

method, *i.e.*, the stress-induced resistivity change of piezo-resistive material integrated on the cantilever[83]. The cantilever resistance is precisely balanced by a Wheatstone bridge. The resistance difference between the cantilever and reference is amplified by 2000 times via a differential amplifier. This signal is then fed to the Nanonis controller as the deflection signal. The magnetic tips are prepared by coating the bare tips with nominally 100 nm Co film using electron-beam evaporation, which is capped with 2 nm Cr to prevent oxidation. The magnetic tip is usually magnetized by a strong magnet at ambient condition before MFM measurements.

In an itinerant ferromagnet, the transport properties depend on the magnetism, examples include magnetoresistance, anomalous Hall effect, and topological Hall effect. In order to study the interplay between the transport properties and the magnetism, it is imperative to combine the MFM and *in-situ* transport measurements. Figure 2.2 shows a schematic picture of the Hall bar device of the magnetic topological insulator thin films fabricated for

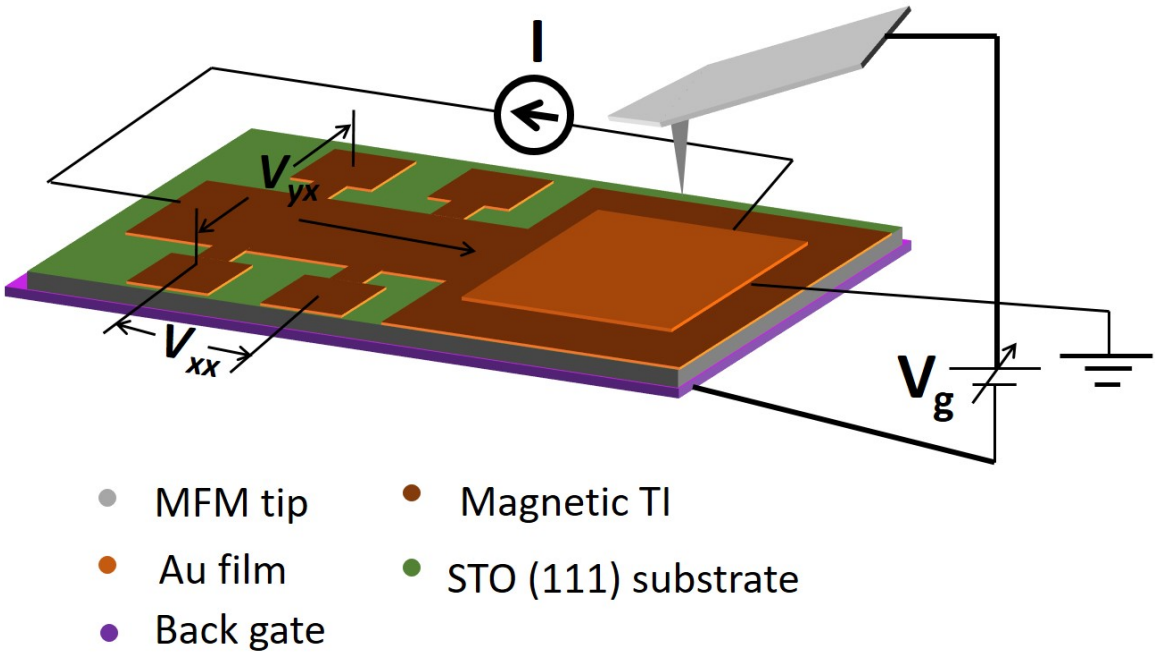

Figure 2.3: **Schematics of a Hall bar device of magnetic TI thin films for MFM and *in-situ* transport measurements.**

MFM and *in-situ* transport measurements. The film was scratched by hand into a Hall bar shape connected with a large square-like area for MFM measurements. An approximately 15 nm Au film layer was deposited on the square area to eliminate electrostatic interactions between the sample and the magnetic tip, as both of them are grounded. The Hall resistance and longitudinal resistance were measured by standard lock-in techniques with an alternating current of 5 μA modulated at 314 Hz. The magnetic TI was grown on the $SrTiO_3$ substrate, which is an incipient ferroelectric with divergent dielectric constant at low temperature, *e.g.* $\varepsilon_r \sim 10000$ at 6 K[84]. Applying a back gate voltage ($\sim$ 100V) to the STO substrate can result in substantial change of the charge carrier density.

2.3 Characterization of M/M_S using cryogenic MFM

The MFM technique, which measures the local magnetic field gradient, can not quantitatively characterize the magnetization (M). It is a powerful technique to characterize the

domain structures of ferromagnets with perpendicular anisotropy. By estimating the up and domain distribution, the local normalized magnetization (M/M_S) can be obtained, where M_S is the saturation magnetization. The shape of M-H and the coercive field (H_C) can be estimated by plotting the M/M_S as a function of magnetic field (H). A typical concern on SPM studies is whether the MFM images are representative of the bulk properties. So in this section, I will discuss the MFM studies of weak ferromagnetic hexagonal $LuFeO_3$ films and ferromagnetic $SrRuO_3$ films. The SQUID data and anomalous Hall data are quantitatively consistent with the obtained M/M_S-H loops, justifying MFM as a suitable technique to characterize M/M_S in these magnetic systems.

2.3.1 Visualizing weak ferromagnetic domains in multiferroic hexagonal ferrite thin film

Multiferroic materials, which possess at least two ferroic properties among ferroelectricity, ferromagnetism, and ferroelasticity, are of great interests to condensed matter physicists due to the possible giant cross-couplings between these three order parameters[85–88] . The cross-coupling between ferroelectric and ferromagnetic orderings gives rise to large magnetoelectric (ME) effect, i.e., electric polarization induced by magnetic field or magnetization induced by electric field [89–91]. The ME effect has a wide range of applications in electric field controlled magnetic memories [92, 93], magnetic field sensors[94, 95], and tunable microwave filters[96, 97]. Extensive studies have been carried out on transition-metal oxide multiferroics, such as $BiFeO_3$[98–102] and hexagonal rare-earth manganites (h-$RMnO_3$, R=Y, Dy-Lu)[103–107]. Recently, the $h-LuFeO_3$ thin film, a member of hexagonal ferrites (h-$RFeO_3$, R=Y, Dy-Lu), has been claimed to be another multiferroic material, with potential ME coupling[108–114]. Similar to hexagonal manganites, hexagonal ferrites exhibit both ferroelectricity and antiferromagnetism. h-$LuFeO_3$ is, however, more appealing because of its weak ferromagnetic ground state with canted moment ($\sim 0.02\,\mu_B$/f.u.) and its higher magnetic ordering temperature ($T_N \approx 147\,K$)[112], presumably due to the stronger

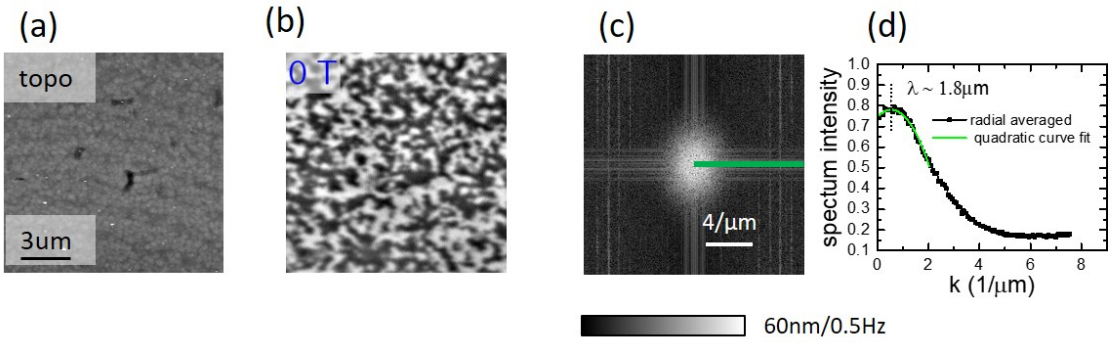

Figure 2.4: (a) Topographic and (b) MFM image of the h-$LuFeO_3$ film at 50 K after zero field cooling. (c) Fourier Transformation (FT) image of (b), the virgin domain state shows a ring-like feature at the center. (d) k dependence of radial FT spectrum intensity (azimuthally averaged) shows a single peak at $\lambda \sim 1.8\,\mu$m. The green curve is the quadratic curve fit around the peak.

exchange interaction between Fe^{3+} moments[115]. The tiny canted moment makes it challenging to image the weak ferromagnetic domains. In this section, we will discuss the direct visualization of weak ferromagnetic domains in h-$LuFeO_3$ films, using our home-made cryogenic MFM system. For more details, please check PRB paper[116].

The h-$LuFeO_3$ films were grown by oxide MBE onto (111)-oriented yttria-stabilized cubic zirconia (YSZ) substrates. A ~ 50 nm thick Au film was deposited on the surface of the $h-LuFeO_3$ film to eliminate electrostatic interaction between the sample and the magnetic tip. The MFM images were taken in a non-contact mode with a scanning plane ~ 40 nm above the sample surface. Figure 2.4 shows the topographic and MFM images of the h-$LuFeO_3$ film at 50 K after zero-field cooling (ZFC). The topographic image shows a flat, Au-capped surface with a roughness ~ 3.5 nm. As shown in Fig. 2.4(b), a labyrinth-like domain structure was observed in the virgin domain state, which is typical for thin films of uniaxial ferromagnets[117, 118]. The characteristic domain size of h-$LuFeO_3$ is estimated by Fourier transform (FT) analysis of the virgin domain state, as shown in Fig.2.4(c). The image shows a ring-like feature in the center, indicating an isotropic domain size distribution. The azimuthally averaged FT spectral intensity as a function of wave vector k is shown in Fig. 2.4(d), which exhibits one broad peak slightly above zero. Using a quadratic

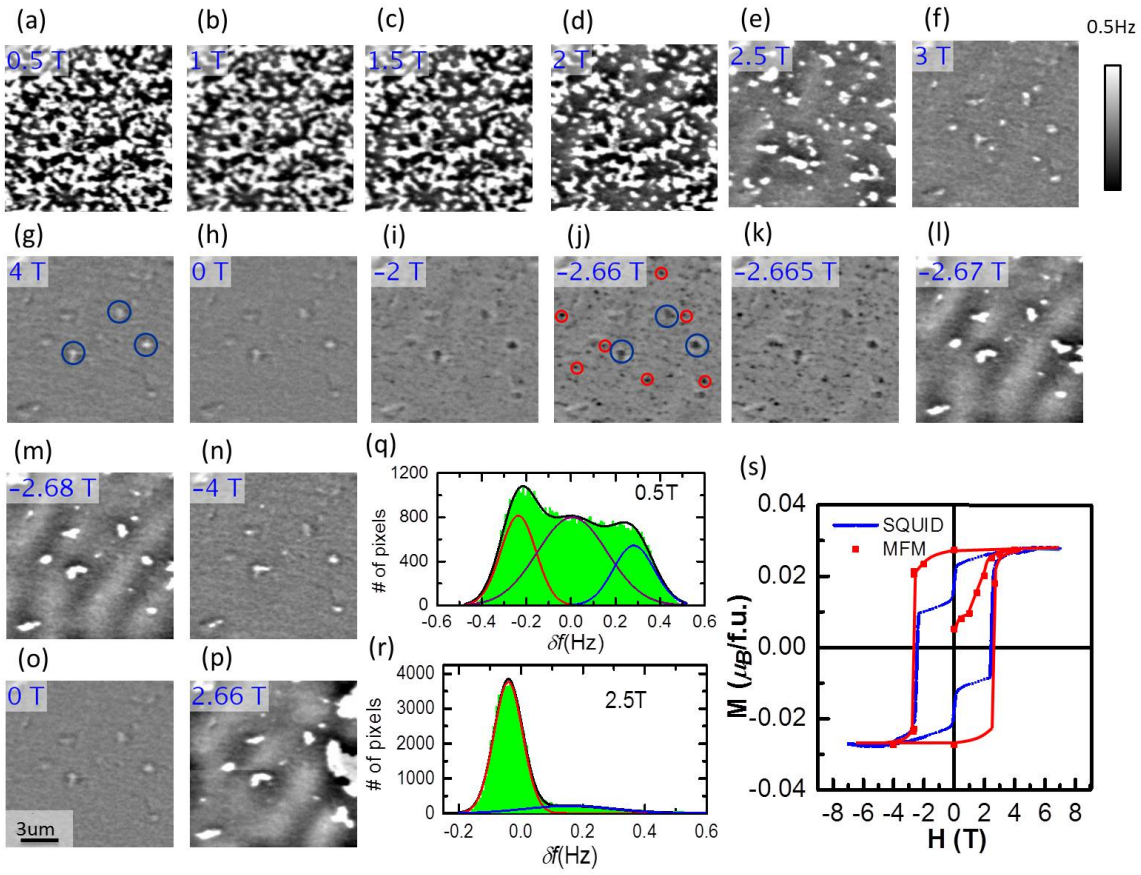

Figure 2.5: (a)-(p) MFM images (50 K) taken at various magnetic fields after zero field cooling. The zero field MFM image is shown in Fig. 2.4(b). The magnetic field value of each image is labeled at the top left corner. The grey scale of the MFM images is 0.5 Hz. Representative defect sites and nucleation sites are labeled by blue and red circles, respectively. Histograms of the MFM images at 0.5 T (q) and 2.5 T (r) reveal multiple peaks. The profiles can be fit by a combination of either three (q) or two (r) Gaussian peaks. The bins number was set to be 100. (s)M-H curves measured by SQUID (blue) and MFM (red) show $H_C \sim 2.66$ T (50 K).

fit, the peak was found at $\lambda \sim 1.8\,\mu$m, indicting the characteristic domain size $\sim 0.9\,\mu$m of the 200 nm thick h-$LuFeO_3$ film after ZFC. The apparently random domain configuration indicates a significant amount of nucleation and pinning sites. To characterize these properties, the magnetization saturation and reversal process is visualized with MFM.

Figure 2.5 shows the evolution of the weak ferromagnetic domains as a function of the external magnetic field. The zero field MFM image is shown in Fig. 2.4(b). A magnetic field of 0.5 T is not strong enough to modify the domain pattern, as shown in Fig. 2.5(a).

The domain contrast was enhanced ~ 1.8 times, likely due to the enhancement of the MFM tip moment. Further increasing the field results in a gradual reduction of the anti-parallel domains due to depinning of the domain boundaries. As shown in Fig. 2.5(b)-(g), the dark regions expand and the bright regions shrink with increasing external magnetic field. The film saturates at 4 T because a further increase of the external magnetic field does not cause any change of the domain pattern. Note that some weak domain contrast is still visible in the saturated state. Those features are not correlated with topography. So they are magnetic defects (labeled by blue circles), likely due to local structural or composition imperfections. The film stays in the saturated state even after the field is ramped down to zero, as shown in Fig. 2.5(h). The domain contrast is reversed at -2 T, indicating the tip moment was switched. This also verifies that the domain contrast observed in the saturated state is magnetic. On the other hand, no reversed domain was found in the scanned area. Maintaining a single domain state under reverse field is a telltale sign of a strong uniaxial anisotropy in h-$LuFeO_3$, which prevents nucleation of reversed domains. At -2.66 T, many bubble-like reversed domains (labeled by red circles) were observed in the MFM image, as shown in Fig. 2.5(j). This confirms a relatively dense concentration of nucleation sites randomly distributed over the film. Further decreasing the magnetic field by 5 mT induces little change in the domain pattern. From -2.665 T to -2.670 T, the domain pattern changes dramatically. At -2.67 T, the film is dominated by down domains with only a small amount of up domains (bright contrast) pinned by defect sites. The sharp transition from positive magnetization to negative magnetization state suggests a relatively narrow distribution of domain wall pinning strength at 50 K. Further decreasing the magnetic field to -4 T aligned all of the magnetic domains, *i.e.*, the film was saturated, showing identical features as the positively saturated state, further corroborating that they are magnetic defects. Interestingly, a similar domain pattern was observed at positive coercive field H_C, as shown in Fig. 2.5(p), which indicates a strong memory effect.

A histogram analysis was also carried out on these field-dependent MFM images ($256 \times$

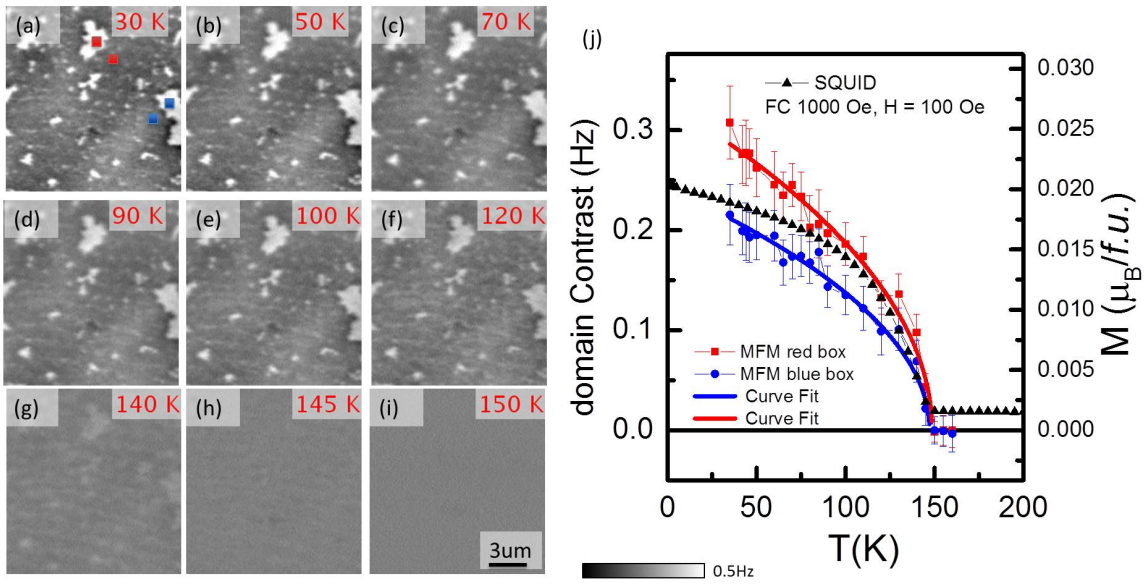

Figure 2.6: (a)-(i)Zero-field MFM images of induced weak ferromagnetic domains were measured at various temperature. (i)Temperature dependence of domain contrast from MFM images (red and blue boxes) is consistent with that of magnetization measured by SQUID (black triangles), indicating a second-order ferromagnetic transition at $T_C \approx 147\,\mathrm{K}$. It can be fitted by a mean-field-like behavior (blue and red curves).

256 pixels) to estimate the population of up and down domains. The histogram curves of near-zero magnetization multi-domain state, Fig. 2.5(a)-(d), can be fitted by a superposition of three Gaussian peaks, as shown in Fig. 2.5(q). Left (red curve) and right (blue curve) peaks correspond to up and down weak ferromagnetic domains. The middle peak (purple curve) may originate from the domain wall contributions. The histogram profiles of the polarized domain states (*e.g.*, 2.5 T), however, exhibit a two-peak feature, due to a reduced contribution from domain walls. We used the peak height to estimate the population of up and down domains. The normalized magnetization M/M_S therefore can be estimated from $(N_\uparrow - N_\downarrow)/(N_\uparrow + N_\downarrow)$, where M_S is the saturation magnetization and $N_\uparrow$ ($N_\downarrow$) is the population of up (down) domains. From the normalized magnetization, the M vs. H loop (red curve) can be plotted from the MFM images. It shows a square-like hysteresis loop of a hard ferromagnet with a strong uniaxial anisotropy. The virgin curve shows that domain walls start to depin at $\sim 1.5\,\mathrm{T}$, much lower than the coercive field. This indicates a relatively

wider pinning strength distribution of the virgin domain state at 50 K. In contrast, the sharp transition at the coercive field suggests that the nucleation sites are also strongly pinning. The *M-H* data from a SQUID measurement (blue curve) on the same film shows a two-step behavior. The first step is absent in the MFM data, possibly due to a small amount of paramagnetic impurity phase (*e.g.*, Fe_3O_4). The second step at $H_C \sim 2.660$ T is in good agreement with that inferred from our MFM data. This provides compelling evidence that our MFM observation reflects the representative domain behavior of the *h*-$LuFeO_3$ thin films grown by MBE.

The strong pinning preserves the domain configuration to high temperature. This enables an investigation of the temperature dependence of the magnetization via MFM domain contrast. The temperature dependence of the pinned weak ferromagnetic domains are shown in Fig. 2.6 (a)-(i). As the temperature increases, the domain contrast becomes weaker and weaker. At 150 K, the domain contrast disappears, indicating a phase transition from a weak ferromagnetic state to a paramagnetic state. The temperature dependence of the domain contrast exhibits a mean-field-like behavior,as shown in Fig. 2.6 (j), which can be fitted by $M = A(T_C - T)^{0.5}$. The fitting results give the $T_C \sim 148$ K and $M_S \sim 0.242$ Hz. The *M-T* curve from SQUID shows $T_C \approx 147$ K, in good agreement with MFM data, and $M_S \sim 0.02\,\mu_B$/f.u., which can be used as a good calibration of our MFM data. The conversion factor between magnetization $\boldsymbol{M}$ and MFM data is $0.0826\,\mu_B$/f.u./Hz. Given the ~ 21 mHz noise level of our MFM system, the sensitivity limit of our setup to probe magnetic moments in this 200 nm thin film is $0.002\,\mu_B$/f.u. (*i.e.*, 1 nm thick film it would be $0.4\,\mu_B$/f.u.).

2.3.2 Visualization of ferromagnetic domains in SrRuO3 thin film

The $SrRuO_3$ (SRO), which shows itinerant ferromagnetism, has been extensively studied for over 40 years[119]. Recently studies of $SrRuO_3$ focus on the exotic transport properties and strong correlations. For instance, although it is a Fermi liquid at low temperature, it

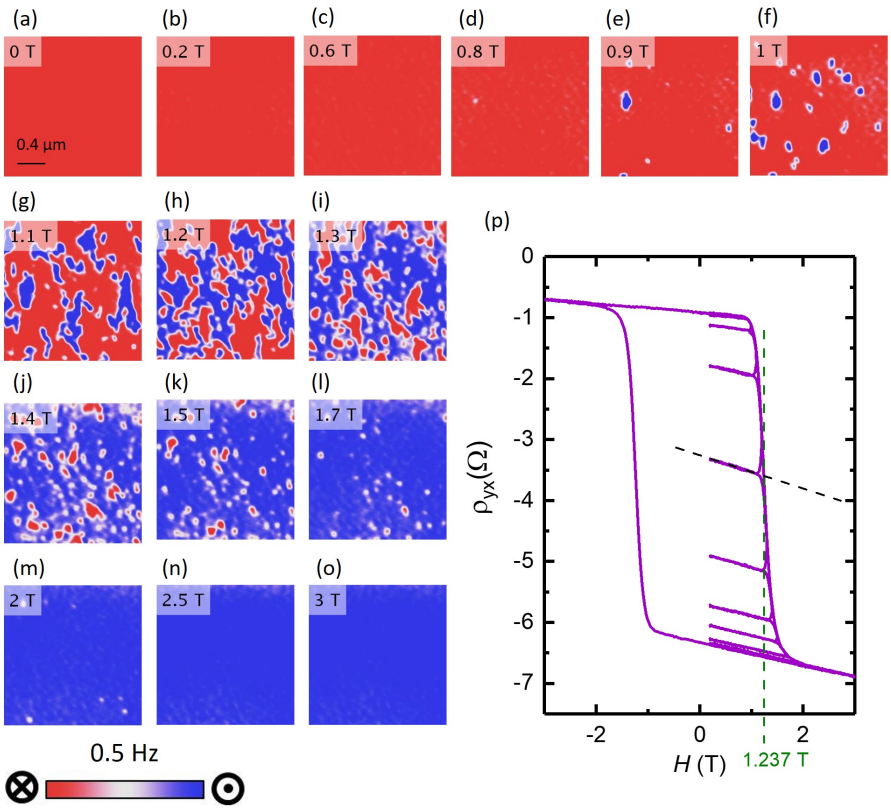

Figure 2.7: (a)-(o)MFM images of 7 u.c. SRO film at 30 K. Film was saturated at −3 T. The magnetic field was then ramped down to 0 T and swept to 3 T. (p) Raw Hall loop *in-situ* measured at 30 K. Black dashed line intercepts with the Hall loop (purple curve), giving the calibrated magnetic field.

exhibits bad metal behavior at high temperature. In addition, the thin films of $SrRuO_3$ have drawn attention for potential applications as a conducting layer in epitaxial multilayered structures of complex oxides. Due to the broad interest, over 1000 papers regarding to the physics, materials sciences and applications of $SrRuO_3$ have been published over the last two decades. And the interest keeps growing. In this section, the MFM and *in-situ* transport studies of 7 unit cell (u.c.) SRO thin films will be discussed. The M/M_S-H loops estimated by the field-dependent MFM images are quantitatively consistent with the anomalous Hall loops, indicating our MFM measurement is representative of the bulk properties.

The 7 u.c. SRO was epitaxially grown on $SrTiO_3$ substrate (001). Figure 2.7 shows the MFM images and *in-situ* transport data measured at 30 K. To minimized the relaxation

effect (domain wall creeping) near H_C and to minimize the stray field effect of the MFM tips, all MFM images were taken at a low magnetic field of approximately 0.2 T after the magnetic field was ramped to the desired field. However, small relaxations still exist during ramping the fields. In order to precisely achieve the $M-H$ loops and make a fair comparison with the $\rho_{yx}-H$ loops, the values of the magnetic field should be carefully calibrated. The dashed lines in Figure 2.7(g) indicate the process of calibrating field 1.2 T. The field was ramped down from 1.2 T to 0.2 T and stays at 0.2 T for 5 min for MFM imaging. The field dependence of ρ_{yx} shows a linear behavior at low field, indicating a robust ferromagnetic state without domain creeping. As the field ramped up from 0.2 T to 1.3 T, the $\rho_{yx}-H$ at low fields shows little hysteresis, further confirming the robustness of the ferromagnetic state around 0.2 T. The straight line extrapolated to high fields intersects with the $\rho_{yx}-H$ loop measured independently in the next round. The intersects gives the calibrated magnetic field 1.237 T, corresponding to 1.2 T. The calibrations of all the fields are listed in table 2.1.

nominal H (T)	0.9	10	1.1	1.2	1.3	1.4	1.5	1.7
calibrated H (T)	0.922	1.023	1.134	1.237	1.343	1.440	1.542	1.730

Table 2.1: Calibrated magnetic fields at 30 K

The field-dependent MFM images show a typical ferromagnetic domain behavior during the magnetization reversal process, via the domain nucleation and domain wall propagation. In order to obtain the M/M_S, up and down domain distribution should be properly estimated from MFM images. In the previous section, we discussed using a histogram analysis to estimate the up and down domain distributions. Here, an alternative method will be discussed by using the roughness (standard deviation) of MFM images.

Consider an Ising model with only up and down domains. Assign 1 for the up domain and 0 for the down domain. Assume the area distribution of up domain is A, then that of down domain is $(1-A)$. The standard deviation of this multi-domain state can be written as:

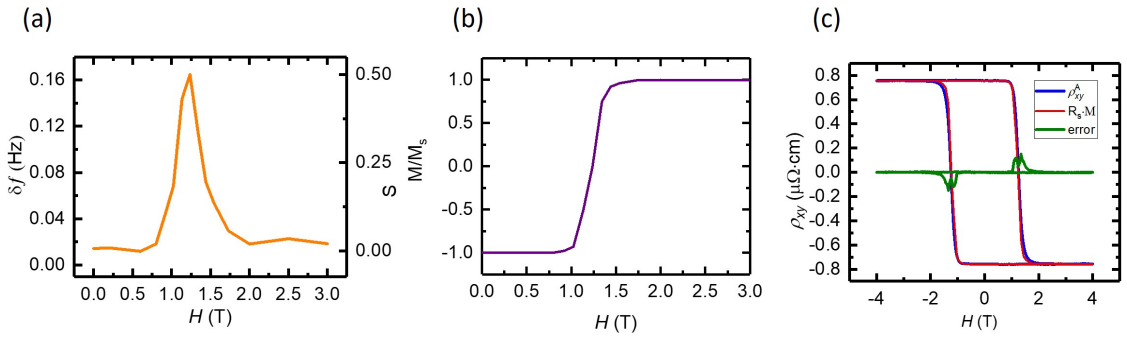

Figure 2.8: (a) Roughness of MFM images measured at various magnetic fields. (b) M/M_S estimated at various magnetic fields. (c) The anomalous Hall loop measured by transport (blue) and estimated by using MFM images (red). The difference is indicated by green curve.

$$S = \sqrt{\frac{\sum(x_i - \bar{x})^2}{N}} = \sqrt{A(1-A)} \tag{2.6}$$

S reaches maximum 0.5, when $A = 0.5$. This means the fifty-fifty domain state at H_C has the largest roughness. The up domain distribution A can be expressed in terms of S:

$$A = \frac{1 \pm \sqrt{1 - 4S^2}}{2} \tag{2.7}$$

where '+' for $H > H_C$ and '−' for $H < H_C$. The normalized magnetization M/M_S can be expressed as:

$$M/M_S = 2A - 1 = \pm\sqrt{1 - 4S^2} \tag{2.8}$$

where S takes values in [0, 0.5]. Fig. 2.8(a) plots the roughness of MFM images (δf) as a function of magnetic field, δf shows a maximum 0.165 Hz at H_C around 1.24 T. Linearly rescaling the MFM roughness to S values in [0, 0.5], The Eq. 2.8 can be used to estimated M/M_S, as plotted in Fig. 2.8(b). For a conventional ferromagnetic metal, the total Hall resistance consists of ordinary Hall effect ($\rho_{xy}^O = \rho_0 H$), which is proportional to external magnetic field H, and the anomalous Hall effect ($\rho_{xy}^A = \rho_S M$), which is proportional to magnetization M:

$$\rho_{yx} = \rho_0 H + \rho_S M \tag{2.9}$$

The anomalous Hall loop can be obtained from Hall data by subtracting out the ordinary Hall contribution, as the blue curve shown in Fig. 2.8(c). As a comparison, the $\rho_S M$ estimated from $M-H$ loop is shown as the red curve in Fig. 2.8(c), which is quantitatively consistent with the blue curve. The difference ($\sim$0.1 $\mu\Omega$·cm), shown in the green curve, is much smaller than the anomalous Hall signal ($\sim$0.8 $\mu\Omega$·cm). The great consistency between M/M_S-H loop from MFM and ρ_{xy}^A-H from transport indicates our MFM measurement is a reliable method to estimate M/M_S-H loop in a uniform ferromagnet, with relatively small domains ($\sim$ 100 nm).

Chapter 3

Visualization of ferromagnetic domains in magnetic topological insulators

Ever since the first experimental observations of quantum anomalous Hall effect (QAHE) in the magnetic topological insulators(TI), the magnetic TI becomes one of the most popular materials in condensed matter physics[3, 36, 37]. The direct visualization of the ferromagnetic domains is crucial to verify the long-range ferromagnetic ordering, which is a necessary condition to realize QAHE. These diluted magnetic semiconductor (DMS) thin films, however, have very tiny magnetic moments, which requires delicate magnetometry to probe. On the other hand, the existence of chiral edge states on the magnetic domain boundaries makes it more urgent to characterize the ferromagnetic domain structures in the QAHE systems. In this chapter, we will discuss the visualization of ferromagnetic domain structures of various magnetic TI systems, by using cryogenic magnetic force microscopy (MFM).

3.1 Ferromagnetic domains in magnetic TIs

Initial MFM studies of magnetic TIs were carried out on both single-crystal and thin-films of magnetic TI, such as Cr doped $(Bi,Sb)_2Te_3$(BST), and V-doped Sb_2Te_3. Although these specimens are either too thick or too conductive to exhibit quantum anomalous Hall effect. These pioneer works pave the way for the magnetic domain imaging of DMSs and magnetic TIs, and finally the QAHE systems.

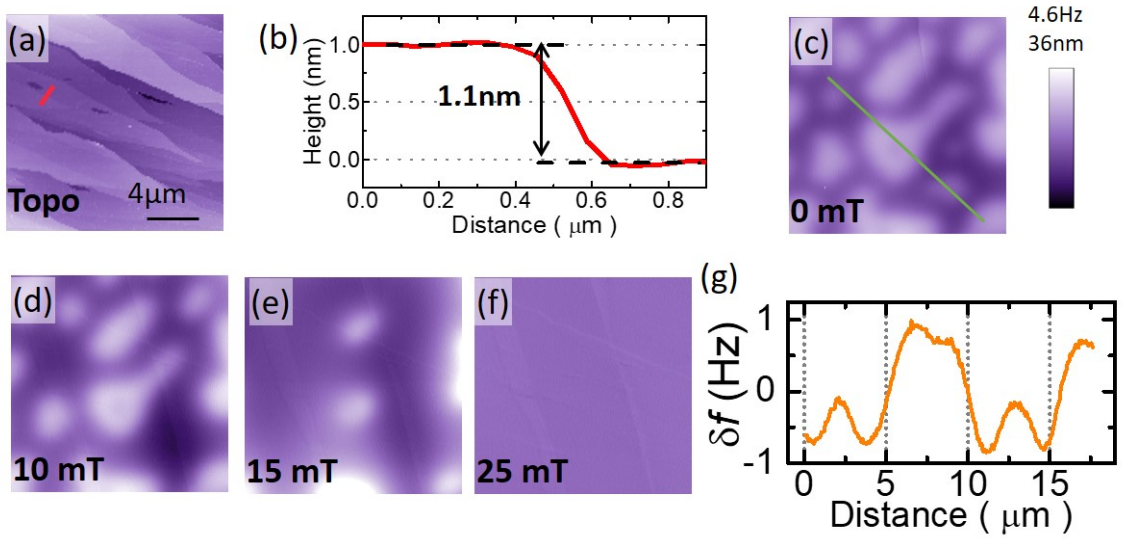

Figure 3.1: Topographic image (5.4 K) of a $(Bi_{0.1}Sb_{0.9})_{1.85}Cr_{0.15}Te_3$ single crystal. (b) A line profile of the red line in (a). The step height (1.1 nm) equals to the height of 1 QL. (c)-(f)MFM images with increasing magnetic fields taken at same location as topographic (a) after zero-field cooling. Magnetic field value of each image is shown at the bottom left corner. (g) A line profile of the orange line in (c). The color scale for topographic (MFM) image is 36 nm (4.6Hz).

3.1.1 Visualizing ferromagnetic domains in Cr-doped BST samples

In 2013, the QAHE was first demonstrated in Cr-doped BST films. After the pioneer works, extensive efforts had been on macroscopic characterization of magnetic TIs. However, little had been done on magnetic imaging of ferromagnetic domains in these materials. The characteristic size and shape of these domains remain largely unknown, which hinders the progress of investigation and applications of chiral edge states at domain walls. In this section, we will briefly discuss the MFM studies on both single crystal and thin film specimens of Cr-doped BST. Details of this work are available in reference:[120].

Single crystals of $(Bi_{0.1}Sb_{0.9})_{1.85}Cr_{0.15}Te_3$ were grown by modified Bridgeman method. Clean sample surface was prepared by Scotch-tape cleavage in air. Thin films of nominally the same composition were synthesized by MBE, then capped by amorphous Se($\sim$ 100 nm). The nominal thickness of films measured by MFM is 17 quintuple layers (QL).

Figure 3.1 shows a topographic image and MFM images at various magnetic fields on the

cleaved surface of a single crystal at 5.4 K after zero field cooling (ZFC). Atomic steps with integer QL are clearly observed in topographic image, indicating a clean cleaved surface. An example of one QL step edge is shown in the line profile in Fig. 3.1(b). Fig. 3.1(c) shows bubble-like ferromagnetic domains with the average size 5 μm. A representative line profile is shown in Fig. 3.1(g). The domain wall width is estimated to be $\sim$2 μm, which is significantly larger than the spatial resolution of our MFM tip ($\sim$100 nm). Note that a simple Block wall model predicts very small domain wall width ($\sim$7 nm)[120]. The large domain wall width observed in MFM indicates either a unconventional domain wall structure or a curved domain wall beneath the surface. As perpendicular magnetic fields are applied to the sample, the bubble domains with the moment parallel to the applied fields gradually shrunk and eventually disappeared [see Fig. 3.1(C)-3.1(f)]. At 25 mT, no domain contrast was observed within scan area, indicating the sample was in single domain state, i.e., all magnetic moments were aligned with external field. The single crystal remained in single domain state after the magnetic field is removed, suggesting a strong uniaxial anisotropy. Reversing the field to negative coercive field, $H_C \approx -15$ mT induced anti-parallel domains with even larger domain size. The domain contrast disappeared when warming sample above Curie temperature ($T_C \approx$15 K). A mean field-like temperature dependence of domain contrast was observed on cooling the sample below T_C[120]. The values of T_C and H_C agree well with bulk magnetization measurements[120] and are comparable with those in previous studies of single crystals with similar composition[121], indicating our MFM observation reflects typical domain behaviors in single crystals of magnetic TIs.

The large domain size and domain wall width of single crystal samples make it difficult for scanning probe microscopy studies of the chiral edge states. For example, the large domain size (a few μm) exceeds the typical scan range ($\leq$1 μm) of scanning tunneling microscopes (STMs). Consistently, previous spin-polarized STM studies did not observe any domain structure in single crystals of Cr doped Sb_2Te_3. On the other hand, smaller domains may exist in thin film specimens because of size confinement effect., *i.e.*, the Kittel's

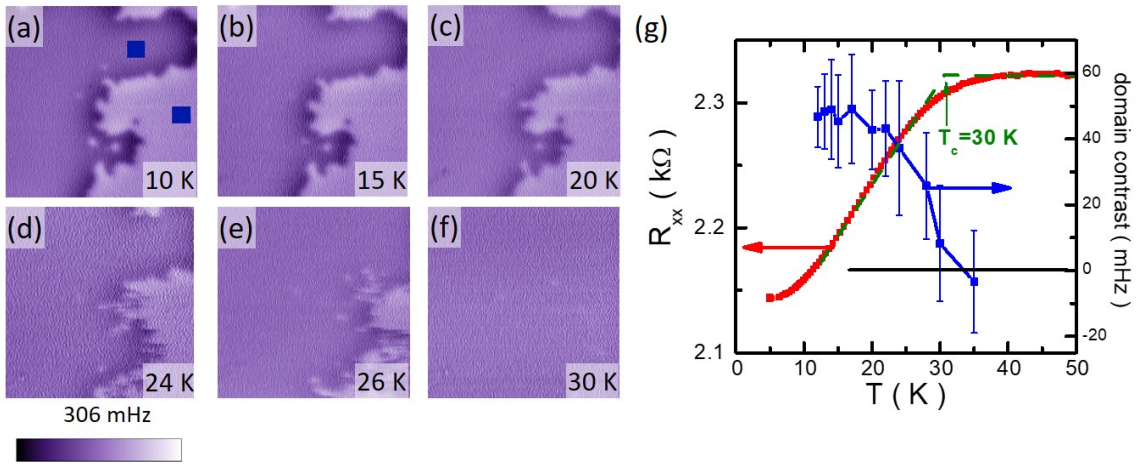

Figure 3.2: (a)-(f) MFM images of a large domain boundary measured on warming in zero field. The pinning of domain wall becomes weaker as T approaches T_C (∼30 K). There is a visible domain wall motion in MFM images taken at 24 K (d) and 26 K (e), indicating depinning of domain wall induced by MFM tip stray field. No domain contrast was observed above T_C. (g)T-dependence of 2-probe resistance (red filled circles) measured in zero field on cooling from room temperature to 5 K, and T-dependence of domain contrast (blue filled squares) defined as the difference between the mean values of the two blue boxes in panel (a).

law. This is confirmed by magnetic imaging of ferromagnetic domains in MBE thin films with nominally the same composition.

MFM images have been taken at 6 K on 17QL Cr-doped BST film. The Cr-doped BST films have small coercivity (∼ 0.05 T at 6 T), which is comparable with the stray field of the magnetic tip. Thus, during the non-contact mode scanning, the tip has strong interaction with the sample, which modifies the magnetic domain patterns. Pinned bubbles domains with a size ∼500 nm have been observed during magnetic field sweeping.[120] In addition to random bubble domains, a long pinned domain boundary separating large magnetic domains was observed occasionally at the coercive field during the magnetic reversal, as shown in Fig. 3.2(a). Temperature dependence of these large domains is shown in Fig. 3.2(a)-(f). As the temperature increases, domain contrast becomes smaller and smaller. At the same time, the pinning strength becomes weaker. At $T \geq 24$ K, the pinning strength becomes so weak that the domain boundary can be moved by the stray field of MFM tip. At 30 K, domain contrast disappeared, indicating a transition from ferromagnetic

state to paramagnetic state. The temperature dependence of domain contrast exhibits a mean-field-like behavior with a transition at $T_C \approx 30\,\mathrm{K}$[blue squares in Fig. 3.2(g)]. The temperature dependence of *in-situ* 2-probe resistance $R(T)$ also shows a shoulder at $\sim 30\,\mathrm{K}$[red filled circle in Fig. 3.2(g)], in good agreement with the MFM results. This transport anomaly is a characteristic of magnetic ordering commonly observed in magnetic metals and semiconductors. The reduction of resistivity is due to suppression of spin-flip scattering by magnetic ordering.

3.1.2 Visualizing ferromagnetic domains in V-doped Sb_2Te_3 films

V-doped BST film is the second magnetic TI system that exhibits QAHE[38]. Comparing to Cr-doped BST films, V-doped ones have a more robust QAH state, with higher precision. Moreover, V-doped BST film is a hard ferromagnet with a larger coercive field ($H_C \sim 1.0\,\mathrm{T}$) and higher Curie temperature (T_C). These features make the V-doped BST thin films more preferable to be utilized for magnetic domain imaging. In addition to the robust QAH effect, a remarkable spontaneous self-magnetization effect has been reported in V-doped BST thin films[38]. The non-zero net magnetization develops in the virgin state in zero magnetic fields, which is not commonly seen in conventional ferromagnetic materials. In order to solve these mysteries, we utilized MFM to investigate the domain behavior of V-doped Sb_2Te_3 thin films[122]. Note that V-doped Sb_2Te_3 should have stronger ferromagnetism, comparing to V-doped BST, because it has more bulk charge carriers (valence band) to mediate RKKY interaction.

Epitaxial thin film $Sb_{1.89}V_{0.11}Te_3$ capped with 10 nm Te was grown on heat treated $SrTiO_3$ (111) substrate by co-evaporation in a molecular beam epitaxy system. The nominal thickness of the film is 10 QL. MFM images were taken in a constant mode with the scanning plane $\sim 40\,\mathrm{nm}$ above the sample surface.

Figure 3.3 shows topographic and MFM images of the $Sb_{1.89}V_{0.11}Te_3$ thin film at 5 K after ZFC and field cooling (FC). The topographic image shows a flat surface with roughness

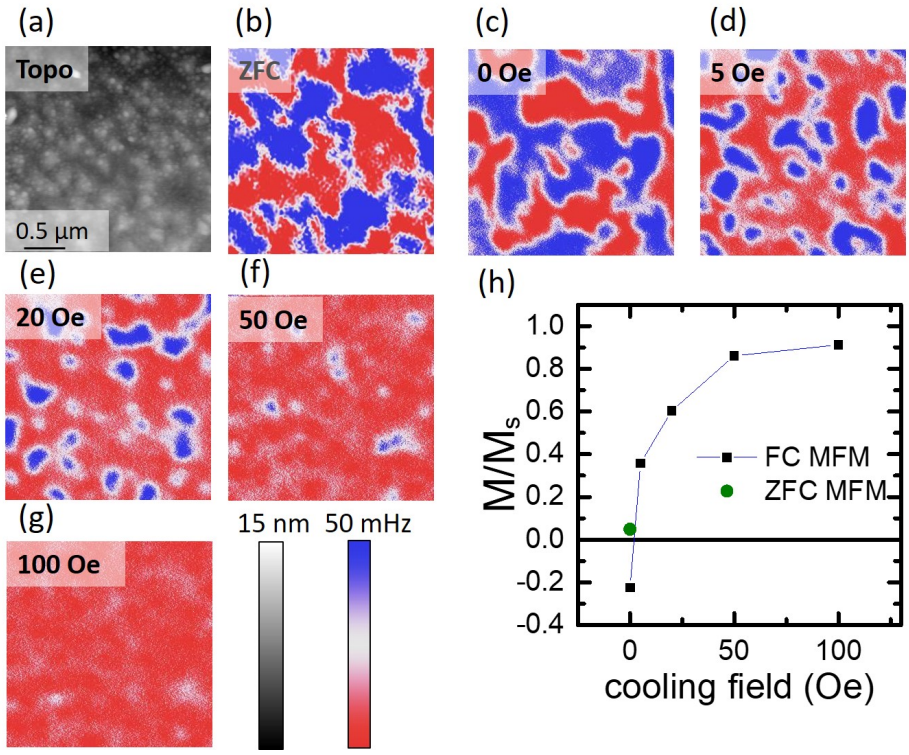

Figure 3.3: Topographic (a) and MFM image (b) measured at 5 K after ZFC. The equal population of up (red) and down (blue) domains indicates a zero-magnetization virgin domain state. (c)-(g) MFM images (5 K) of FC domain states with cooling fields ranging from 0 Oe to 100 Oe. The cooling field values are labeled at the upper-left corner of each MFM image. The color scale is 15 nm (50 mHz) for topographic (MFM) image(s), and 20 mHz for the ZFC MFM image (b). Note that the ZFC image (b) was slightly filtered to enhance the signal to noise ratio. (h) Cooling field dependence of the net magnetization of various domain states is inferred from MFM images using a histogram analysis of MFM images. The trapped flux in the superconducting magnet is estimated to be ~ 3 Oe.

$\sim$ 1.9 nm. The topographic features are likely surface contamination after the film was exposed to air. The virgin state after ZFC, as shown in Fig. 3.3(b), exhibits a multi-domain state which is unlike the reported self-magnetization behavior. Fig. 3.3(c)$-$(g) show MFM images of the same region at 5 K after FC. The sample was thermally cycled to 60 K, then cooled down to 5 K with the superconducting magnet set to the field values labeled on the upper left corner of each panel in Fig. 3.3. As shown in Fig. 3.3(c), the nominal 0 Oe FC data shows that the sample is slightly negatively polarized, indicating the existence of negative trapped flux in the superconducting magnet. This is consistent with the history of the superconducting magnet usage, since the field was ramped down from a positive value

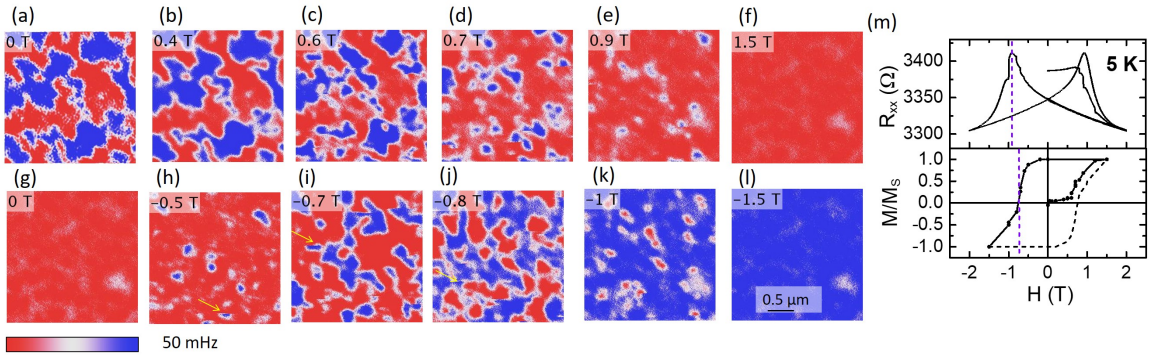

Figure 3.4: (a)-(l) 5 K field-dependent MFM images of the virgin domain state after ZFC show a typical domain behavior with a strong pinning effect. The applied magnetic fields are labeled at the top-left corner of each MFM image. (m)The field dependence of 2-probe resistance R_{xx} was measured with the field sweeping within ±2 T.The M-H hysteresis loop deduced from MFM images is qualitatively consistent with the R-H butterfly loop. The coercive field is 0.92 T from R-H and 0.76 T from M-H.

to zero, i.e. negative trapped flux due to a slight overshot of the power supply. Applying a small field (*e.g.* 5 Oe) during cooling can significantly polarize the film [see Fig. 3.3 (d)] and the film saturates at 100 Oe [see Fig. 3.3 (g)], indicating divergent correlation length at T_C due to strong ferromagnetic exchange interactions. The systematic variation of domain population is a strong evidence of long-range ferromagnetic order in V-doped Sb_2Te_3.

In order to quantitatively characterize the domain states after different field cooling, the population of positive and negative domains was estimated by conducting a histogram analysis of these MFM images. The histogram curves exhibit two peaks which correspond to up and down domains[122]. We used the peak height to estimate the population of up and down domains. The normalized magnetization of the thin film M/M_S (M_S: saturation magnetization) therefore can be estimated from: $(N_\uparrow - N_\downarrow)/(N_\uparrow + N_\downarrow)$, where $N_\uparrow$ and $N_\downarrow$ are populations of up and down domains, respectively. The normalized magnetization as a function of cooling field is plotted in Fig. 1.1 (h). The trapped flux of our superconducting magnet inferred from linear extrapolation is roughly 3 Oe. Therefore, the previously observed self-magnetization effect is likely an extrinsic effect due to non-zero trapped flux in the superconducting magnet[38].

The ferromagnetic domain behavior was also investigated by performing field-dependent

MFM imaging of the domain state after ZFC, as shown in Figure 3.4. The ZFC domain state is essentially unchanged up to 0.4 T, indicating a strong domain wall pinning effect of a hard ferromagnet [38]. The domain contrast enhancement between 0 and 0.4 T is due to the enhancement of the MFM tip moment by the external magnetic field. Higher magnetic fields induce more red regions (up domains), where spins are parallel with external fields. The film reaches saturation at 1.5 T, as no blue region (down domain) remains. There are some weak MFM contrasts in the saturation state, which anti-correlate with topographic features shown in Fig. 3.3(a). So they are non-magnetic features, possibly originating from residual electrostatic interactions due to the variation of contact potential caused by surface contamination. The film remained in the saturation state after the field was ramped down to zero, suggesting a strong uniaxial anisotropy that prevents domain nucleation at zero field. This is in sharp contrast with the superparamagnetic behavior observed in prior studies of Cr-doped BST, where substantial relaxation was observed at zero and low fields [4]. For our sample, significant relaxation was observed near the coercive field.

The down domains start to nucleate at -0.5 T. Further decrease in H induced more down domains (blue region). A fifty-fifty domain state was recovered at approximately -0.7 to -0.8 T which is defined as the coercive field (H_C). Significant domain relaxation was observed near H_C, as shown by sharp domain switching along the slow scan axis in MFM images near coercive fields, *e.g.* as indicated by arrows in Fig. 3.4,(h),(i),(j). At -1.5 T, the sample was fully polarized (Fig. 3.4(l)). The magnetization reversal process observed in the 10 QL $Sb_{1.89}V_{0.11}Te_3$ thin film is more consistent with typical ferromagnetic domain reversal behavior, including domain nucleation and domain wall propagation[123]. The $M(H)$ hysteresis loop deduced from MFM images was plotted in Fig. 3.4(m). Note that we only measure the virgin curve and half of the hysteresis loop. The other half (dashed line) was replicated from measured results via a symmetric operation, assuming the hysteresis loop is symmetric about zero field. The coercive field (H_C) deduced from MFM images is ~ 0.76 T.

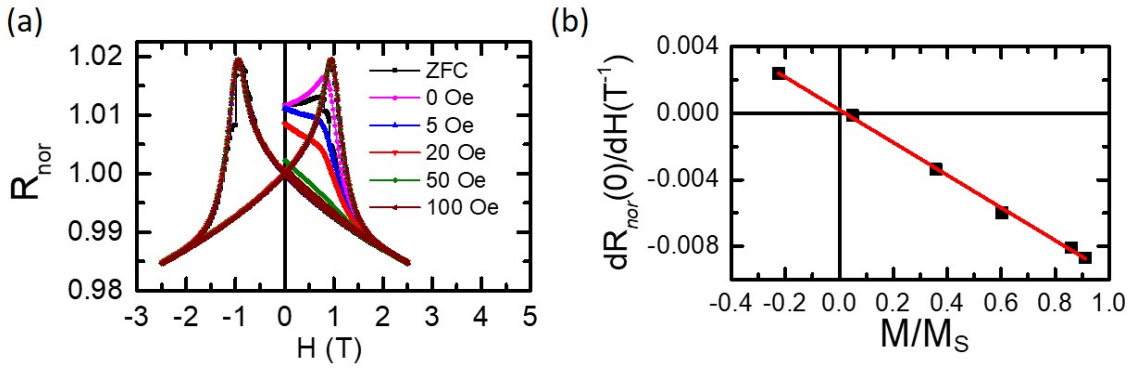

Figure 3.5: (a) Field dependence of normalized resistance $R_{nor} = R_{xx}(H)/R_{xx}(0)$. Magnetoresistance ($R_{xx}$) was measured with the magnetic field sweeping within $\pm 2.5\,\mathrm{T}$ after FC (0 to 100 Oe). (b) Graph of the initial slope of normalized resistance vs normalized net magnetization. The linear relationship between them is evidenced from the linear fit (red line).

The *in-situ* two-probe resistance (R) measurement was performed simultaneously with MFM measurement. The $R(H)$ butterfly loop was qualitatively consistent with the $M(H)$ loop [see Fig. 3.4(m)] though the H_C from transport ($\sim 0.92\,\mathrm{T}$) is slightly higher. The difference likely originates from the stray field from the MFM tip, which locally adds to the external magnetic field[120]. So the scanned region (probed by MFM) experiences a higher magnetic field than the rest of the sample (probed by R). Note that it takes some time ($\sim 5-10$ minutes) to capture each MFM image. The steps in the $R(H)$ loop indicate a substantial time relaxation effect around the coercive field. Although similar relaxation behavior was also observed in Cr-doped magnetic TIs[4, 124, 125], the relaxation in V-doped films is more consistent with typical ferromagnetic domain behavior, *i.e.* domain nucleation and domain wall propagation.

Further evidence of ferromagnetic domain behavior comes from the robust domain pattern against thermal fluctuation at the elevated temperature up to 20 K. The domain contrast quickly diminished upon warming the film to 35 K. This is consistent with $T_C \sim 32\,\mathrm{K}$ deduced from $R(T)$ data[120]. The agreement between bulk transport measurement and local MFM measurement suggests that our MFM results reflect a representative domain behavior of the $Sb_{1.89}V_{0.11}Te_3$ thin film.

Figure 3.5 shows *in-situ* magnetoresistance (MR) measurement of different FC domain states. The initial MR curves of different domain states show a systematic behavior. First, the single domain state is more conducting than the multi-domain state, as the zero-field resistance $R(0)$ of 100 Oe FC is significantly less than ZFC, while $R(0)$ of 0 Oe and 5 Oe FC are very close to ZFC. The difference may be related to the density of domain walls in different domain states. The more polarized film has smaller domain wall density. It is known that the domain walls enhance electron scattering in ferromagnetic metals[126, 127], thus, the multi-domain state is usually more resistive. Second, the slope of the MR curve at zero field is proportional to the net magnetization, as shown in Fig. 3.5(b). This can be understood in terms of averaged MR of the multi-domain state. For domains with magnetization along the direction of the external magnetic field, the intensity of thermal excitation, i.e. spin wave excitation (magnon), will be suppressed by the external field. Therefore magnon-electron scattering will be suppressed, and thus resistivity will be lowered. Conversely, the magnon-electron scattering will be enhanced for domains with magnetization opposite to the direction of the external magnetic field because of enhancement of spin wave intensity. Assuming a linear response at the zero-field limit, the change in resistance due to the external magnetic field for positive or negative domains is $\Delta R_{\pm} = \mp k \cdot H$ $(k > 0)$. Assuming the fraction of up (down) domains is $N_{\uparrow}$ $(N_{\downarrow})$ and a simple linear resistance model, the net resistance change would be, $\Delta R = N_{\uparrow} \cdot \Delta R_{\uparrow} + N_{\downarrow} \cdot \Delta R_{\downarrow} = k \cdot (N_{\downarrow} - N_{\uparrow}) \cdot H$, *i.e.* $\frac{dR}{dH}|_{H=0} = k(N_{\downarrow} - N_{\uparrow}) \propto -M/M_S$, in good agreement with results in Fig 1.3(b). Note that the transport properties of V-doped Sb_2Te_3 are dominated by bulk (valence band) carriers [38]. Such MR behavior due to bulk carriers would diminish in insulating V doped BST at low temperature where QAH chiral edge states dominate the transport.

3.2 Visualization of ferromagnetism in a quantum anomalous Hall system

Although convincing evidence of ferromagnetism has been observed in both Cr-doped BST and V-doped Sb_2Te_3, these specimens either too thick or too conductive to exhibit QAHE. In this section, we will discuss the visualization of ferromagnetic domains in a quantum anomalous Hall system[128].

The main problem that hinders the further exploration of QAHE in magnetic TIs is the ultra-low temperature required to achieve the full quantization. For both Cr-, or V-doped BST films, full quantization of Hall resistance was observed below 50 mK. As illustrated in 1.1.3, the magnetic inhomogeneity and VBM above the Dirac point may be the two factors that limit the QAH temperature. Here, we will focus on solving the magnetic inhomogeneity issue in quantum anomalous Hall systems.

Recently, enhanced QAH temperature was observed in Cr,V co-doped BST thin films[14]. At optimal Cr/V ratio, full quantization was achieved at 300 mK, an order of magnitude higher than the end members with single dopants[14]. The Hall hysteresis loop is more square-like, suggesting a sharper magnetization reversal, *i.e.*, less magnetic inhomogeneity. Furthermore, the temperature dependence of anomalous Hall resistance is more mean-field-like. These observations indicate improved ferromagnetism in Cr/V co-doped TI thin films. However, direct microscopic evidence of long-range ferromagnetic ordering is still lacking. Note, that intrinsic anomalous Hall effect is determined by the Berry phase of occupied bands, which is independent of magnetization magnitude[129]. In this section, we report a systematic study of Cr/V co-doped BST thin films using magnetic force microscopy (MFM).

Epitaxial thin film Cr/V co-doped BST films capped with 2 nm Al was grown on a heat treated $SrTiO_3(111)$ substrate by co-evaporation in a molecular beam epitaxy (MBE) system. The nominal thickness of the film is 5 quintuple layers (QL). The film was scratched by hand into a Hall bar shape connected with a large square-like area for MFM measurements.

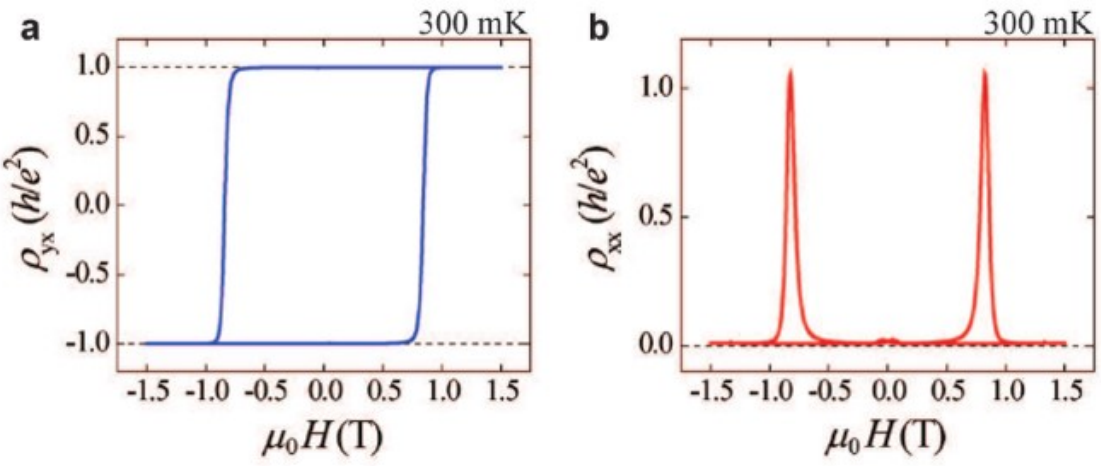

Figure 3.6: **Transport properties of 5 QL $(Cr_yV_{1-y})_{0.19}(Bi_xSb_{1-x})_{1.81}Te_3$ ($y = 0.16$) film** | 300 mK Hall traces (ρ_{yx} vs. $\mu_0 H$) (a) and MR curves (ρ_{xx} vs. $\mu_0 H$) (b) of the film measured at $V_g = V_g^0$. Adapted from Ref.[14].

A layer of $\sim$ 15 nm Au film was deposited on the square area to eliminated electrostatic interaction between the sample and magnetic tip. Fig. 3.7(a) shows the schematic picture of the Hall bar device of the magnetic TI thin films fabricated for MFM and *in-situ* transport measurements. Three $(Cr_yV_{1-y})_{0.19}(Bi_xSb_{1-x})_{1.81}Te_3$ films ($y = 0, 0.16, 1$, respectively and $x \sim 0.4$) are fabricated into the Hall bar devices. All MFM data presented here were taken at 5 K. As shown in Fig. 3.7(b), the $y = 0.16$ film is the optimized sample (Curie temperature $T_C \approx 28$ K) with the best ferromagnetic behavior (sharpest reversal) and the highest Hall conductance (1.5 K). In addition, the temperature dependence of the Hall resistance is more mean-field-like, indicating robust ferromagnetism [14]. The longitudinal resistance starts to decrease right below T_C, indicating that the sample enters the QAH regime as soon as the long-range ferromagnetic order forms, as shown in Fig. 3.8(a). The end member ($y = 0$ or 1), however, enters the QAH regime at a much lower temperature. Gate voltage (V_g) was applied to the back of the STO substrate to tune the Fermi level. At 1.5 K, the Hall resistance reaches 0.95 h/e^2 at V_g^0, as shown in Fig. 3.8(b). Such a quantization level was only achieved below 50 mK in single Cr- or V-doped thin films[3, 36–38].

Figure 3.9a,h shows the MFM images and *in-situ* transport data (ρ_{xx} and ρ_{yx}) of the

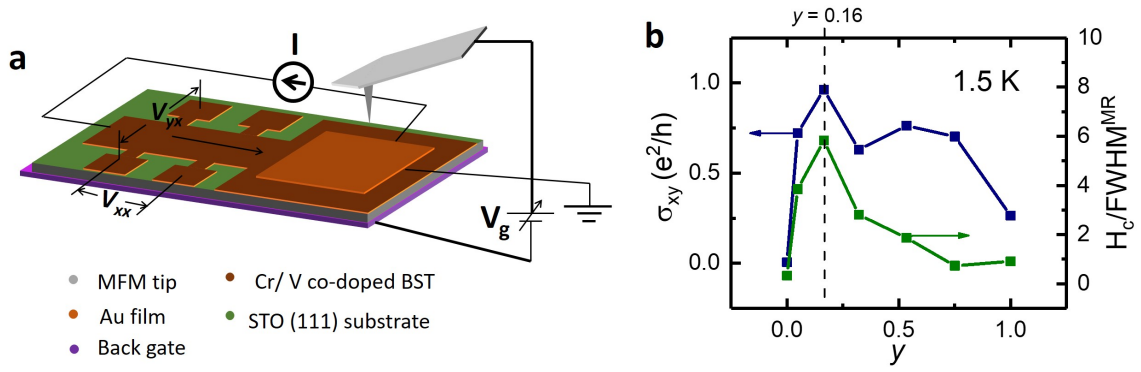

Figure 3.7: | **Schematic of the *in-situ* transport setup and the Cr concentration (y) dependence of σ_{xy} and H_C/FWHM^{MR}.** (a) A schematic of the Hall bar device for MFM and *in-situ* transport measurements. The 5 QL Cr/V co-doped BST thin film was grown on STO(111) substrate using MBE, followed by deposition of a layer of 15 nm Au film. Both Au film and magnetic tip were grounded to eliminate any electrostatic interaction between them. A back-gate voltage V_g was applied to the bottom electrode to tune the charge carrier density. The Hall resistance ρ_{yx} and longitudinal resistance ρ_{xx} were obtained by measuring V_{yx} and V_{xx}. (b) Cr concentration (y) dependence of zero magnetic field Hall conductance σ_{xy} (blue) and the ratio of coercivity (H_C) to the full-width-half-maximum (FWHM) of magnetoresistance (MR) at 1.5 K.

optimally doped film ($y = 0.16$) at $V_g^0 \simeq 10$ V at various magnetic fields. The $\rho_{yx}(H)$ loop shows a saturation $\sim 0.5\,h/e^2$ with a coercive field $H_C \sim 0.26$ T. The magnetization reversal process from downward (red) to upward (blue) magnetized states is illustrated in the MFM images. The downward saturated state has very weak magnetic contrast with a small positive field (+0.05 T), indicating the single domain state persists at a small reversed field, showing a compelling evidence of robust ferromagnetism. The observed stable single domain state, with little relaxation, is in sharp contrast to the superparamagnetic behavior previously reported in Cr-doped BST films, where significant relaxation was already observed at small magnetic fields [4]. At 0.15 T, up domains start to nucleate, represented by light blue regions. As the field increases further, up domains expand and down domains shrink. At the coercive field H_C where $\rho_{yx} = 0$ and ρ_{xx} peaks at $\sim 0.8\,h/e^2$, equally populated up and down domains were observed, confirming the zero magnetization state ($M = 0$). For $H \geq 0.35$ T, no red regions are visible in MFM images, indicating the system is in a saturated (single domain) state. The MFM observation of ferromagnetic domain behavior

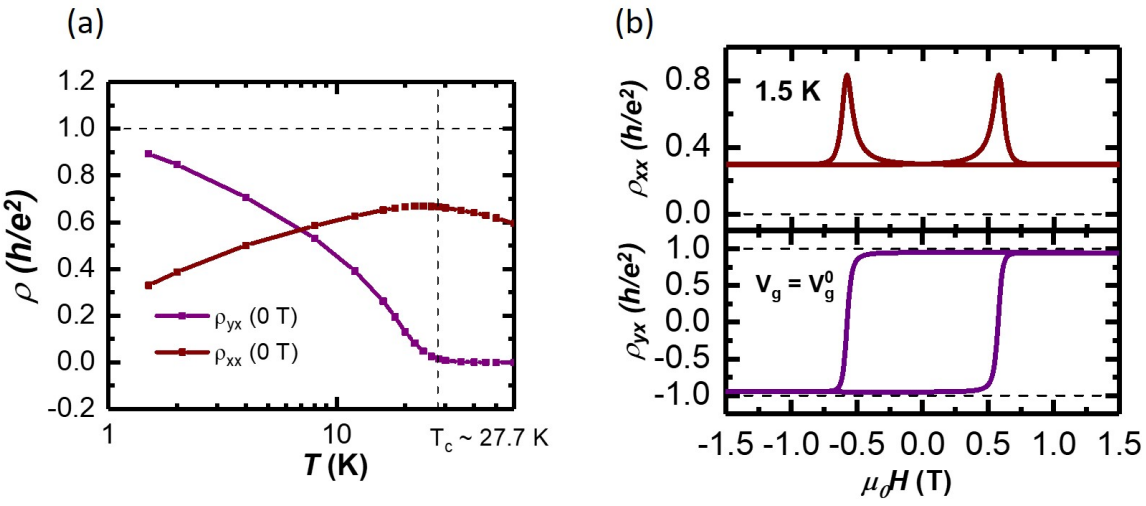

Figure 3.8: (a) Temperature dependence of Hall resistance (ρ_{yx}) and longitudinal resistance (ρ_{xx}) at zero magnetic field. (b) 1.5 K Hall traces (ρ_{yx} vs. $\mu_0 H$) and MR curves (ρ_{xx} vs. $\mu_0 H$) of the film measured at $V_g = V_g^0$.

is in excellent agreement with the *in-situ* transport data, suggesting local observation is representative of the global (bulk) properties. Note that the Hall data at 1.5 K and 5 K show similar square-like hysteresis loops, indicating no qualitative difference between these two temperatures. Furthermore, a larger coercive field (H_C) and sharper reversal observed at the lower temperature suggest better ferromagnetism. Therefore, the observed ferromagnetic behavior is expected to persist at the lower temperature where full quantization was observed on the same sample [14].

The ferromagnetic domain behavior can be further illustrated with the difference between MFM images of adjacent fields, as shown in Fig. 3.9(a). The locations where the changes in MFM signal are above the noise level ($\sim$ 2 mHz) are defined as the newly reversed regions. They are marked by different colors at each field value, which are shown in the right column of Fig. 3.9(a). The unchanged areas are marked with white color. In Figs. 3.9b-g, these differential images were stacked together to show the spatial correlations of magnetization reversal events in order to differentiate isolated domain nucleation from domain expansion. For example, as shown in Fig. 3.9(c), some of the newly reversed regions (yellow) at 0.2 T have no correlations with previously reversed regions (red). These

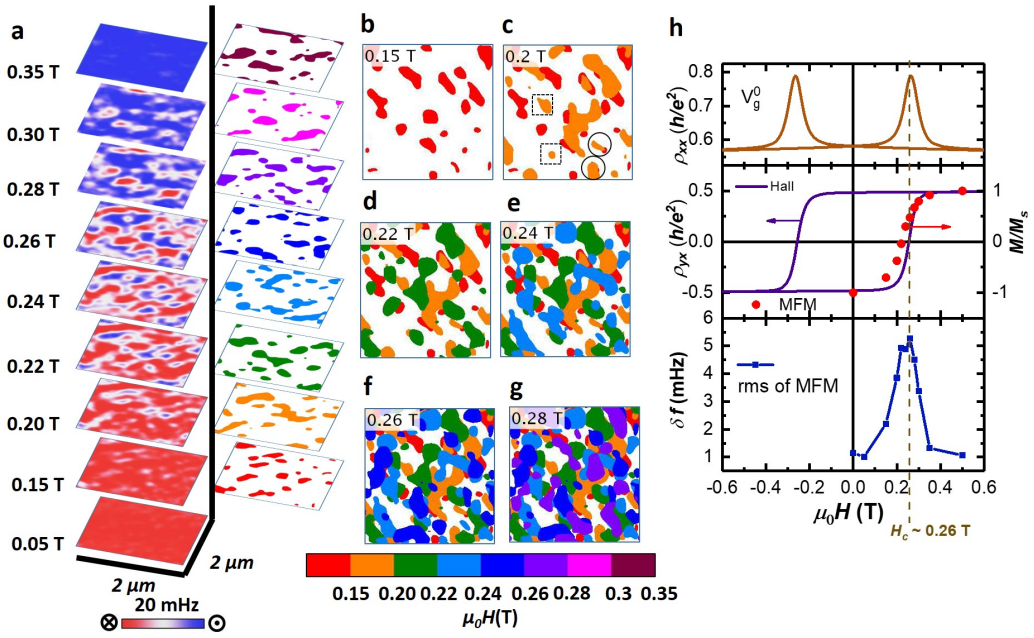

Figure 3.9: | **The magnetization reversal process at 5 K at neutral point V_g^0.** (a) Left column: stack of MFM images from 0.05 T to 0.35 T to illustrate domain evolution; Right column: differential images by taking the difference between adjacent MFM images. Different colors represent local magnetization reversed at different magnetic fields. (b)-(g) Images of the reversed areas at various fields by combining the differential images, which illustrate domain nucleation and possible domain wall propagation. Dashed squares label nucleation sites and solid circles label possible domain wall propagation. (h) Top: *in-situ* transport data (ρ_{xx}) at $V_g^0 \simeq 10$ V. Middle: H-dependence of normalized magnetization M/M_s, estimated from domain population, is consistent with the anomalous Hall loop (ρ_{yx}). Bottom: H-dependence of the domain contrast (δf_{rms}) which peaks at H_C. The MFM images show ferromagnetic domain behavior during the magnetization reversal from 0.15 T to 0.35 T, consistent with transport data.

regions, labeled by dashed squares, are isolated nucleation sites. The other yellow regions, labeled by solid circles, have some overlap with the red regions, likely due to tilted domain walls. This behavior is consistent with domain growth via either domain wall propagation or domain wall induced nucleation. The domain behavior is distinctively different from the superparamagnetic behavior of random switching events in the prior report [4].

In addition to direct visualization of ferromagnetic domain behavior, MFM data can also be used to extract the hysteresis loop of normalized magnetization (M/M_s), which is estimated from the populations of up and down domains [122]. As shown in Fig. 3.9(h), the $M/M_s(H)$ curve quantitatively agrees with the $\rho_{yx}(H)$ loop.The agreement between local

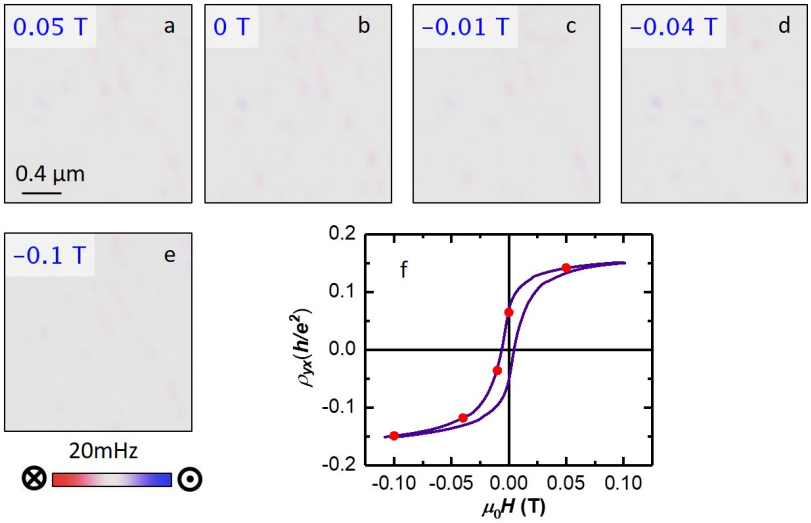

Figure 3.10: **5 K MFM and *in-situ* Hall data of Cr-doped BST film at various magnetic fields** | (a)-(e) MFM data show very weak magnetic signals during magnetization reversal process from 0.05 T to −0.1 T. (f) Hall trace at 5 K shows a hysteresis loop with $H_C \approx$ -5 mT. Red dots denote the Hall data, measured at the same field as the MFM data.

(domain population) and global (ρ_{yx}) measurements demonstrate that our MFM results are representative of the bulk magnetic properties. Consistently, the domain contrast, estimated by the root-mean-square (RMS) value of the MFM signal (δf_{rms}), peaks at H_C when up and down domains are equally populated. The observed domain behavior provides unambiguous evidence of long-range ferromagnetic order in the optimally Cr/V co-doped BST thin films. In contrast, MFM measurements on single doped BST films do not reveal clear ferromagnetic behavior, see Fig. 3.10 and 3.11. Therefore, our MFM data provides direct evidence that long-range ferromagnetic order is essential for the enhancement of the QAH temperature [14].

The long-range ferromagnetic order is one of the key ingredients of QAHE. Yu *et al.* proposes a Van Vleck mechanism in magnetically doped TIs, where the exchange interaction between local moments are mediated by band electrons with significant Van Vleck susceptibility [130, 131]. Therefore, the Van Vleck mechanism is independent of bulk carrier density. However, other studies indicate that an RKKY type exchange plays a significant role when bulk or surface carriers are present[132, 133]. To shed light on the exchange

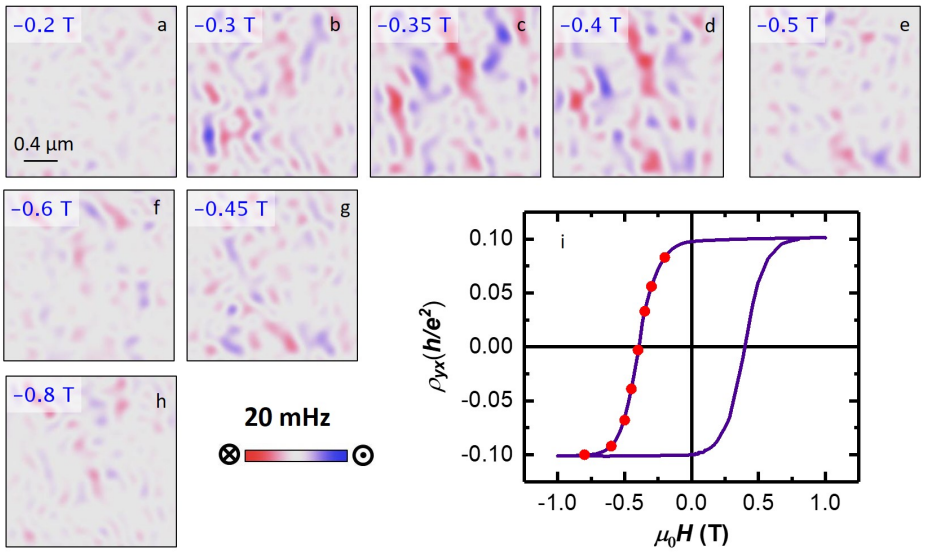

Figure 3.11: **5 K MFM and *in-situ* Hall data of V-doped BST film at various magnetic fields** | (a)-(h) MFM data show a inhomogenous ferromagnetic behavior during magnetization reversal process from −0.2 T to −0.8 T. (i) Hall trace at 5 K shows a hysteresis loop with $H_C \approx$ -0.4 T. Red dots denote the Hall data, measured at the same field as the MFM data.

mechanisms, we investigate the bulk carrier dependence of the ferromagnetism by applying a gate voltage (V_g). Similar to the neutral point V_g^0 case, both electron-doped (300 V) and hole-doped (−300 V) states show typical ferromagnetic domain behavior, confirming that long-range ferromagnetic order is robust against tuning the Fermi level near the neutral point[128], supporting the presence of a Van Vleck mechanism. Fig. 3.12(a)-(c) show the MFM images at H_C and the nucleation maps of the three gate voltages. Comparing the three multi-domain states, hole-doping results in larger domain size, fewer nucleation sites, and stronger domain contrast, while electron doping results in an opposite trend. Consistently, H_C is enhanced (suppressed) by hole (electron) doping, as shown in the $\rho_{yx}(H)$ loops in Fig. 3.12(d). On the other hand, both hole and electron doping away from the neutral point suppress the anomalous Hall effect. Note, that the domain contrast of the multi-domain state is proportional to the saturated magnetization [116]. The enhanced domain contrast at H_C indicates an increase in saturated magnetization with hole doping. Comparing to the local magnetic moment density, the gate-induced charge carrier density is negligible[128].

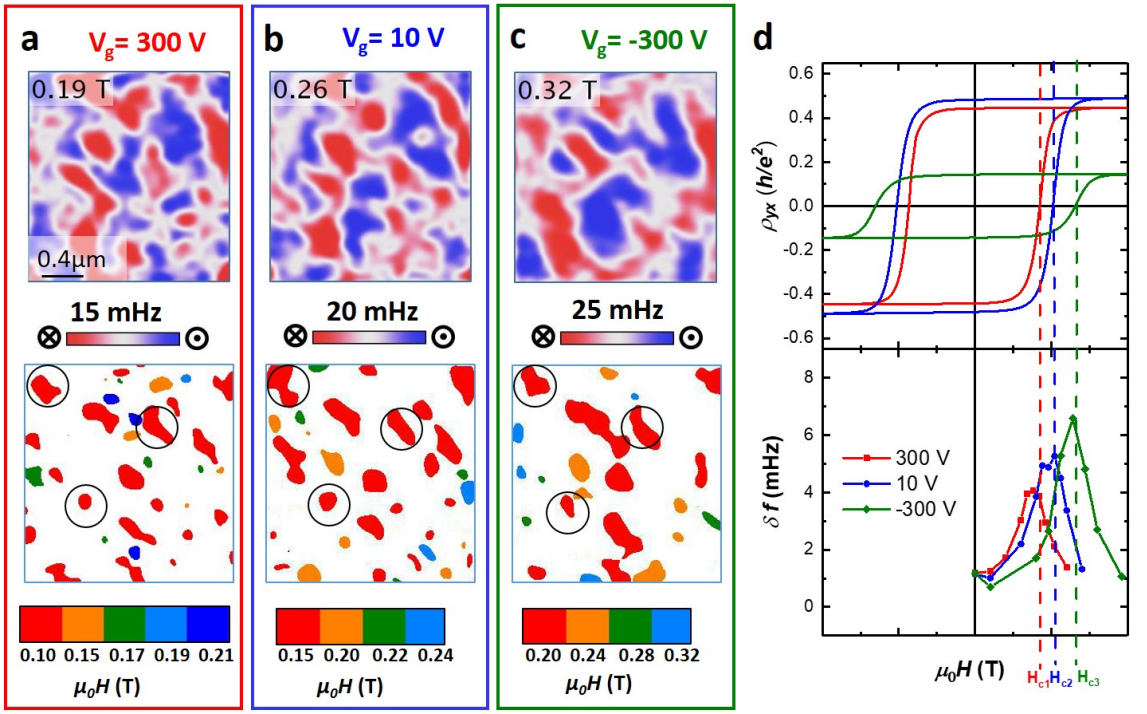

Figure 3.12: | **Gate dependence of ferromagnetic behavior.** (a)-(c) MFM images around the coercive field and nucleation-site maps, at $V_g = 300\,\mathrm{V}$, $10\,\mathrm{V}$ and $-300\,\mathrm{V}$, respectively. Larger domain size and stronger domain contrast were observed in the $V_g = -300\,\mathrm{V}$ (hole-doping). Black circles label some of the common nucleation sites at three different V_g values. (d) The Hall resistance (top panel), MFM domain contrast (δf_{rms}) (bottom panel) as a function of magnetic field at three different V_g values. The H_C deduced from two panels are consistent with each other, as $H_{C1} \approx 0.21\,\mathrm{T}$ ($V_g = 300\,\mathrm{V}$), $H_{C2} \approx 0.26\,\mathrm{T}$ ($V_g^0 = 10\,\mathrm{V}$), $H_{C3} \approx 0.33\,\mathrm{T}$ ($V_g = -300\,\mathrm{V}$).

So the saturated magnetization at zero temperature $M_S(0)$ is independent of gate voltage. Therefore, the enhancement of the magnetization at 5 K indicates a decrease in the reduced temperature T/T_C, *i.e.*, an increase of T_C due to enhanced exchange coupling in the hole-doped films. This is also consistent with higher H_C and fewer nucleation sites in the hole-doped state, suggesting the presence of RKKY mechanism. Therefore, the gating dependence of the MFM results indicates that both Van Vleck and RKKY mechanisms are present in magnetically doped TIs. Interestingly, some nucleation sites (labeled by black circles) are independent of gate voltage, so they are likely caused by neutral defects or imperfections that are insensitive to charge carriers. On the other hand, there are nucleation sites that do depend on the gate voltage, which indicates that they might be related to

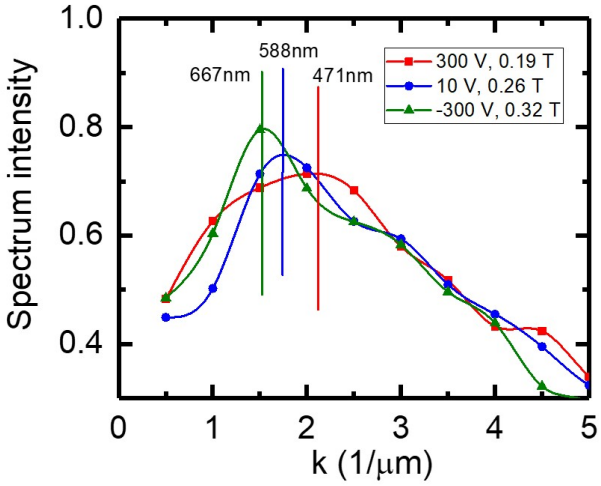

Figure 3.13: **Radial Fourier transform spectrum (azimuthally averaged) of MFM images taken at H_C with different gate voltages.** The spectra show a peak at wave vectors (k=$2\pi/\lambda$) corresponding to wavelength of $\lambda \sim 667$, 588, and 471 nm for $V_g = -300, +10,$ and $+300$ V, respectively.

charged defects.

The V_g-dependence of ρ_{yx} and H_C are summarized in Fig. 3.14(a). The $\rho_{yx}(V_g)$ curve was measured at zero magnetic field with a slow ramping of V_g from -300 V to $+300$ V after the film was saturated at high field. The $\rho_{yx}(V_g)$ shows a peak at $V_g^0 \approx 10$ V, the charge neutral point. This result agrees well with the saturation state resistance from hysteresis loop measurements (red stars), indicating the single-domain state at zero magnetic field is robust against tuning the bulk carrier density, *i.e.*, robust ferromagnetism. In contrast to the monotonic gate dependence of the coercive field H_C, ρ_{yx} shows a non-monotonic behavior, consistent with the proximity of the Dirac point to the VBM in BST, as shown in Fig. 3.14(b) [3, 14, 38]. The hole-doping will not only enhance exchange interaction via an RKKY type exchange mechanism, but will also significantly enhance dissipation, thus reducing ρ_{yx}. On the other hand, electron-doping pushes the Fermi level up above the VBM, but presumably below the conduction band minimum (CBM). Therefore, electron-doping likely only induces surface state carriers with slightly enhanced dissipation. Previous ARPES studies of V-doped BST film suggest that the Dirac point is below the VBM, so the

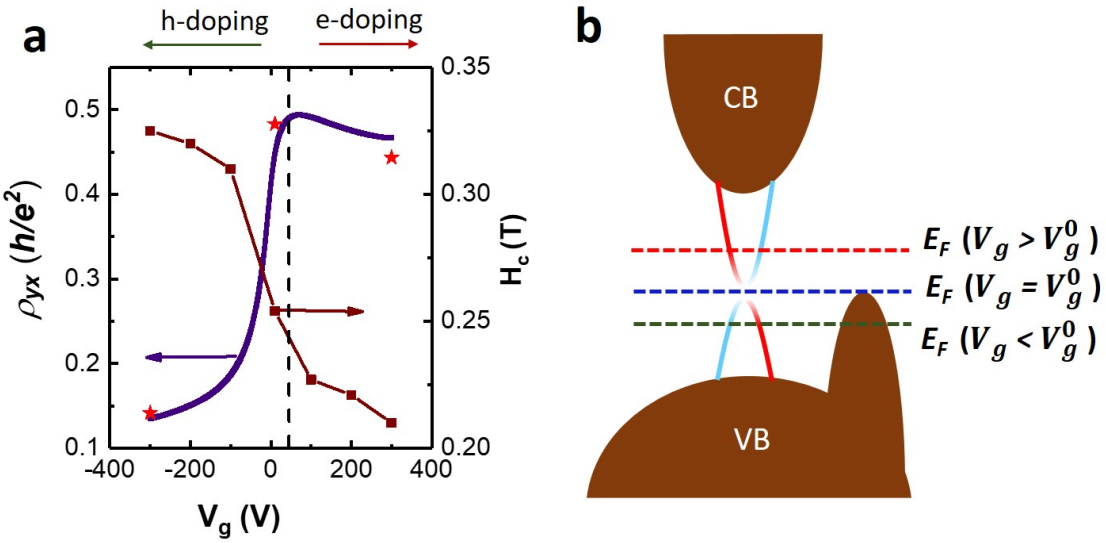

Figure 3.14: | **Gate dependence of ρ_{yx} & H_C and schematic band structure. a**, ρ_{yx} and H_C vs. V_g. Red stars are the zero-field ρ_{yx} from hysteresis loops at -300 V, 10 V and 300 V. **b**, Schematic picture of the band structure of the Cr/V co-doped BST film. The Dirac point of the surface state is close to the VBM.

mass gap overlaps with bulk states [42]. In contrast, transport studies indicate the Dirac point is above the VBM for Cr doped BST films [3, 14]. Therefore, it is possible that Cr doping in co-doping samples slightly lowers the VBM so that it is easier to localize the bulk states inside the mass gap, see Fig. 3.15. Alternatively, Cr/V co-doping might significantly enhance scattering of bulk carriers, resulting in enhanced localization of in-gap bulk states. Further studies of the impact of dopants on magnetic exchange and transport are needed to understand the mechanism of enhanced QAHE temperature in co-doped samples. The observed robust ferromagnetism resolves one of the major concerns in magnetically doped topological insulators, and opens a door to explore high-temperature dissipationless conduction with magnetic topological materials.

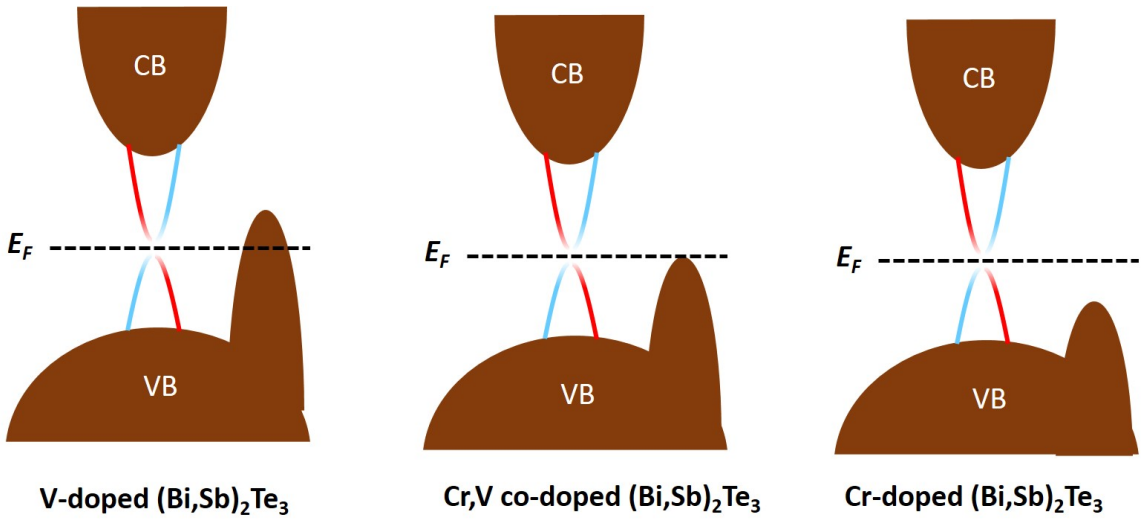

Figure 3.15: **Schematic diagrams of the band structures of V-doped, Cr/V co-doped and Cr-doped BST films.**

3.3 Direct evidence of the antiparallel magnetization alignment in a quantum anomalous Hall heterostructure for realizing axion insulator state

In the previous section, we discussed the ferromagnetic domains in single-layer quantum anomalous Hall systems. In this section, we will talk about quantum anomalous Hall heterostructures, which exhibits axion insulator state. As mentioned in 1.1.4, axion insulators are very appealing to physicists, due to its unique quantum properties, such as the quantized magneto-optical effect[49, 50], the topological magneto-electric effect (TME)[3, 36, 37], and the magnetic monopole[51]. One of the main criteria for realizing the axion insulating state is the antiparallel magnetization alignment. In this section, we will discuss the direct evidence of the antiparallel magnetization alignment in a quantum anomalous Hall heterostructure, by using the cryogenic MFM technique[15].

A 3D FM-TI-FM QAH sandwich heterostructure has been proposed for realizing axion insulating state. It has been shown that magnetically doped TI layers can be epitaxially grown on an undoped Ti layer and vice versa to form the required FM-TI-FM sandwich

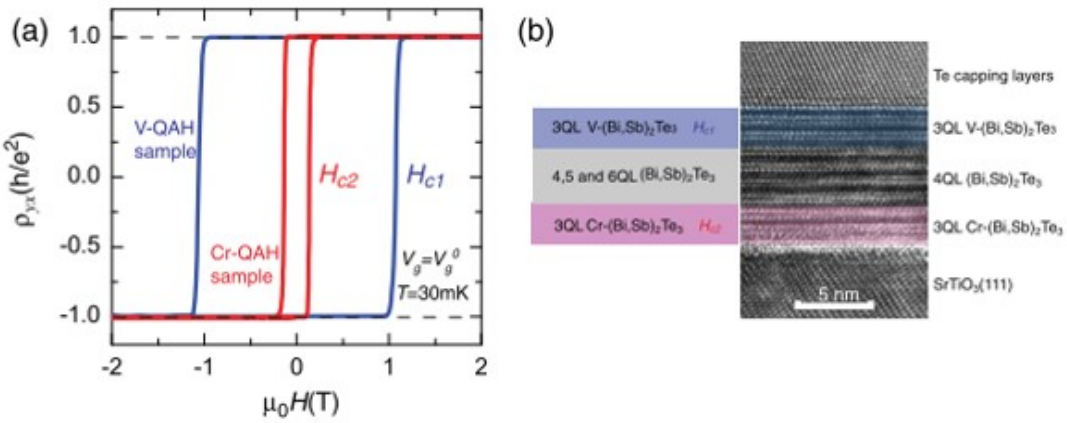

Figure 3.16: (a) QAHE in individual Cr- and V-doped BST films measured at $T = 30\,\mathrm{mK}$. The H_C of the V-doped QAH film $H_{C1} \sim 1.06\,\mathrm{T}$; the H_C of the Cr-doped QAH film $H_{C2} \sim 0.14\,\mathrm{T}$. (b) Schematic drawing and cross-sectional TEM image of V-doped BST/BST/Cr-doped BST QAH sandwich heterostructure. Adapted from Ref.[15].

heterostructures[41, 52, 65]. If the top and bottom BST layers are doped with two different magnetic ions, specifically, Cr- and V-, and the interlayer coupling strength (H_E) is substantially smaller than the difference ΔH_C between the coercive field (H_C) of the two magnetic layers, an antiparallel magnetization alignment may appear when the external H lies between two H_Cs[15, 56]. As shown in Fig. 3.16(a), the coercive field of Cr- and V-doped BST films at 30 mT are, respectively, $\sim 0.15\,\mathrm{T}$ and $\sim 1\,\mathrm{T}$. The significant difference between these two H_Cs make it promising to realize the antiparallel magnetization alignment.

The V-doped BST/BST/Cr-doped BST QAH sandwich heterostructures are grown on $SrTiO_3$(111) substrate in a molecular beam epitaxy (MBE) chamber. As shown in Fig. 3.16(b), the bottom magnetic layer is 3 QL Cr-doped BST, and the top magnetic layer is 3 QL V-doped BST. The undoped BST film separating two magnetic layers have thickness of 5 QL. The relatively thick spacing layer is utilized to reduce H_E and prevent the hybridization of the top and bottom surface states[134–136].

Fig. 3.17(b) shows the Hall conductance loop measured at 30 mK, when the Fermi level is tuned to the charge neutral point, *i.e.*, $V_g = V_g^0$. At high field, when the magnetization of top and bottom layers are aligned in the same direction, the heterostructure shows QAH state ($\sigma_{xy} = e^2/h$). At intermediate state, when $H_{C2} < H < H_{C1}$ (or $-H_{C2} > H > -H_{C1}$),

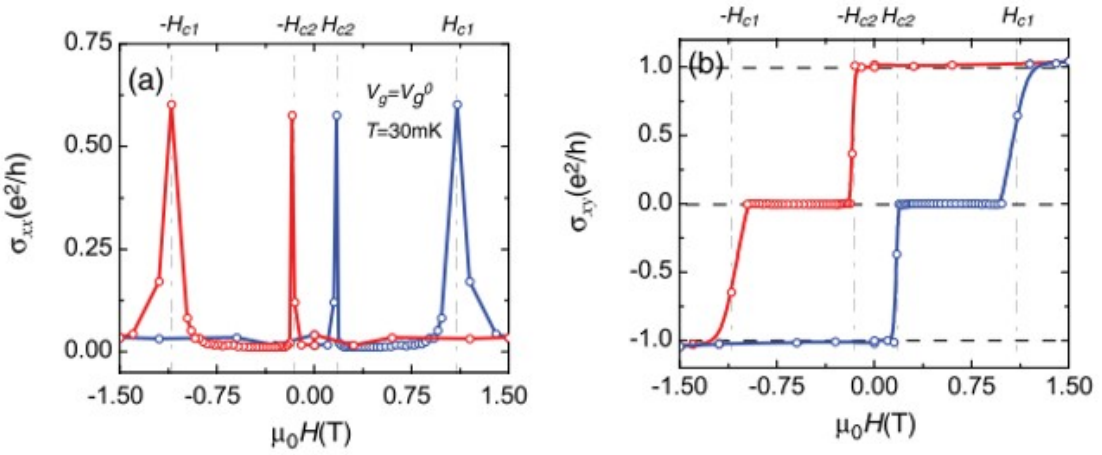

Figure 3.17: $\mu_0 H$ dependence of σ_{xx} (a) and σ_{xy} (b) of 3-5-3 heterostructure at $V_g = V_g^0$ and $T = 30\,\mathrm{mK}$. An axion insulator is observed if the zero σ_{xy} plateau results from the anitparallel magnetization alignment. Adapted from Ref.[15].

the Hall conductance σ_{xy} shows a zero plateau. In these cases, the top and bottom surfaces can be regarded as half-integer QAH states with $\sigma_{xy}^t = -0.5e^2/h$ and $\sigma_{xy}^b = 0.5e^2/h$ (or $\sigma_{xy}^t = 0.5e^2/h$ and $\sigma_{xy}^b = -0.5e^2/h$), leading to zero σ_{xy} plateau and eliminating the 1D chiral edge states.

As discussed in 1.1.4, the zero Hall conductance plateau is not a concrete proof of axion insulating state, because it has been observed in single-layer QAH samples, where it results from the large ρ_{xx} of the multi-domain state at H_C[53–55]. In contrast, the zero σ_{xy} plateau observed here, as we will show below, results from the cancellation of the top and bottom surface conduction in the antiparallel magnetization alignment, consistent with an axion insulator. In order to demonstrate the antiparallel magnetization alignment in the zero σ_{xy} plateau regions, we carried out MFM measurements.

Fig. 3.18(a)-(n) show MFM images at 5.3 K and $V_g = 0$, as the magnetic field sweeping from $-0.01\,\mathrm{T}$ to $-0.75\,\mathrm{T}$. The heterostructure was initially saturated at $1\,\mathrm{T}$, *i.e.*, top and bottom layers are both magnetized upward (red). At $-0.01\,\mathrm{T}$, the heterostructure stays in the saturation state (red), indicating a strong uniaxial anisotropy. As the field swept to more negative fields, some green domains nucleate, suggesting the magnetization reversals of

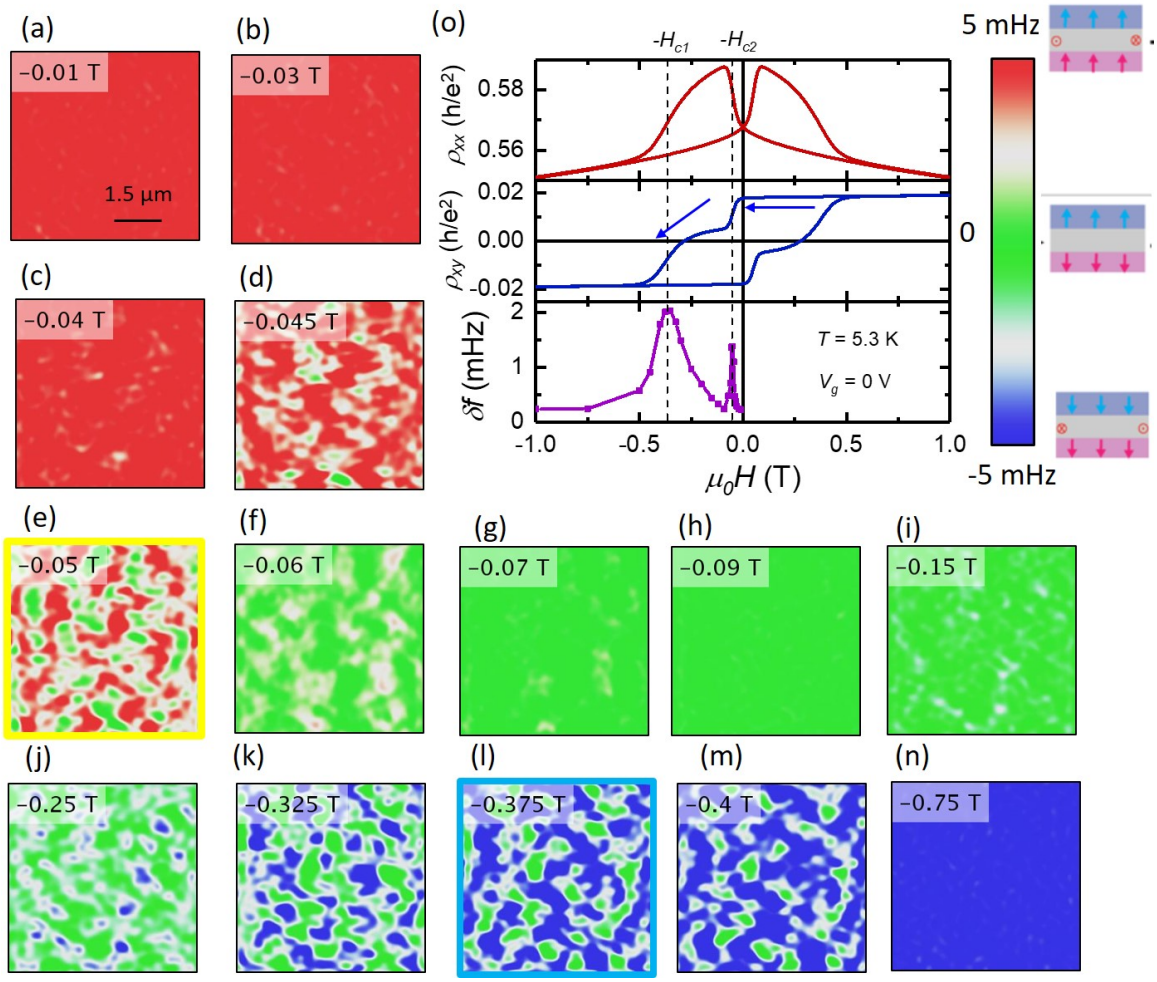

Figure 3.18: (a)-(n)5.3 K MFM images measured at various magnetic fields from −0.01 T to −0.75 T at $V_g = 0$. (o)*In-situ* transport data of ρ_{xx} (red) and ρ_{yx} (blue). The purple curve indicates the roughness of MFM images δf at various magnetic fields.

the Cr-doped BST layer. At these green regions, Cr-layer is reversed, while V-layer remains upward. At $H_C \sim -0.05$ T, it shows the fifty-fifty domain population. At $H_{C2} \sim -0.09$ T, the entire area becomes green. This is a strong evidence of antiparallel magnetization alignment, since no domains are visible at this intermediate state, in sharp contrast to Cr-modulation-doped QAH heterostructures, which exhibit multi-domains at the zero σ_{xy} plateau regime. Further sweeping the field leads to the magnetization reversals of the V-doped BST layer, as the blue domains start to nucleate. The fifty-fifty domain state is observed at $H_{C1} \sim -0.375$ T. The heterostructure is finally saturated at −0.75 T, as the entire area becomes blue. *In-situ* transport measurements were performed simultaneously,

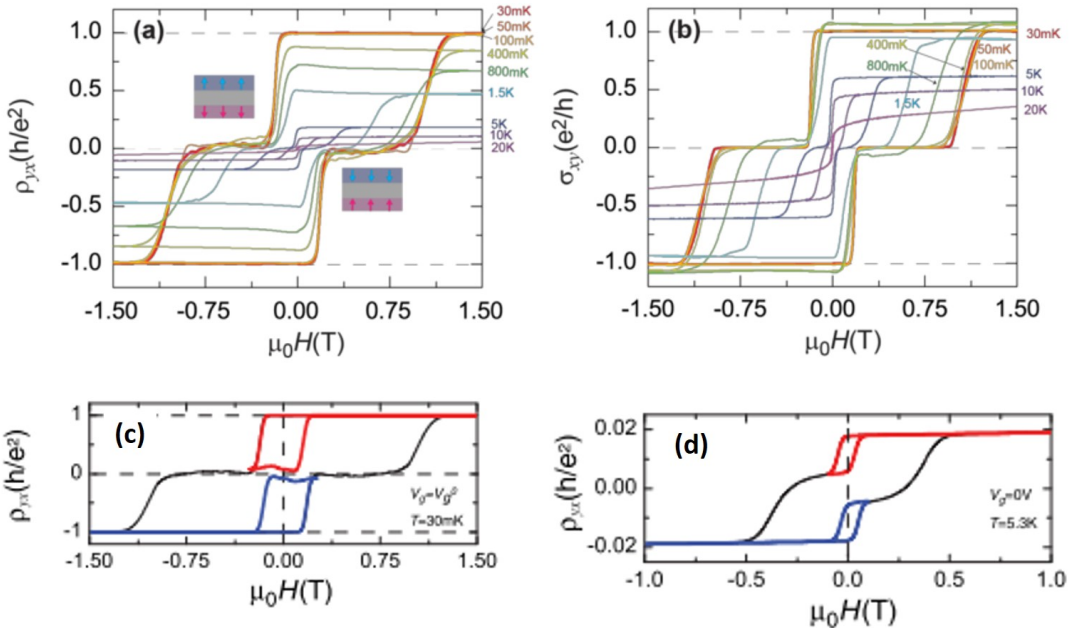

Figure 3.19: The $\mu_0 H$ dependence of ρ_{yx} (a) and σ_{xy} (b) at different temperatures. Both $\sigma_y x$ and σ_{xy} exhibit two-step magnetization transition for $T < 10\,\mathrm{K}$. Minor loops of the ρ_{yx} at $V_g = V_g^0$ and $T = 30\,\mathrm{mK}$ (c) and at $V_g = V_g^0$ and $T = 5.3\,\mathrm{K}$ (d). Adapted from Ref.[15].

as shown in Fig. 3.18(o). The two-step magnetization reversal process was also verified by the ρ_{yx} loop. The roughness of MFM images (δf) was plotted as the purple curve in Fig. 3.18(o), which shows double peaks. These two peaks correspond to the coercive field of the top and bottom layer (H_{C1} and H_{C2}), in excellent agreement with the transport data. Our MFM measurements demonstrated the presence of antiparallel magnetization alignment at 5.3 K. It is reasonable to expect such behavior to persist to lower temperatures that bring out the QAH state.

Figure 3.19(a)(b) show the $\mu_0 H$ dependence of ρ_{yx} and σ_{xy} over the temperature range $30\,\mathrm{mK} < T < 20\,\mathrm{K}$. Both ρ_{yx} and σ_{xy} exhibit a two-step transition feature up to $T = 10\,\mathrm{K}$. The two-step feature sharpens with decreasing temperature showing zero ρ_{yx} and σ_{xy} plateaus for $T < 1.5\,\mathrm{K}$. To confirm the antiparallel magnetization alignment in zero ρ_{yx} and σ_{xy} plateaus regions at $T = 30\,\mathrm{mK}$, we compared the minor loops at $T = 30\,\mathrm{mK}$ with $V_g = V_g^0$ and $T = 5.3\,\mathrm{K}$ with $V_g = 0\,\mathrm{V}$. The H_E can be estimated by $H_\mathrm{E} = (|H^L_{\mathrm{C,minor}} - H^R_{\mathrm{C,minor}}|/2)$, where $H^L_{\mathrm{C,minor}}$ and $H^R_{\mathrm{C,minor}}$ denote the left and right H_C of

minor loops[137, 138]. The H_{E}s at $T = 30\,\mathrm{mK}$ and $T = 5.3\,\mathrm{K}$ are ∼115 and ∼84 Oe, respectively. Since the H_{C}s of two magnetic TI layers are also functions of T, we define a relative H_{E} value $\alpha = [H_{\mathrm{E}}/(H_{\mathrm{C1}} - H_{\mathrm{C2}})]$ to compare the interlayer coupling strengths at different Ts.We find that $\alpha \sim 0.0013$ at $T = 30\,\mathrm{mK}$ and ∼0.028 at $T = 5.3\,\mathrm{K}$. With the MFM observation at 5.3 K, the smaller α at $T = 30\,\mathrm{mK}$ confirms not surprisingly the robust antiparallel magnetization alignment in the zero ρ_{yx} and σ_{yx} plateau regions. Therefore, the axion insulator state is indeed realized in the zero ρ_{yx} and σ_{yx} plateau regions at $T = 30\,\mathrm{mK}$.

Chapter 4

Topological Hall effect in ultra-thin $SrRuO_3$ films

In this chapter, we will switch from momentum space Berry phase phenomena to a real space one, namely the topolgical Hall effect (THE). The THE originates from scalar spin chirality, the solid angle subtended by non-coplaner spin texture[11, 63]. As an electron traveling through the non-coplaner spin texture, it will experience an effective magnetic field. This field, originating from the Berry phase picked up by the electron as it hops between magnetic moments, will in turn give rise to a Hall effect known as the THE, to be distinguished from the ordinary Hall effect which does require the application of an external magnetic field.

4.1 Chiral fluctuation driven topological Hall effect

While the THE is usually interpreted as a signature of static topological spin textures, it has been proposed that chiral fluctuation of spins could also result in significant anomalous Hall effect (AHE) in double-exchange magnets such as manganites [139–141], or two-dimensional (2D) chiral magnets [142]. However, the conventional mechanisms of AHE cannot be excluded [11, 143].

In this section, we will discuss the unambiguous evidence of chiral fluctuation driven THE in a seemingly symmetric heterostructure of $SrTiO_3$ (STO) capped $SrRuO_3$ (SRO) thin films grown on STO substrate, a 2D ferromagnet with perpendicular uniaxial anisotropy. A substantial THE was observed in SRO films with thickness (t) ($3 \sim 6$ u.c.) in a wide temperature range around the ferromagnetic transition temperature T_C. Remarkably, the

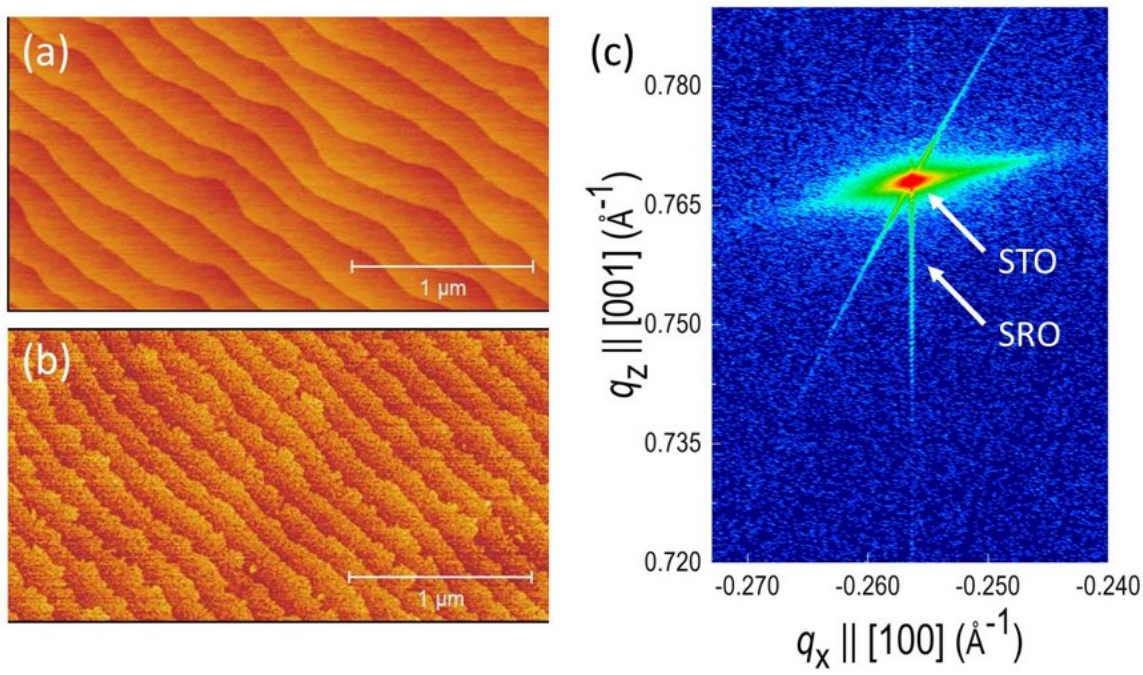

Figure 4.1: Surface morphology of (a)TiO_2 terminated STO (001) substrate and (b) 2 u.c. STO capped 5 u.c. SRO film. (c) Reciprocal space mapping of (103) peak of the film, indicating that the film is fully coherent with STO substrate.

observed THE persists well above T_C into the paramagnetic phase, indicating its origin in chiral-fluctuation-induced topological charge. The experimental observation is in excellent agreement with our Monte Carlo simulations of a 2D uniaxial ferromagnet with chiral interaction, which provides compelling evidence of chiral fluctuation driven topological responses.

Both the $SrRuO_3$ (SRO) and $SrTiO_3$ (STO) layers were epitaxially grown on TiO_2 terminated (001) STO substrates using pulsed laser deposition (PLD) technique. The single TiO_2 terminated STO substrates were achieved by standard buffer HF etching for 30 s and subsequent annealing at 950 °C for 90 min. Fig. 4.1(a) shows an example of the surface morphology of an as-treated STO substrate by atomic force microscopy (AFM), revealing atomically smooth surface with clear terrace structure. During the growth of either SRO or STO, the laser fluence and repetition rate are 2 J/cm^2 and 1 Hz, respectively. The substrate

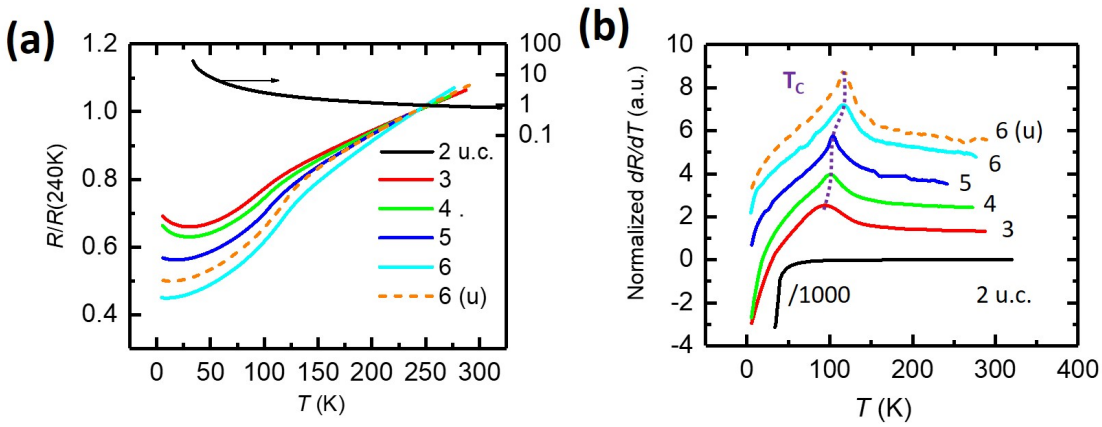

Figure 4.2: **Longitudinal resistance R_{xx} of STO capped SRO ($2 \leq t \leq 6$) and uncapped 6 u.c. SRO films** (a) Temperature dependence of normalized longitudinal resistance $R/R(240\,\mathrm{K})$ at zero magnetic field for capped $2 \leq t \leq 6$ and uncapped 6 u.c. (orange dashed curve). (b)First order derivative of longitudinal resistance $\mathrm{d}R/\mathrm{d}T$ for $2 \leq t \leq 6$ and uncapped 6 u.c. (orange dashed curve). The Curie temperature T_C can be indicated by the derivative peak, which is labelled by the dashed purple line.

temperature and oxygen partial pressure during growth are 650°C and 0.25 mBar, respectively. In-situ reflection high-energy electron diffraction (RHEED) was used to monitor the growth and confirmed a layer by layer growth fashion. All the films show atomic flat surface with similar terrace structure with substrates. An example of the surface morphology of the 2 u.c. STO capped 5 u.c. SRO film is shown in Fig. 4.1(b). X-ray diffraction (XRD) has been done by PANalytical XPert Materials Research Diffractometer (MRD) in high resolution mode. Reciprocal space mapping (RSM) of (103) diffraction peaks has been performed at room temperature. Fig. 4.1(c) shows RSM of (103) peak of 2 u.c. STO capped 5 u.c. SRO film, indicating that the film is fully coherent with STO substrate.

A cartoon schematic of thin film structure and device configuration is shown in Figure 4.3**a**. Electric contacts were fabricated with wire binding and silver paint. The STO capping layer is crucial to enhance the ferromagnetism in ultrathin limit by suppressing the octahedral tilting[144].The longitudinal resistance R_{xx} was characterized on STO capped SRO films ($2 \leq t \leq 6$). The temperature dependence of normalized longitudinal resistance $R/R(240\,\mathrm{K})$ for $3 \leq t \leq 6$, as shown in Fig. 4.2(a), shows the metallic behavior. At high

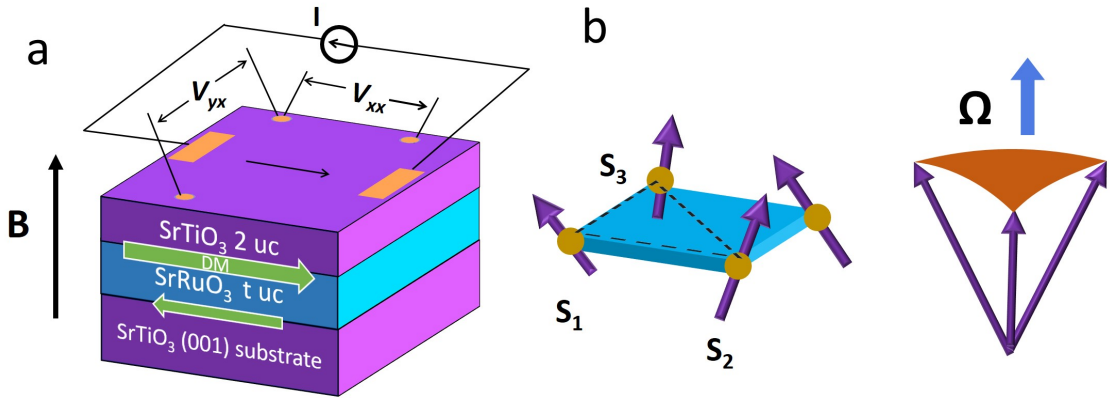

Figure 4.3: **a**, A schematic of the $(\mathrm{STO})_2/(\mathrm{SRO})_t$ bilayer grown on STO (001) and leads for transport measurements. **b**, a snapshot of non-coplaner spins on a square lattice. The three non-coplanar neighbouring spins subtend a solid angle Ω, resulting in effective magnetic field.

temperature, it exhibits a linear relation, which indicates the bad metal behavior[145]. The R_{xx} drops faster around Curie temperature T_C, due to the ferromagnetic ordering[146, 147]. The derivative of R_{xx} respect to T, $\mathrm{d}R_{xx}/\mathrm{d}T$, shows a peak around T_C, as shown in Fig. 4.2(b)[148]. The thickness dependence shows the thinner films are more resistive and have lower T_C. This is consistent with the effect of reduced dimensionality. The 2 u.c. film shows the insulating behavior, suggesting a metal-insulator transition with a critical thickness $t = 3$. The uncapped 6 u.c. SRO films shows $T_\mathrm{C} \approx 117 \pm 2$ K.The critical thickness for uncapped SRO films is reported to be 4 u.c. [149]. Table 4.1 shows the T_C for various SRO films, where T_C^R and T_C^h are T_cs determined by $R_{xx}(T)$ and $h(T)$ (will be discussed later), respectively.

SRO films (u.c.)	3	4	5	6	6 (u)
T_C^R (K)	94±5	100±4	104±1	116±3	117±2
T_C^h (K)	94.7	103.2	105.8	115.6	118.2

Table 4.1: Curie temperature T_C of capped SRO films with various thickness

Figure 4.4 shows the raw Hall data $\rho_{yx}(H)$ of the 6 u.c. sample measured at various temperatures. The ordinary Hall effect (OHE) can be esitmated by the slope of Hall data at high field limited, considering the AHE and THE suppresses at high fields. After subtracting

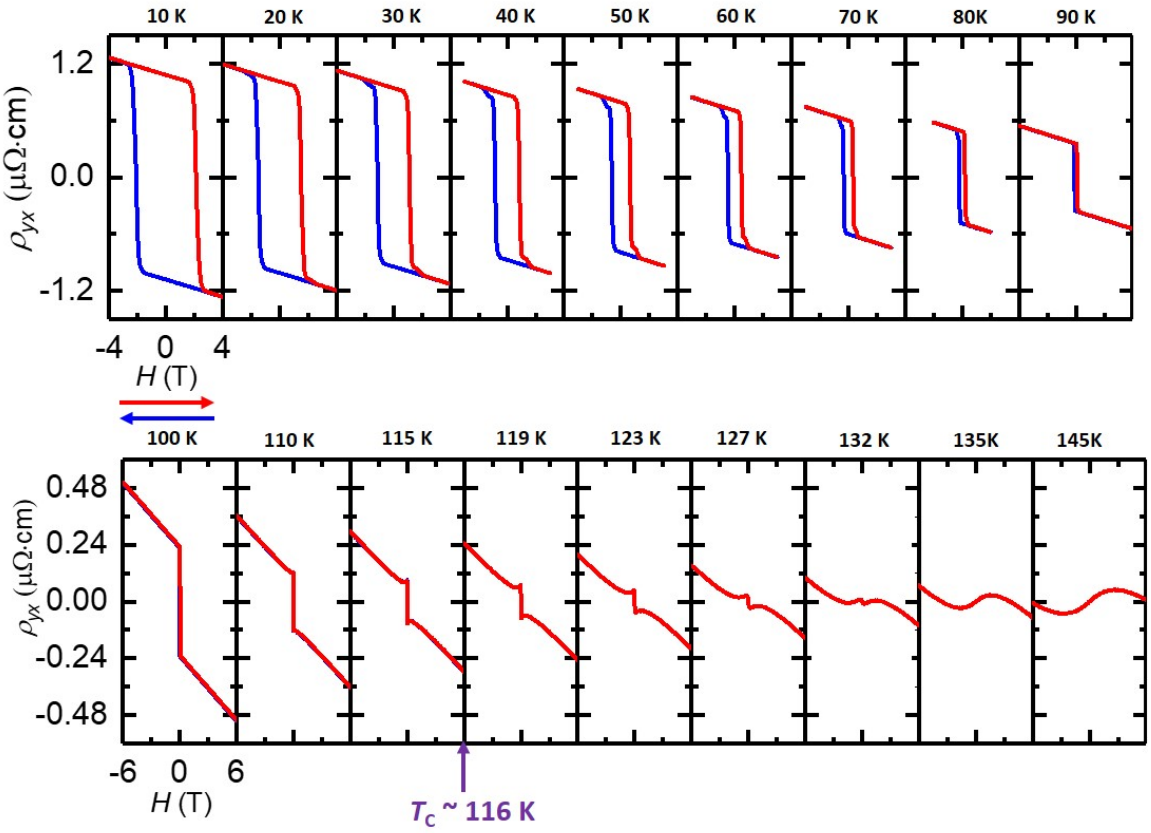

Figure 4.4: | **The raw Hall data of STO capped 6 u.c. SRO film.** Raw Hall data after antisymmetrization, as a function of magnetic field H at various temperatures from 10 K to 145 K. Blue (red) curves were taken as the magnetic field from −6 to 6 T (6 to −6 T). The cyan arrows indicate the THE humps emerge above 100 K.

the OHE, which is proportional to H, the $\rho_{yx}(H)$ data show a pronounced square shape at low temperatures, as shown in Figure 4.5, indicating a robust ferromagnetic ordering. The coercive field gradually decreases to zero above 100 K so that the hysteresis is negligible. Remarkably, a sharp peak was found near zero field, indicating additional contribution [65–68].Thus our Hall data indicate three contributions: the OHE ($\rho_{yx}^{\mathrm{O}} = R_0 H$), the AHE ($\rho_{yx}^{\mathrm{A}} = R_S M$), and the THE ($\rho_H^{\mathrm{T}}$).

$$\rho_{yx}(H) = R_0 H + R_S M + \rho_H^{\mathrm{T}}, \tag{4.1}$$

More remarkably, the THE becomes more pronounce near T_{C}, and persists all the way up to 132 K, 16 K above the $T_{\mathrm{C}} \approx 116$ K, well into the paramagnetic phase. Its magnitude

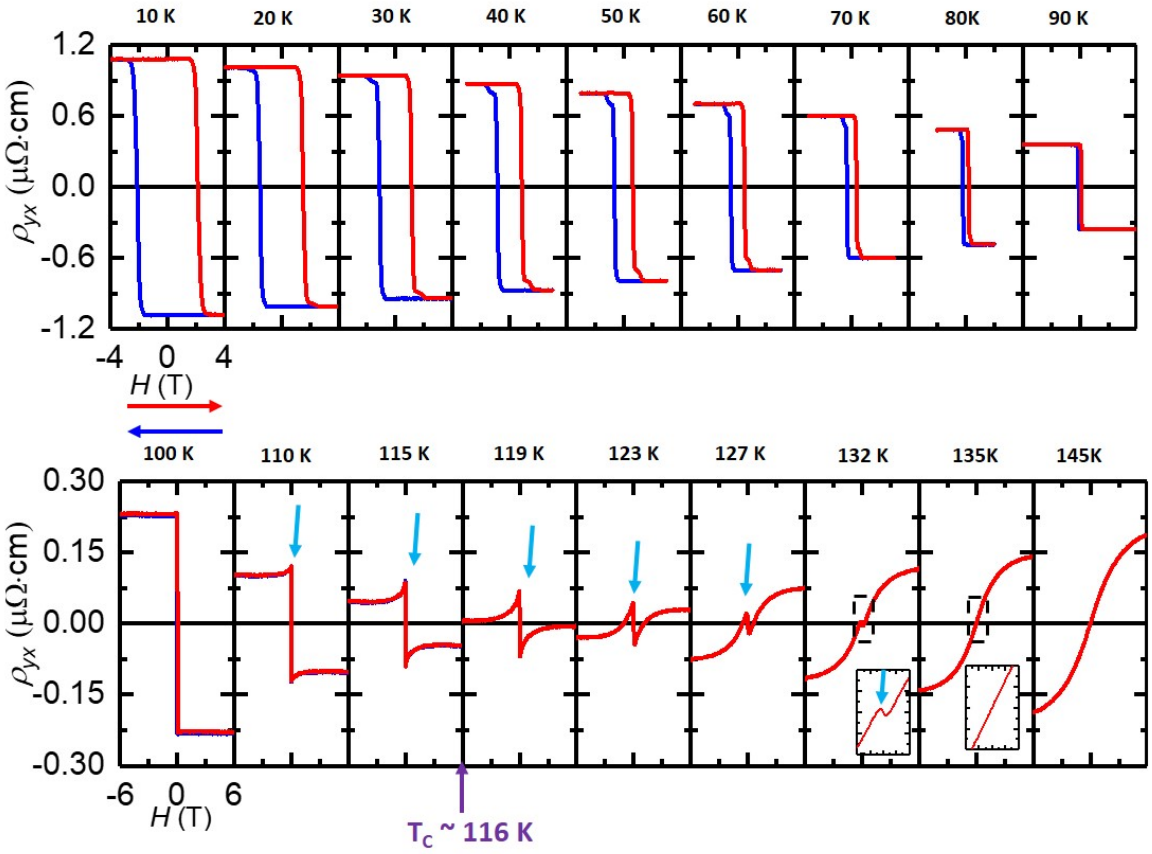

Figure 4.5: | **The anomalous Hall data of STO capped 6 u.c. SRO film.** Anomalous Hall resistivity ρ_{yx} (with OHE subtracted) as a function of magnetic field H at various temperatures from 10 K to 145 K. Blue (red) curves were taken as the magnetic field from -6 to 6 T (6 to -6 T). The cyan arrows indicate the THE humps emerge above 100 K. The insets show zoomed-in curves of 132 and 135 K data around zero field, suggesting the THE peaks are absent above 135 K.

gradually diminishes at higher temperatures and is undetectable above 135 K, which suggests a dynamical origin of the THE above T_C [142]. To reveal the intrinsic behavior of the THE, we utilize the fact that the AHE (R_S) of SRO changes sign at intermediate temperature due to strong energy dependence of the Berry phase near the Fermi energy[68, 150]. For our 6 u.c. SRO film, the AHE changes its sign at approximately 119 K so that the $\rho_{yx}(H)$ data is dominated by the THE. As shown in Fig. 4.5, the field dependence of the THE at 119 K shows a sharp antisymmetric peak near zero field followed by a smooth suppression at high fields, which is consistent with the suppression non-coplanar spin texture shown in Fig. 4.3**b**.

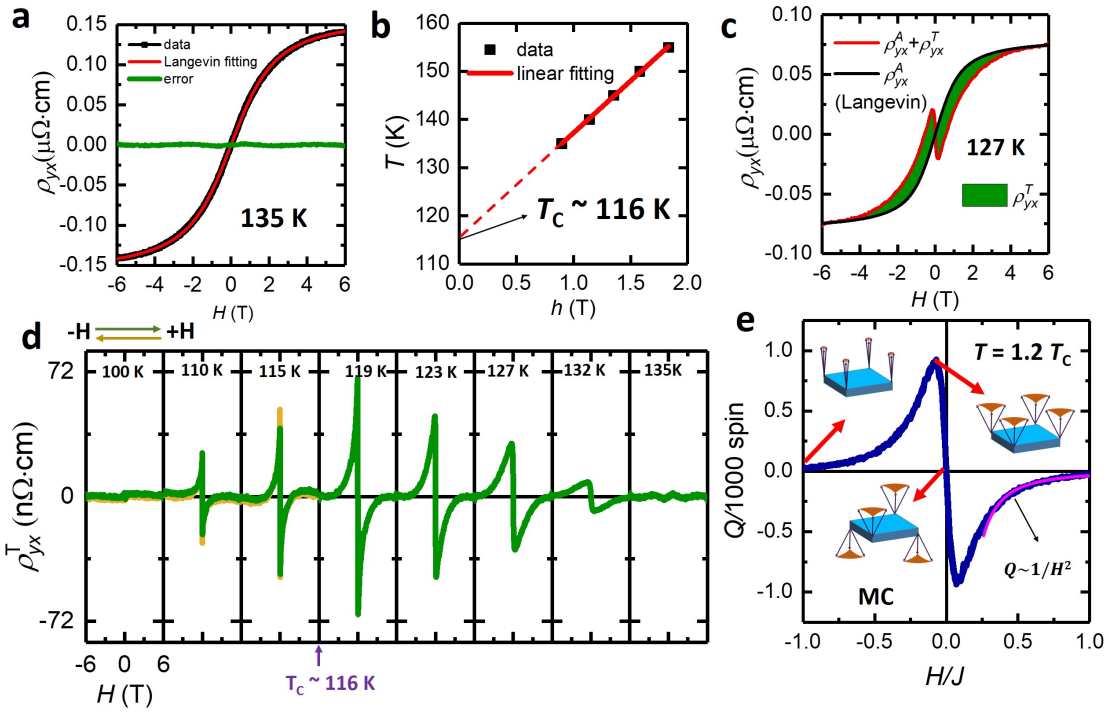

Figure 4.6: | **The THE signal ρ^{T}_{yx} of STO capped 6 u.c. SRO films.** **a**, ρ_{yx} (black) at 135 K was fitted with a Langevin function (red). The green curve is the residue of the fitting. **b**, T as a function of the fitting parameter h shows a linear relation, indicating $T_{\mathrm{C}} \approx 116$ K. **c**, ρ_{yx} at 127 K deviates from expected AHE ρ^{A}_{yx} (Langevin function). The difference indicated by the green area is THE signals ρ^{T}_{yx}. **d**, ρ^{T}_{yx} as a function of magnetic field H at various temperature from 100 K to 135 K. **e**, MC simulations of topological charges Q at $T = J$ shows an antisymmetric profile similar to the experimental data of the THE. The high field tail can be described by $1/H^2$ (the magenta curve).

To extract the intrinsic topological Hall signal above 110 K, the H dependence of AHE contribution ($\propto M(H)$) needs to be properly removed. For the paramagnetic phase at $T \geq T_{\mathrm{C}}$, the $M(H)$ curves can be described by a Langevin function in the large spin limit. Because the THE contribution becomes negligible for $T \geq 135$ K, these high temperature AHE data are chosen for Langevin fitting. For example, the fitting result of 135 K ρ^T_{yx} data is shown in Fig. 4.6**a** using a Langevin function $M(H) \propto L(x) = \coth(x) - \dfrac{1}{x}$, where $x = \frac{H}{h}$ and $h \equiv \frac{k_B}{\mu}(T - T_{\mathrm{C}})$ is a fitting parameter with k_B the Boltzmann constant and μ the effective order moment. The h values of Hall data at $T \geq 135$K are shown in Fig. 4.6**b**, where h vs. T follow a linear relation. The intercept of the linear fitting gives the same Curie temperature $T^{\mathrm{fit}}_{\mathrm{C}} \approx 116$ K the same as that determined by the dR_{xx}/dT anomaly,

corroborating the validity of the Langevin fitting. Assuming the magnetization and AHE are described by the same function near T_C, the extrapolated h values are used to compute the paramagnetic AHE contribution at $T_C < T < 135\,\mathrm{K}$, as shown in Fig. 4.6**c**. For T below T_C, a step function is used to approximate the AHE contribution. The extracted THE data are shown in Fig. 4.6**d**. The antisymmetric THE peaks are observed in a wide temperature range from 110 K to 132 K, a compelling evidence of thermal fluctuation induced THE[142].

To understand fundamental mechanism of chiral fluctuation driven THE, we carried out Monte Carlo (MC) simulations of a 2D uniaxial ferromagnet with weak chiral interaction (DMI). The Monte Carlo (MC) simulations were conducted on a $N^2 = 32 \times 32$ square lattice with periodic boundary conditions. The Hamiltonian was used as the energy function underlying the standard Metropolis algorithm. The expression of Ω follows:

$$\exp\left(\frac{i\Omega}{2}\right) = r^{-1}(1 + \boldsymbol{S}_1 \cdot \boldsymbol{S}_2 + \boldsymbol{S}_2 \cdot \boldsymbol{S}_3 + \boldsymbol{S}_3 \cdot \boldsymbol{S}_1 + i\chi) \tag{4.2}$$

where $\chi \equiv \boldsymbol{S}_1 \cdot (\boldsymbol{S}_2 \times \boldsymbol{S}_3)$ is the spin chirality of the three neighboring spins [151], and $r = \sqrt{2(1 + \boldsymbol{S}_1 \cdot \boldsymbol{S}_2)(1 + \boldsymbol{S}_2 \cdot \boldsymbol{S}_3)(1 + \boldsymbol{S}_3 \cdot \boldsymbol{S}_1)}$ is the normalization factor. The sign of chirality is fixed by chiral interaction (DMI). The total topological charge (TC) Q is then given by summing Ω over all the right-handed spin triangles in the lattice,

$$Q = \frac{1}{4\pi} \sum_{\triangle_{ijk}} \Omega(\boldsymbol{S}_i, \boldsymbol{S}_j, \boldsymbol{S}_k). \tag{4.3}$$

Q (or χ) is a odd function with respect to time reversal symmetry, so $Q(H) = -Q(-H)$. Thus, for paramagnetic phase with $H = 0$, the net topological charge is zero, $Q(0) = 0$, corresponding to equal populations of "up" and "down" triads. The model Hamiltonian is:

$$H = \sum_{\langle ij \rangle} \left[-J_{ij} \boldsymbol{S}_i \cdot \boldsymbol{S}_j + \boldsymbol{D}_{ij} \cdot (\boldsymbol{S}_i \times \boldsymbol{S}_j)\right] - \sum_i \left[K_i (S_i^z)^2 + B_z S_i^z\right] \tag{4.4}$$

where $\boldsymbol{S}_i = S\mathbf{n}_i$ is the spin on the ith lattice site. The first term, taking positive J, describes ferromagnetic Heisenberg exchange coupling. The second term describes the chiral interaction (DMI) arising from inversion symmetry breaking (at interfaces); here $\boldsymbol{D}_{ij} = D(\hat{z} \times \hat{r}_{ij})$,

the cross product of interface normal $\hat{z}$ with the bond direction $\hat{r}_{ij}$ between sites. The uniaxial magnetic anisotropy K is also included. With $D < D_c \equiv 2\sqrt{2JK}/\pi$, the ground state of the system is a uniaxial ferromagnet despite of the presence of chiral interaction (DMI). The last term describes Zeeman energy, where B_z is the external magnetic field applied in z direction.

Even though our heterostructure appears to be symmetric, it has been shown that the STO film grown on SRO is slightly different from the STO substrate because of in-plane tensile strain[152]. The slight difference that breaks the out-of-plane (OOP) inversion symmetry, which allows a weak but nonzero Dzyaloshinsky-Moriya interaction (DMI)[57, 58] because the heaviest element is ruthenium with moderate SOC strength.

The broken inversion symmetry ($D \neq 0$) allows non-coplanar spin texture, especially when the long range order is "melted" by thermal fluctuation around T_{C}. The non-coplanar spin texture generates fictitious magnetic (gauge) field which is proportional to the solid angle Ω subtended by three neighboring spins as shown in Fig. 4.3**b**. Interestingly, the topological charges $Q(H)$ is not-zero, showing antisymmetric shape, in excellent agreement with the experimental observation of the THE above T_{C}. Thus, the observed THE is a result of effective magnetic (gauge) field generated by thermal fluctuation induced topological charges, as shown in Fig. 4.3**b**. It is interesting to note that although the system's ground state is achiral ($D < D_c$), the thermal fluctuations are chiral due to broken inversion symmetry. Such seemingly incompatible behavior can be understood by symmetry analysis of high temperature expansion ofpartition function [142].

At the low field limit, the induced Q is proportional to magnetic field H. At high field limit, the Zeeman energy competes with DMI, forcing spins to align with the external magnetic field and thus suppressing the solid angle Ω of neighboring spins. Therefore, the THE is suppressed at high magnetic field. In a simple picture, the angle θ between neighboring two spins scales as D/H at the high field limit. Because the solid angle $\Omega(\theta)$ subtended by three neighboring spins is proportional to θ^2, the induced THE is proportional

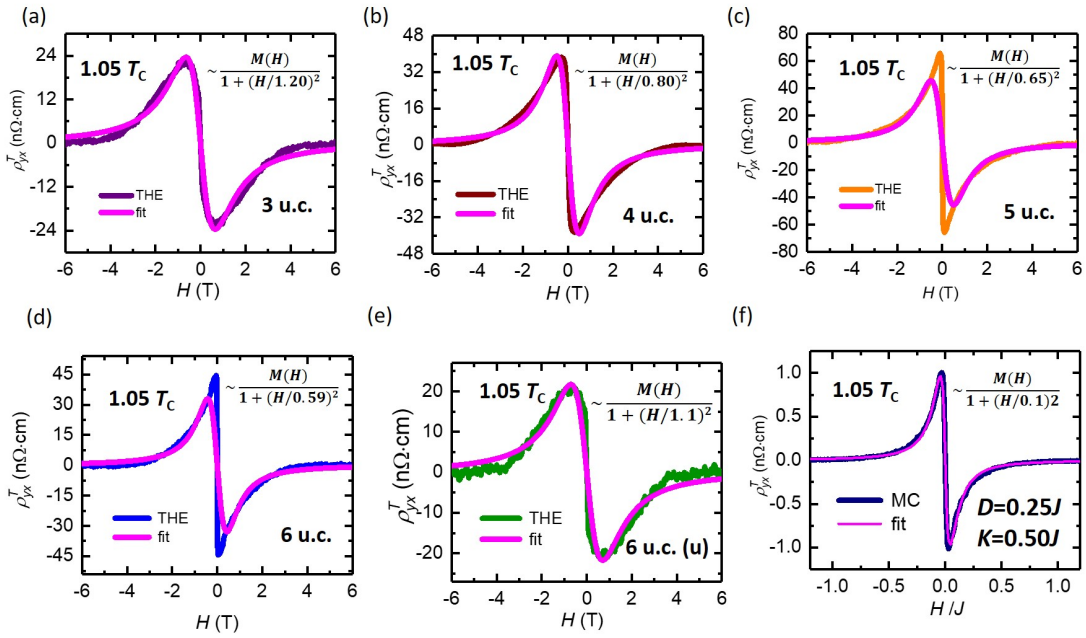

Figure 4.7: (a)Fitting of the THE as a function of magnetic field for capped $t = 3, 4, 5, 6$ at $1.05\,T_C$.(b) Fitting of Q as a function of magnetic field for disorder-free MC simulations at $1.05T_C$.

to $(D/H)^2$ at high magnetic field. As illustrated in Fig. 4.6**e**, the high field behavior of TC indeed follows $1/H^2$ dependence. Combining both limits, we propose a phenomenological function:

$$Q(H) \propto \frac{M(H)}{1+(aH)^2} \tag{4.5}$$

where $a \propto 1/D$.

Fig. 4.7 shows both the THE from transport measurements and the Q from MC simulations can be reasonably fitted by this empirical function. The fitting gives the effective D ($D_{eff} = 1/a$) for capped 3 u.c. , 4 u.c. , 5 u.c. , 6 u.c. and uncapped 6 u.c. SRO film, respectively, 1.20 T, 0.80 T, 0.65 T, 0.59 T and 1.1 T, which correspond to energy scales: 69.6 μeV, 46.4 μeV, 37.7 μeV, 34.8 μeV and 63.8 μeV. This is two order of magnitude less than the exchange coupling strength $J \approx 9$ meV, estimated by the Cuire temperature $T_C \approx 100$ K. The D_{eff} estimated by fitting for the MC simulation is $\approx 0.1\,J$, which has the same order magnitude as the used MC value $D = 0.25\,J$. This confirms the validity of using this empirical function fitting to estimate the D values.

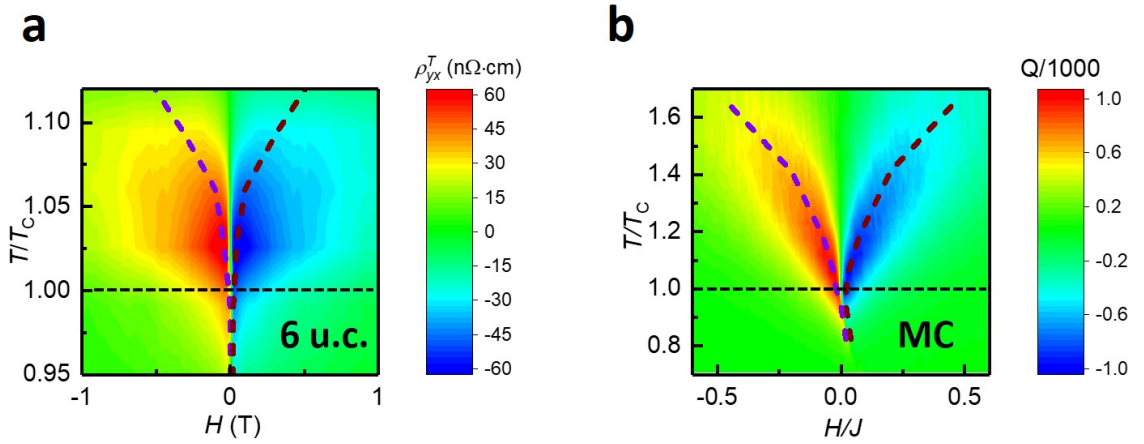

Figure 4.8: | T-H **intensity maps of the THE (6 u.c.) and topological charge** Q **from MC simulations.** **a**, the THE intensity map of STO capped 6 u.c. SRO film as a function of T/T_c and H. **b**, the disorder-free MC simulation of Q intensity map as a function of T/T_c and H. The dashed lines trace the maximum THE values of each field scan.

In addition to agreement in magnetic field dependence, the temperature dependence of the THE is also qualitatively consistent with MC simulation. To compare the overall T and H dependence, we construct an intensity map of ρ_{yx}^{T} in the T-H phase diagram shown in Fig. 4.8**a**. The contour lines show a heart shape, where the THE is most pronounced around T_{C}. The THE peak extends to higher magnetic field above T_{C}, supporting the thermal fluctuation mechanism. The overall T and H dependence is also qualitatively reproduced in the results of MC simulations, as shown in Fig. 4.8**b**.

This agreement provides compelling evidence that the THE in the SRO capped SRO films originates from the chiral fluctuation induced topological charges in a 2D ferromagnet. At high T and low B, the THE is significantly suppressed, approximately following a scaling behavior $\rho_{yx}^{\mathrm{T}} \propto B/(T-T_{\mathrm{C}})^{\alpha}$, *i.e.* $\ln((d\rho_{yx}^{\mathrm{T}}/dB)_0) = -\alpha \ln((T-T_{\mathrm{C}})/T_{\mathrm{C}}) + C$, where $(d\rho_{yx}^{\mathrm{T}}/dB)_0$ is the first derivative of Q respect to B at $B=0$. For capped $3 \sim 6$ u.c. and uncapped 6 u.c. , α falls in the range $3 \sim 4$, as shown in Fig. 4.9. The disorder-free MC simulations give the $\alpha \approx 2.9$, consistent with experimental data. However, the precise nature of the scaling behavior of the THE requires higher resolution measurements and simulations, which would inspire future studies.

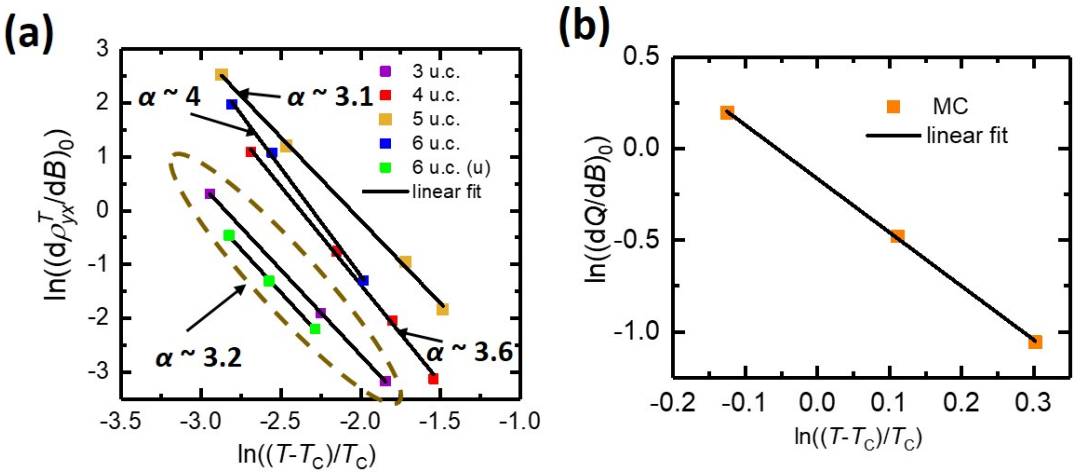

Figure 4.9: $\ln((d\rho_{yx}^T/dB)_0)$ vs $\ln((T-T_{\rm C})/T_{\rm C})$ for capped $3\sim6$ u.c. and uncapped 6 u.c. at high temperature limit. (b) $\ln((dQ/dB)_0)$ vs $\ln((T-T_{\rm C})/T_{\rm C})$ for disorder-free MC simulations at high temperature limit.

Chiral fluctuation induced THE was also observed in thinner SRO films $t=3,4,5$, showing similar T and H dependence. (See 4.1.1) Fig. 4.10**a** shows the maximum topological Hall signals $\rho_{yx}^{\rm T}$ as a function of reduced temperature $T/T_{\rm C}$. Clearly, the THE peaks around $T_{\rm C}$. The quantitative differences likely come from the combination of DMI other parameters (*e.g.* effective exchange J and magnetic disorders) that vary with the film thickness, which would complicate the thickness dependence of the THE magnitude. As shown in Fig. 4.10**b**, the width of the THE peak, which is proportional to effective DMI ($D_{\rm eff}$), reduces systematically the film thickness increases. Here $D_{\rm eff}=D/t$ because D mainly comes from the interfaces where the inversion symmetry is broken. The normalized THE ρ^T/ρ_m^T in thinner films show larger peak widths, indicating stronger $D_{\rm eff}$. Using the phenomenological function in Eq. (4.5), we extracted $D_{\rm eff}\approx 1/a$ of the capped (3, 4, 5, and 6 u.c.) and uncapped (6 u.c.) SRO films. As shown in Fig. 4.10**c**. $D_{\rm eff}$ of uncapped films decreases as thickness increases, in excellent agreement with the interface origin. The estimated interface D value is approximately 0.2 meV, almost 2 orders of magnitude smaller than that of $SrIrO_3$/SRO interface [68], confirming the expectation of weak DMI in our SRO films. Furthermore, the D of uncapped SRO film (6 u.c.) is about twice bigger than the

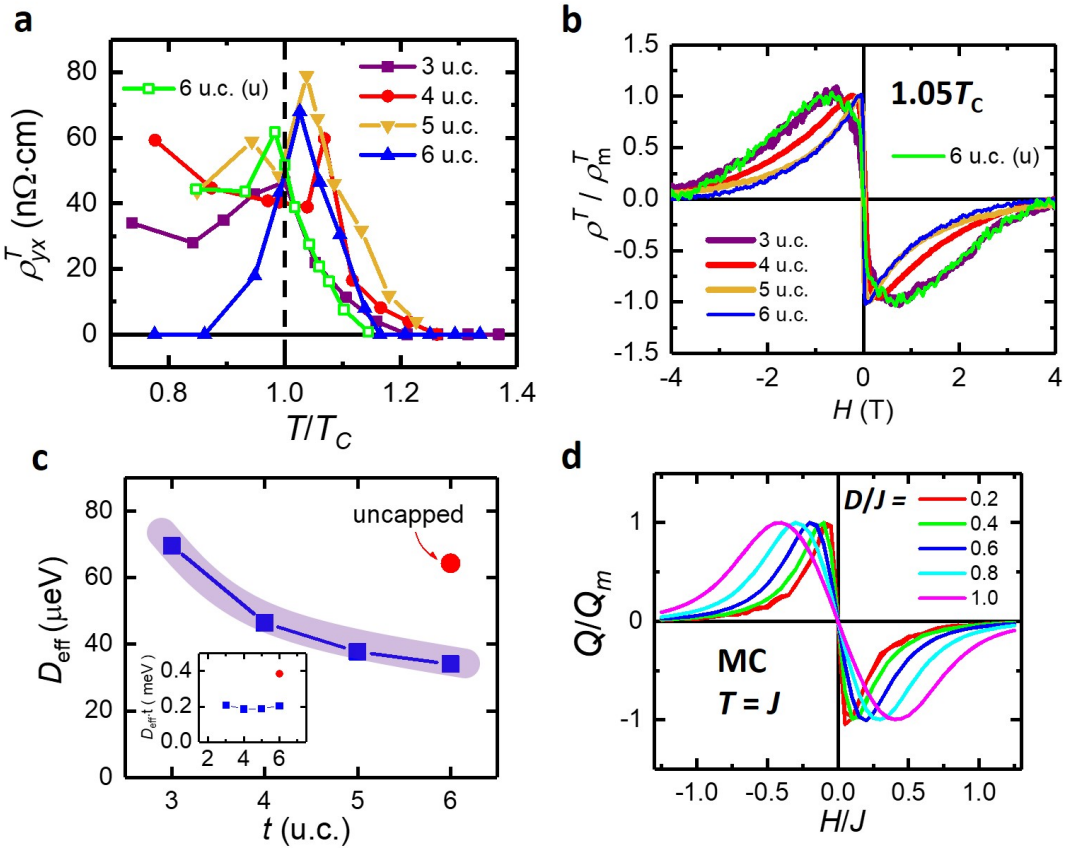

Figure 4.10: **Thickness dependence of the THE (ρ_{yx}^T).** **a**, Maximum values of ρ_{yx}^T as a function of temperature T of SRO films with thickness $t = 3 \sim 6$ u.c. capped (6 u.c. uncapped) with STO. **b**, antisymmetric H dependence of ρ_{yx}^T at the reduced temperature $1.05\,T_{\rm C}$. **c**, Effective DMI ($D_{\rm eff}$) extract from fitting the H dependence of ρ_{yx}^T shown in **b**. **d**, antisymmetric profiles of normalized TC Q/Q_m for various D at $T = J$. The D dependence is in good agreement with experimental results in **b**.

capped one, consistent with stronger asymmetry between SRO/STO interface and SRO surface. Last but not the least, the $D_{\rm eff}$ dependence is also reproduced by MC simulations, as shown in Fig. 4.10**d**. The excellent agreement between experiment and MC simulations demonstrate the chiral fluctuation mechanism of the THE in ultrathin SRO films.

At temperatures well below $T_{\rm C}$, $\rho_{yx}^{\rm A}(H)$ shows square-like magnetic hysteresis due to strong uniaxial anisotropy[119]. Interestingly, the THE peak persists to lower temperature following coercive fields in ultrathin limit (3 u.c.). The presence of the AHE hysteresis loop makes it difficult to separate the THE contribution. One needs to characterize the magnetization hysteresis with an independent magnetometer[68]. It is unclear whether

the low temperature THE originates from static topological spin texture (*e.g.*, skrymions), which will inspire future investigation. Nevertheless, the discovery of the THE around T_C in ultra-thin SRO films provides direct evidence of chiral fluctuation induced topological charges, suggesting that the THE is a general phenomenon in ferromagnetic metal thin films with chiral interaction as they approach the 2D limit. Our results open up possibilities of exploring topological transport in itinerant 2D ferromagnets and beyond[153–155], and may help to identify chiral spin liquid states [151, 156]

4.1.1 Complete Hall data of STO capped SRO thin films ($3 \sim 5$ u.c.) at various temperatures

3 u.c.

The Hall loops (OHE subtracted) at various temperature from 6 K to 115 K are shown in Fig. 4.11(a). The THE humps have been observed from 6 K to 110 K, above the $T_C \approx 95$ K. The insets show the THE peaks around zero field at 105 K and 110 K. However, such peaks disappear around 115 K. The paramagnetic behavior above 115 K was fitted by the Langevin function. The fitting parameter $h = k_B(T - T_C)/\mu$ was obtained at various temperatures from 115 K to 130 K. Temperature (T) as a function of h was plotted in Fig. 4.11 (b). The fitting results follow a linear relation. The intercept of the linear fitting gives $T_C^{fit} \approx 95$ K, in excellent agreement with the T_C determined by the dR_{xx}/dT anomaly. The topological Hall signals can be obtained by subtracting out the paramagnetic background, as shown Fig. 4.11(c). The field dependent topological Hall signals show the antisymmetric profiles from 80 K to 110 K, indicating the chiral fluctuation induced topological charges. The THE maximizes at T_C and disappears above 110 K. The intensity map of the THE as a function of T/T_C and H was plotted in Fig. 4.11(d), qualitatively consistent with MC simulations.

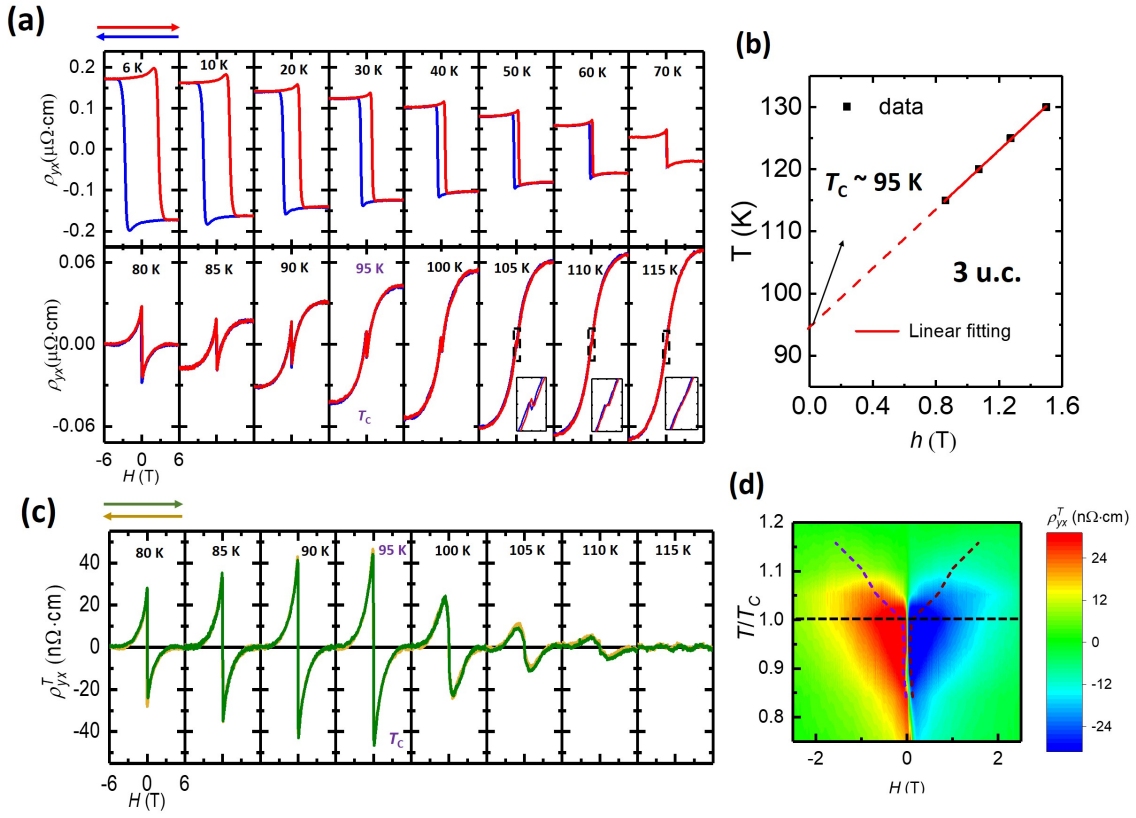

Figure 4.11: **Hall data of 3 u.c. capped SRO film at various temperature.** (a) Hall loops without the ordinary Hall effect (OHE). The insets show the zoomed-in curves around zero field, as indicated by the dashed rectangles. Red (blue) curves indicate field swept from -6 T to 6 T (6 T to -6 T).(b) Temperature as a function of Langevin fitting parameter h.(c) Topological Hall effect after paramagnetic background subtracted out. Green (yellow) curves indicate field swept from -6 T to 6 T (6 T to -6 T). (d) Intensity map of the THE as a function of T/T_C and H. The dashed lines trace the maximum THE values of each field scan.

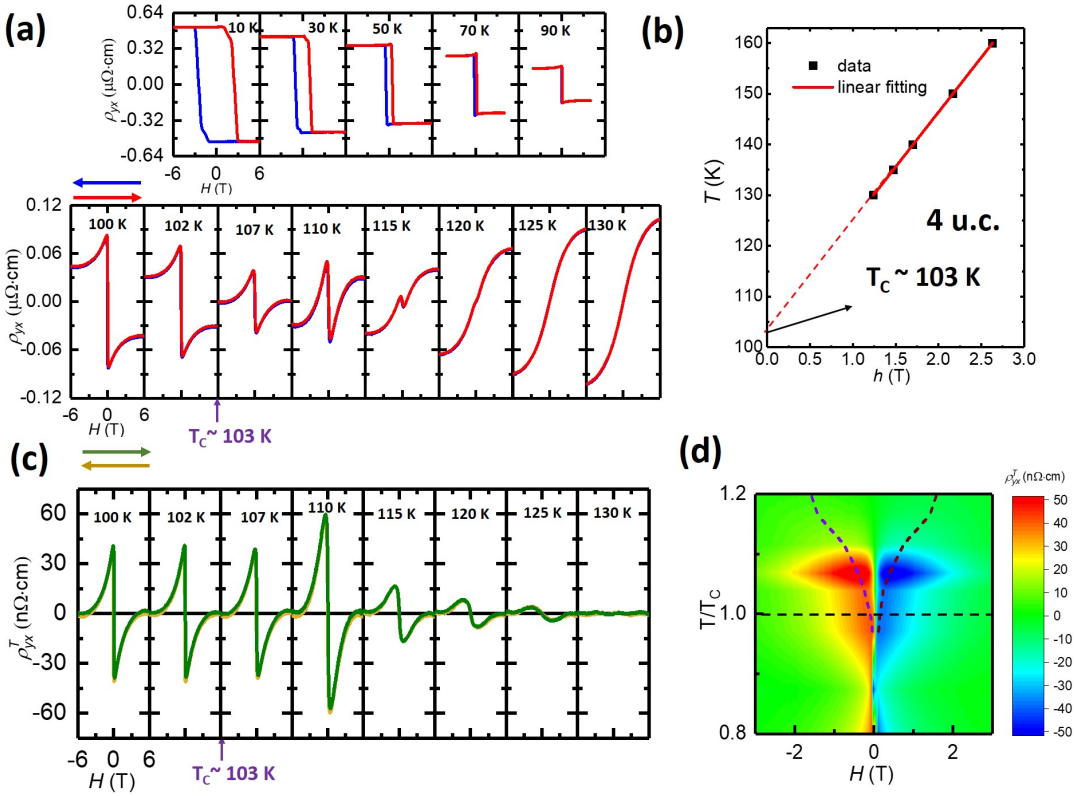

Figure 4.12: **Hall data of 4 u.c. capped SRO film at various temperature.** (a) Hall loops without the ordinary Hall effect (OHE). Red (blue) curves indicate field swept from $-6\,\mathrm{T}$ to $6\,\mathrm{T}$ ($6\,\mathrm{T}$ to $-6\,\mathrm{T}$).(b) Temperature as a function of Langevin fitting parameter h.(c) Topological Hall effect after paramagnetic background subtracted out. Green (yellow) curves indicate field swept from $-6\,\mathrm{T}$ to $6\,\mathrm{T}$ ($6\,\mathrm{T}$ to $-6\,\mathrm{T}$). (d) Intensity map of the THE as a function of T/T_C and H. The dashed lines trace the maximum THE values of each field scan.

4 u.c.

The Hall data (OHE subtracted) of 4 u.c. capped SRO film from 10 K to 130 K was shown in Fig. 4.12 (a). Around $T_C \approx 103$ K, the antisymmetric peak around zero magnetic field, which is a strong evidence of chiral fluctuation induced THE, persists all the way to 120 K, 17 K above the T_C. The Hall data (OHE subtracted) is absent of the THE peaks above the 125 K, where it can be nicely fitted by Langevin function $L(x)$. The fitting parameter $h = k_B(T - T_C)/\mu$ was obtained at various temperatures from 130 K to 160 K. Temperature (T) as a function of h was plotted in Fig. 4.12 (b). The fitting results follow a linear relation. The intercept of the linear fitting gives $T_C^{fit} \approx 103$ K, in excellent agreement with the T_C determined by the dR_{xx}/dT anomaly. This agreement allows us to extrapolate the h's value for removing the paramagnetic AHE contribution at $T < 130$ K. The extracted THE data are shown in Fig. 4.12 (c). The antisymmetric THE peaks are observed in a wide temperature range from 100 K to 125 K and maximize at 110 K, 7 K above T_C. The intensity map of ρ_{yx}^T is shown in Fig. 4.12 (d). The THE extends well into the paramagnetic phase above T_C, in consistent with the origin of thermal fluctuation.

5 u.c.

The Hall data (OHE subtracted) of 5 u.c. capped SRO film from 10 K to 135 K was shown in Fig. 4.13 (a). Around $T_C \approx 106$ K, the antisymmetric peak around zero magnetic field, which is a strong evidence of chiral fluctuation induced THE, persists all the way to 130 K, 24 K above the T_C. The Hall data (OHE subtracted) is absent of the THE peaks above the 125 K, where it can be nicely fitted by Langevin function $L(x)$. The fitting parameter $h = k_B(T - T_C)/\mu$ was obtained at various temperatures from 135 K to 160 K. Temperature (T) as a function of h was plotted in Fig. 4.13 (b). The fitting results follow a linear relation. The intercept of the linear fitting gives $T_C^{fit} \approx 106$ K, in excellent agreement with the T_C determined by the dR_{xx}/dT anomaly. This agreement allows us to extrapolate the h's value for removing the paramagnetic AHE contribution at $T < 135$ K. The extracted

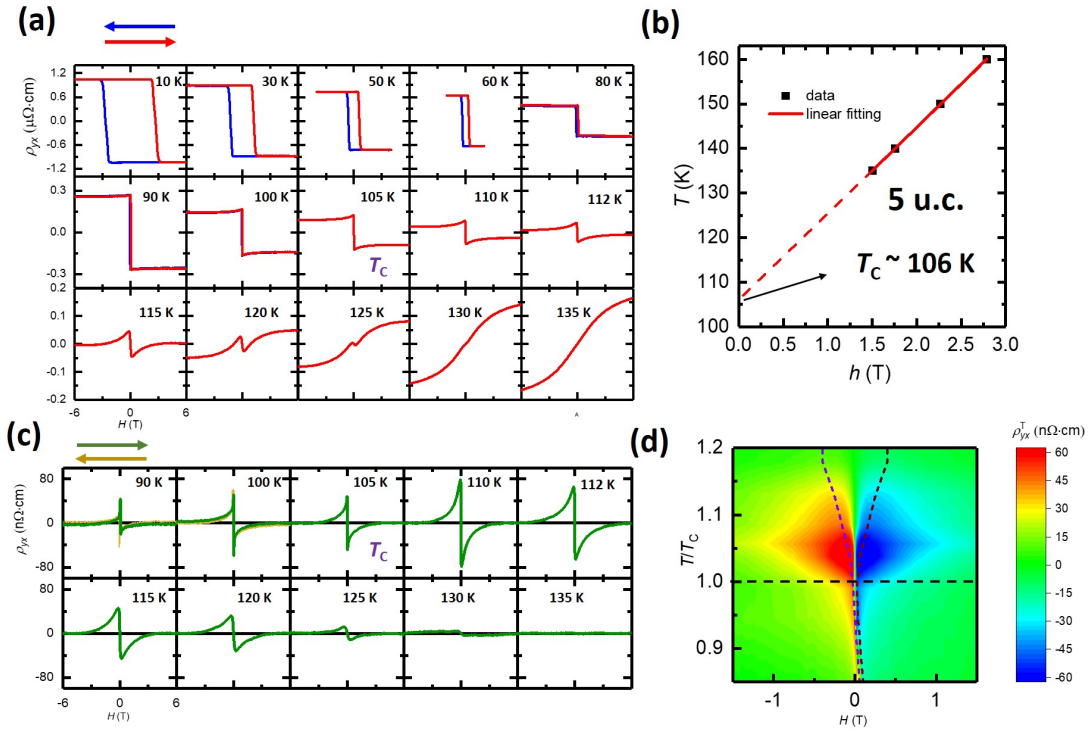

Figure 4.13: **Hall data of 5 u.c. capped SRO film at various temperature.** (a) Hall loops without the ordinary Hall effect (OHE). Red (blue) curves indicate field swept from −6 T to 6 T (6 T to −6 T).(b) Temperature as a function of Langevin fitting parameter h.(c) Topological Hall effect after paramagnetic background subtracted out. Green (yellow) curves indicate field swept from −6 T to 6 T (6 T to −6 T). (d) Intensity map of the THE as a function of T/T_C and H. The dashed lines trace the maximum THE values of each field scan.

THE data are shown in Fig. 4.13 (c). The antisymmetric THE peaks are observed in a wide temperature range from 90 K to 130 K and maximize at 110 K, 4 K above T_C. The intensity map of ρ_{yx}^T is shown in Fig. 4.13 (d). The THE extends well into the paramagnetic phase above T_C, in consistent with the origin of thermal fluctuation.

4.1.2 Hall data of uncapped SRO film (6 u.c.) at various temperature

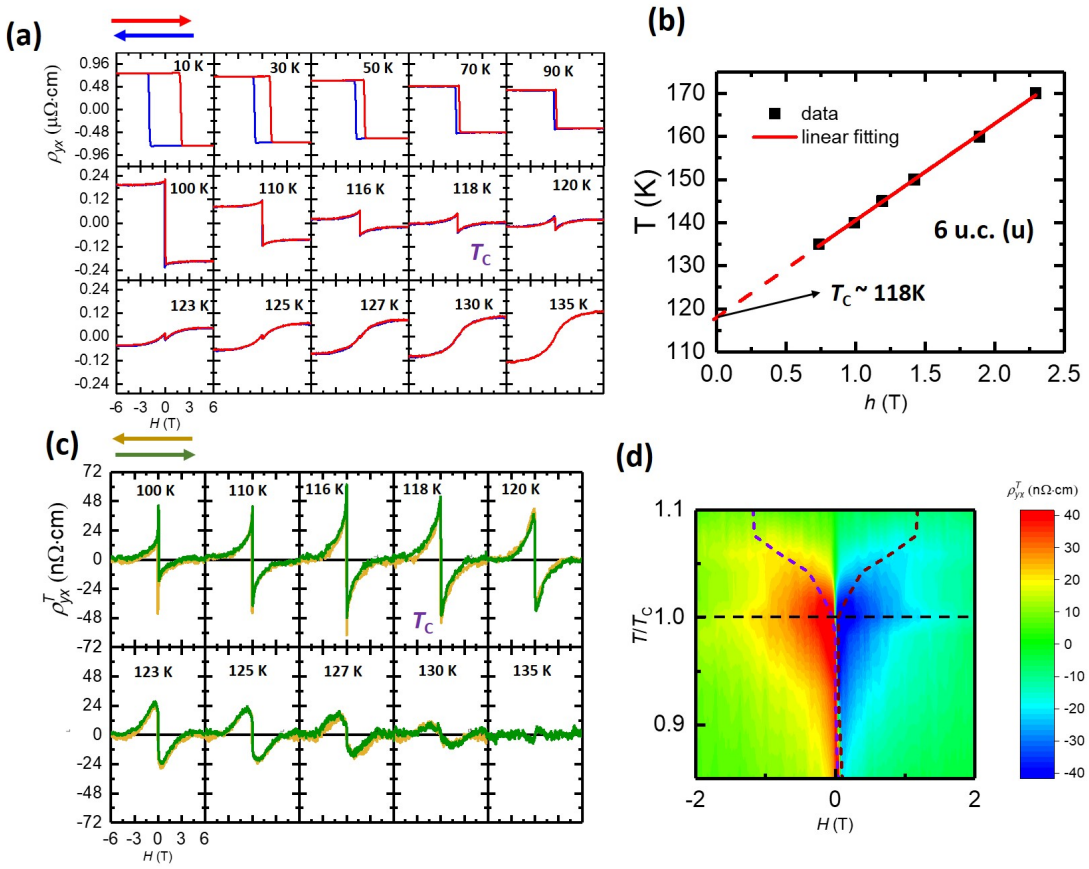

Figure 4.14: **Hall data of 6 u.c. uncapped SRO film at various temperature** (a) Hall loops without the ordinary Hall effect (OHE). Red (blue) curves indicate field swept from −6 T to 6 T (6 T to −6 T).(b) Temperature as a function of Langevin fitting parameter h.(c) Topological Hall effect after paramagnetic background subtracted out. Green (yellow) curves indicate field swept from −6 T to 6 T (6 T to −6 T). (d) Intensity map of the THE as a function of T/T_C and H. The dashed lines trace the maximum THE values of each field scan.

The chiral fluctuation induced THE has been also observed in uncapped SRO ultrathin films grown on STO substrate. The uncapped SRO films show weaker ferromagnetism,

compared to capped ones. The critical thickness increases to t=4. Moreover, the 4 u.c. and 5 u.c. films show narrow Hall hysteresis loops at low termperature and low Curie temperature, indicating a disordered ferromagnetism. The 6 u.c. film, however, shows a robust ferromagnetism at low temperature, as shown in Fig. 4.14(a). The THE humps have been observed around $T_C \approx 118\,K$. The high temperature Hall loops ($135\,K \leq T \leq 170\,K$) was fitted by Langevin function and the fitting parameter $h = k_B(T - T_C)/\mu$ was obtained. By plotting T as a function of h, the Curie temperature is around 118 K, which is quantitatively consistent with the resistance anomaly, determined by the derivative peak. By subtracting the paramagnetic background, estimated by using the fitting parameter h's at various temperature, the antisymmetric topological Hall signals were shown in Fig. 4.14(c). The heart shape intensity map, shown in Fig. 4.14(d), suggests the maximized THE around T_C, qualitatively consistent with the MC simulations and STO capped SRO ultrathin films.

4.2 Disorder driven topological Hall effect

The previous section discussed chiral fluctuation driven THE (fTHE) in both capped and uncapped SRO films around T_C. In this section, we will focus on the low-temperature THE in these SRO films. As shown in Fig. 4.5, the Hall data of 6 u.c. capped SRO film exhibit a square-like hysteresis loop at low temperature without an obvious signature of the THE. For the 3 u.c. capped SRO, however, such THE feature can persist to low temperature. As shown in Fig. 4.11(a), a significant hump emerges around the H_C at low temperature. Such low-temperature THE humps have been observed in various ultra-thin film systems, including $Cr_x(Bi_{1-y}Sb_y)_{2-x}Te_3/(Bi_{1-y}Sb_y)_2Te_3$ heterostructures[65], Mn-doped Bi_2Te_3[66], SrIrO3/SRO bilayer structures[68], and CrTe[67]. The formation of a static skyrmion phase has been claimed in these systems. The direct evidence of this exotic skyrmion phase, however, is still lacking. In our relatively symmetric capped SRO films, the DMI should be much smaller, *i.e.* $D << D_c \equiv 2\sqrt{2JK}/\pi$. The ground state is ferromagnetic. The possibility of emergence of static skyrmions in a ferromagnet is a very interesting topic. To

address these issues, we used magnetic force microscopy to investigate the local magnetic structures in these ultra-thin SRO systems at low temperature.

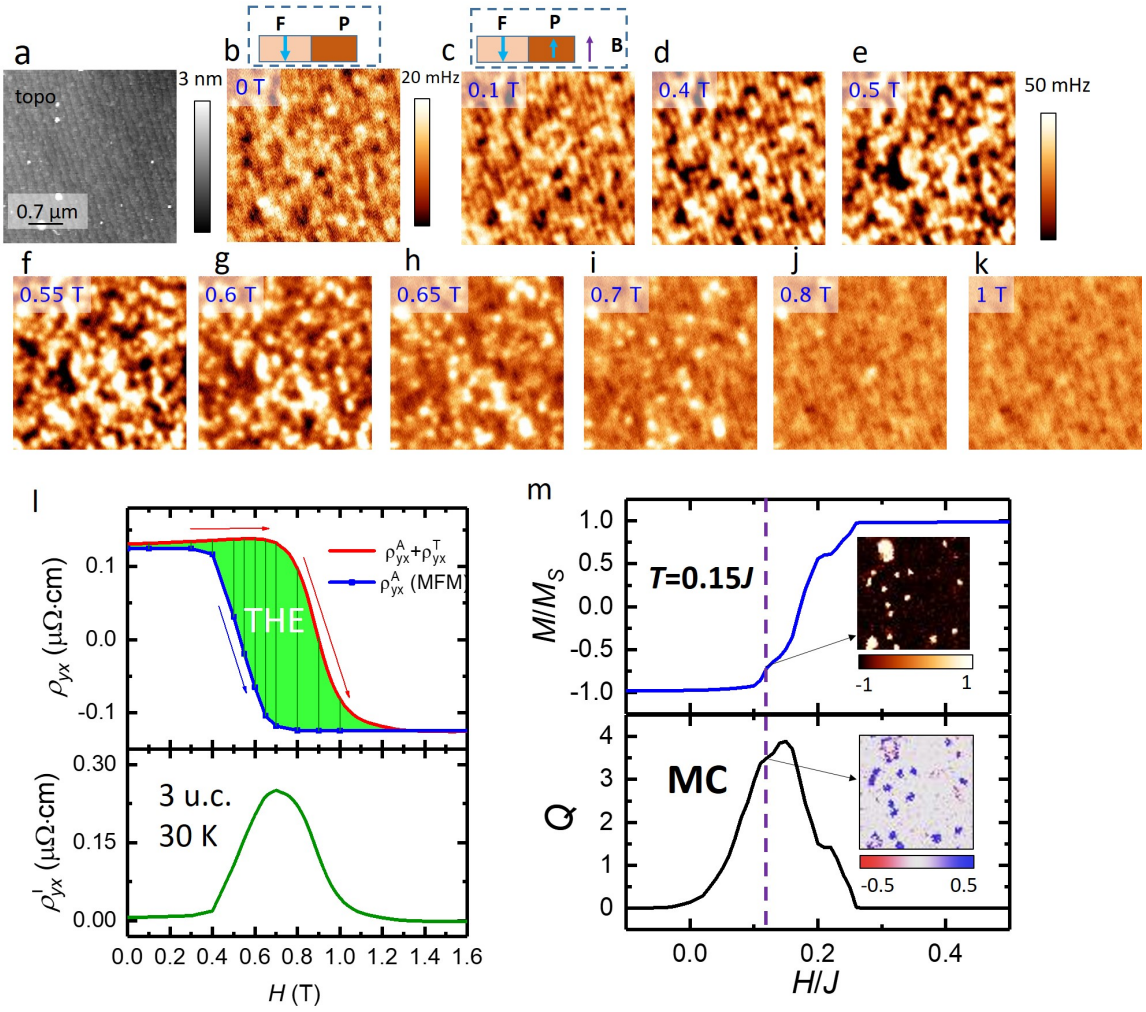

Figure 4.15: | **Topograhic and MFM images with in-situ Hall data at 30 K for $(SRO)_3/(STO)_2$ bilayer.** **a**, Topograhic image of the Au coated surface. **b-k**, MFM images at various fields from 0 T to 1 T. They show a coexistence of ferromagnetic (F) and paramagnetic (P) phases. **l**, The field-dependent $\rho^A_{yx} + \rho^T_{yx}$ (blue) and ρ^A_{yx} (red),deduced from MFM images. The difference (green) gives ρ^T_{yx}.**m**, MC simulations of magnetization M and topological charges Q at $T = 0.15J$.

Figure 4.15 shows the topographic and MFM images taken at 30 K on the $(SRO)_3/(STO)_2$ bilayer. The topographic image of the Au coated surface exhibits clear stripe-like atomic step edges, following the miscut of $SrTiO_3$ (001) substrate. This indicates a high quality of the film depositions. The film was firstly saturated at -1 T and later the field was ramped

down to 0 T. The Hall resistance, at zero field, suggests the film stays in the saturation state. The MFM image, however, shows some spatial variations, indicating the magnetic inhomogeneity, possibly due to a mixture of ferromagnetic and paramagnetic phases. As a small positive magnetic field was applied, *e.g.*, at 0.1 T, the MFM pattern stayed the same while the MFM contrast gets stronger. This indicates that the ferromagnetic regions (bright) are robust against small positive field, while the paramagnetic regions (dark) are polarized by the external magnetic field. At higher positive fields, the ferromagnetic phase was finally reversed. The magnetization reversal process shows typical ferromagnetic domain behaviors, without any indication of Skyrmion lattices. The M-H loop, *i.e.*, ρ_{yx}^{A}-H loop can be estimated by counting the up and down domain population of the ferromagnetic phase. . There is a large discrepancy between the ρ_{yx}^{A}-H (MFM) and the anomalous Hall loop (AHE data with the OHE subtracted), indicating the emergence of a large THE, which reaches $\sim 0.25\mu\Omega\cdot$cm, at 0.7 T. Although some magnetic bubbles were found in MFM images at this field. But, these bubbles are merely the pinned ferromagnetic domains, other than single magnetic skyrmions, because the density of these bubbles can give rise to a topological Hall signal $\sim$0.25 n$\Omega\cdot$cm, much smaller than the experimental value. In average, each magnetic bubble carries 1000 topological charges.

To understand how the magnetic inhomogeneity affects the THE in a uniaxial ferromagnet, we add some magnetic disorders (local reduction of K and J) in the MC simulations. These Monte Carlo simulations were again conducted on a $N^2 = 32 \times 32$ square lattice with periodic boundary conditions. The exchange and anisotropy constants were replaced with tensors which could change depending on the particular bond/site corresponding to their indices. To generate the paramagnetic defects underlying the tensorial structure of J_{ij} and K_i, we used the following procedure: first, a random site in the lattice was selected to be a defect; then, sites neighboring this nucleation site were also chosen to be defective with 80% probability; then a new nucleation site was chosen, and the process is repeated until exactly 1/16 of the lattice contained paramagnetic defects. The paramagnetic defects have

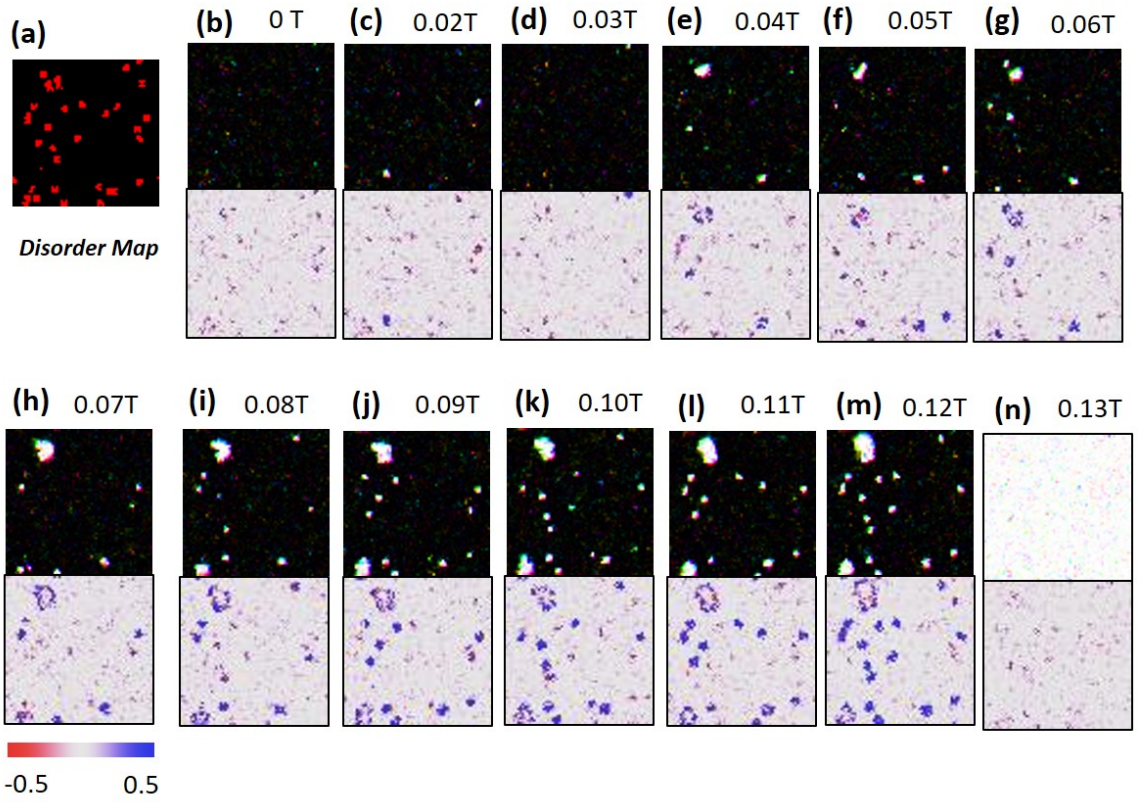

Figure 4.16: | **MC simulations of magnetization and TC maps at 0.15** J **a**, magnetic disorder map used for MC simulations. **b-n**, Field-dependent magnetization (upper) and TC (lower) maps from 0 T to 0.13 T.

their on-site anisotropy and the exchange interaction of all their bonds reduced by 50% and 75%, respectively, compared to the majority non-defective sites. Figure 4.16(a) shows a typical map of these paramagnetic defects (red regions).

By using these MC simulations with paramagnetic defects, the single peak Q as a function of H can be achieved around H_C at low temperature $T \sim 0.15J$, in sharp contrast to the disorder-free MC simulations, where the THE is largely suppressed at low temperature. The snapshots of the distributions of magnetization (M) and Q are plotted in Figure 4.16(b)-(n). During magnetization reversal process, the reversed domain was firstly nucleated in the paramagnetic defects as expected. Interestingly, the Q maps show the topological charges tend to accumulate on the boundary of the pinned ferromagnetic domains, where the spins are rotating from up to down in a specific chirality, determined by the direction of $\mathbf{D}$. Limited by the sensitivity and lateral resolution of MFM, we cannot directly probe the topological charges on the magnetic domain boundaries. Further investigation of disorder-driven THE (dTHE) requires more delicate magnetic probes.

Chapter 5

Epilogue

This thesis presents a systematic study of two fascinating topological phenomena in magnetic thin film systems: quantum anomalous Hall effect and topological Hall effect. One concerns the Berry phase in momentum space and the other one concerns the Berry phase in real space. Both effects are very appealing to physicists due to the fundamental interests and potential applications. In this section, we will make a brief summary of the main contents of this thesis and discuss the future research directions, based on the current progress of these fields.

5.1 Summary of results

In the prologue, we introduced some basic concepts relevant to the quantum anomalous Hall effect and topological Hall effect. We first discussed the Berry connection and Berry curvature in k space, which are the counterparts of the vector potential and magnetic field in real space. The intrinsic anomalous Hall effect, therefore, originates from the Berry phase in k space. The quantum anomalous Hall effect is possible to be realized if topological nontrivial band structure which carries the quantized Berry phase. Later, a brief history of the experimental realizations of three quantum Hall effects has been discussed, along with the discovery of 2D and 3D topological insulators. As for the real space Berry phase effect, we talked about the topological Hall effect, which is related to the non-coplanar spin textures in real space. The integer Berry phase gives rise to the topological object, which is known as skyrmion. We discussed how people used the THE to determine the emergence of a skyrmion phase in B20 compounds.

For the method chapter, we introduced the basic principle of cryogenic magnetic force microscopy, which is a very powerful technique to characterize magnetic domains, especailly for thin films. We also present how we combined both MFM and in-situ transport together to accurately determine the $M-H$ loops of an Ising ferromagnet. To convincingly illustrate this point, we present the MFM and in-situ transport data of two magnetic film systems with weak magnetic signals: 200 nm h-$LuFe_3$ film and 7 u.c. SRO film. These results demonstrate that our homemade MFM setup is capable of characterizing $M-H$ loops with very high sensitivity, which has been verified by SQUID data and in-situ transport data, respectively. The results of h-$LuFe_3$ film has been published in Ref.[116].

We then discussed the pioneer works of characterizations of ferromagnetic domain structures in magnetic TIs, including Cr-doped $(Bi,Sb)_2Te_3$ and V-doped Sb_2Te_3 films. The characterizations of the size and shape of ferromagnetic domains in these systems is of great importance to facilitate the discovery of chiral edge states on the domain boundaries. The MFM studies of Cr-doped $(Bi,Sb)_2Te_3$ films have been published in Ref.[120]. And the MFM studies of V-doped Sb_2Te_3 films have been published in Ref.[122]. Finally, we successfully visualized the ferromagnetism in a quantum anomalous Hall system: Cr and V co-doped BST films. Our discovery resolves one of the major challenges in QAH systems, and paves the way towards high-temperature dissipationless conduction by exploring magnetic TIs. These important results have been published in Ref.[128].

The axion insulating state can be realized in a sandwich heterostructure by combining two QAH layers with different magnetic coercivity. In the intermediate state, when one layer is flipped by the external magnetic field, while the other one is not, the QAH heterostructure has the antiparallel magnetization alignment, which is a necessary condition to realize the axion insulating state. Our MFM results indicate a two-step transition during magnetization reversal process of a QAH heterostructure, which is a very promising candidate for an axion insulator. The MFM studies of this axion insulator has been published in Ref.[15].

For the real-space phenomenon, we discussed the THE in ultra-thin film systems: the

STO capped and uncapped SRO films. We present a surprising and beautiful discovery of the THE above T_C in the paramagnetic phase of SRO films. The field, temperature and film thickness dependence of the THE has excellent agreement with MC simulations, which indicates a chiral fluctuation driven THE in 2D uniaxial ferromagnets. Our findings encourage further explorations of THE in other 2D ferromagnets. In the last section, we discussed the disorder-driven THE in SRO films at low temperature. The MFM data exhibits the coexistence of paramagnetic and ferromagnetic phases in the 3 u.c. capped SRO film. The field and temperature dependence of low temperature THE is qualitatively consistent with MC simulation with paramagnetic defects.

5.2 Perspectives for future research

Quantum anomalous Hall effect

One of the major obstacles in the field of quantum anomalous Hall effect is the ultra-low temperature to achieve the quantum anomalous Hall effect ($T < 1\,\mathrm{K}$). Up to now, the QAHE has been only observed in magnetic TI thin film systems. Within these systems, there are two main factors that limit the QAH temperature. One is the magnetic inhomogeneity, which can be improved by magnetic co-doping[128]. The other one concerns the complicate band structure of the $(Bi,Sb)_2Te_3$, whose valence band maximum is above the Dirac point. Thus, it requires ultra-low temperature to localize these bulk states (valence band) to achieve the QAHE, when the Fermi level is tuned to the Dirac point. Herein, it is imperative to find a TI which has a 'better' band structure, where the Dirac point is well inside the bulk band gap. ARPES data exhibits Dirac point is more away from VBM in Bi_2Se_3 than in Bi_2Te_3 and Sb_2Te_3[29]. However, both surface and bulk states of Bi_2Se_3 tend to have n-type charge carriers, due to the native n-type defects such as selenium vacancies[157, 158]. It has been very challenging to hole dope the Bi_2Se_3. Recently, J. Moon *et al.* has successful achieved p-type Bi_2Se_3 by doping Ca elements and employing In_2Se_3 buffer layer[159]. The problem is the degradation of film quality with Ca doping. The situation becomes more complicated if magnetic elements are doped to introduce ferromagnetism. Hopefully, these issues could be resolved by material scientists in the future.

Another possible direction to achieve QAHE is to fabricate FMI/TI/FMI heterostructures. The exchange coupling between a TI and a FMI breaks the TRS on the interface and leads to the QAHE. Experimentally, it is challenging to find the suitable materials for the FMI layer, which can form a high-quality heterostructure with TIs and lead to a strong exchange coupling. Extensive studies have been done on EuS, a ferromagnetic insulator with in-plane magnetic anisotropy. Although recent neutron measurements have shown out-of-plane magnetism induced on the interface of Bi_2Se_3/EuS, the induced

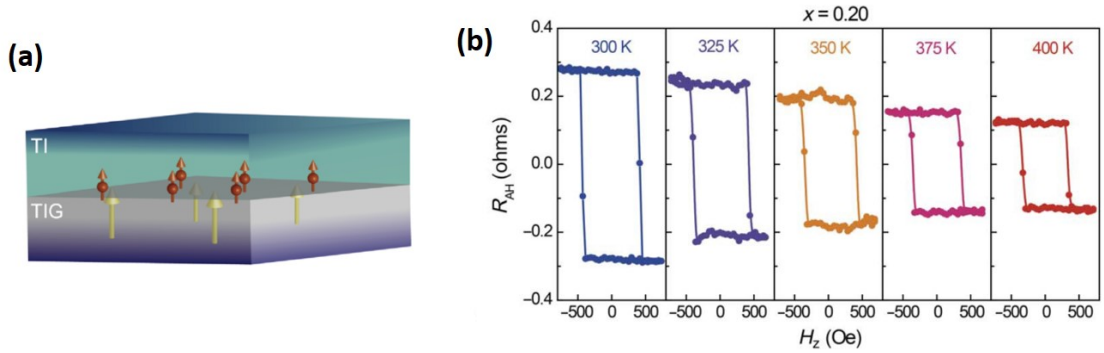

Figure 5.1: (a)Schemtics of the proximity coupling between TI and TIG. (b)AHE loops of TIG/$(Bi_xSb_{1-x})_2Te_3$ for $x = 0.20$ (p-type) between 300 and 400 K.

magnetism is too weak to result in significant AHE[160]. Most recently, C. Tang *et al.* used a high-T_C ($\sim$ 560 K) ferrimagnetic insulator, $Tm_3Fe_5O_{12}$ (TIG), with a perpendicular magnetic anisotropy. The perpendicular magnetic phase has been achieved in TIs well above 400 K, which is one order of magnitude higher than the T_Cs of the magnetic TIs which exhibits QAHE[161]. Figure 5.1(b) shows square-like AHE loops persist to 400 K in TIG/$(Bi_xSb_{1-x})_2Te_3$ ($x = 0.2$), indicating a robust ferromagnetism on the interface of TI/TIG even above room-temperature. However, the anomalous Hall resistance is still far away from the quantized value (h/e^2). One of the major issues in this TI/TIG system is how to grow another FMI layer on top of TI, in order to gap out the top surface. Since TIG has much higher growth temperature than TI, it is impossible to use TIG as the top layer. Recently, several 2D ferromagnetic insulators have been discovered, which can be used as the candidates for the top FMI layer. These exciting results encourage the further exploration of QAHE in the FMI/TI/FMI systems. In addition to FMI, the ferromagnetic surfaces of antiferromagnetic insulators (AFMI) may be also used to gap TI surface states. Since there are more AFMI than FMI in nature, AFMI/TI/AFMI heterostructures may be a more promising direction to explore. Theoretically, antiferromagnetic MnSe and MnTe have been proposed to be good candidates to open up a significant mass gap at the surface states[162].

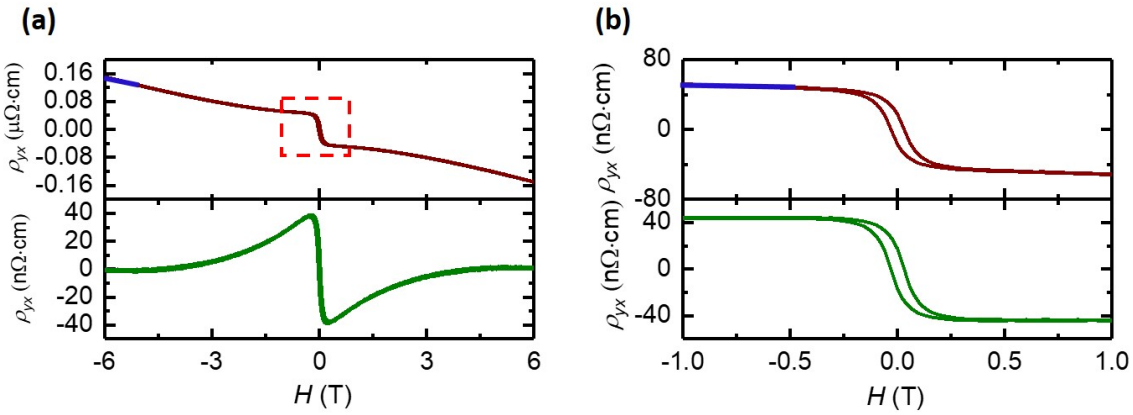

Figure 5.2: (a)Raw Hall data of 4 u.c. capped SRO film measured at 107 K (upped panel). Field was swept from -6 T to 6 T. Hall data after OHE (slope of blue line in upper panel) subtracted was shown in lower panel. (b) Raw Hall data of 4 u.c. capped SRO film with field swept from -1 T to 1 T (red square in (a)). Hall data after OHE (slope of blue line in upper panel) subtracted was shown in lower panel.

Chiral fluctuation driven topological Hall effect

As illustrate in Chapter 4, chiral fluctuation driven THE is a universal phenomenon in 2D uniaxial ferromagnets. It is natural to raise the question why this phenomenon has seldom been reported. Based on my experience of studying the THE in SRO systems, this is closely related to the magnetic fields we sweep during the Hall loop measurements. As the temperature approaches the T_C, the hysteresis loop is getting smaller and smaller and finally disappears. If the researchers only focus on the anomalous Hall loops of these magnetic films, they would not bother to apply a large enough magnetic field or apply very fine steps. However, the THE peaks could be very wide or very narrow, depending on the DMI strength of the thin films. Therefore, a very delicate measurement is required to find the chiral fluctuation driven THE around T_C.

To illustrate this point, the Hall loops of 4 u.c. capped SRO film at 107 K are shown in Figure 5.2(a). The fields were swept from -6 T to 6 T. A non-linear Hall effect emerges at high fields. If the ordinary Hall effect, estimated by the slope between -5 T and -6 T, is subtracted from raw Hall data (brown curve), the anomalous Hall loop (green curve) shows signatures of the THE. However, if the field sweeps from -1 T to 1 T, as shown in

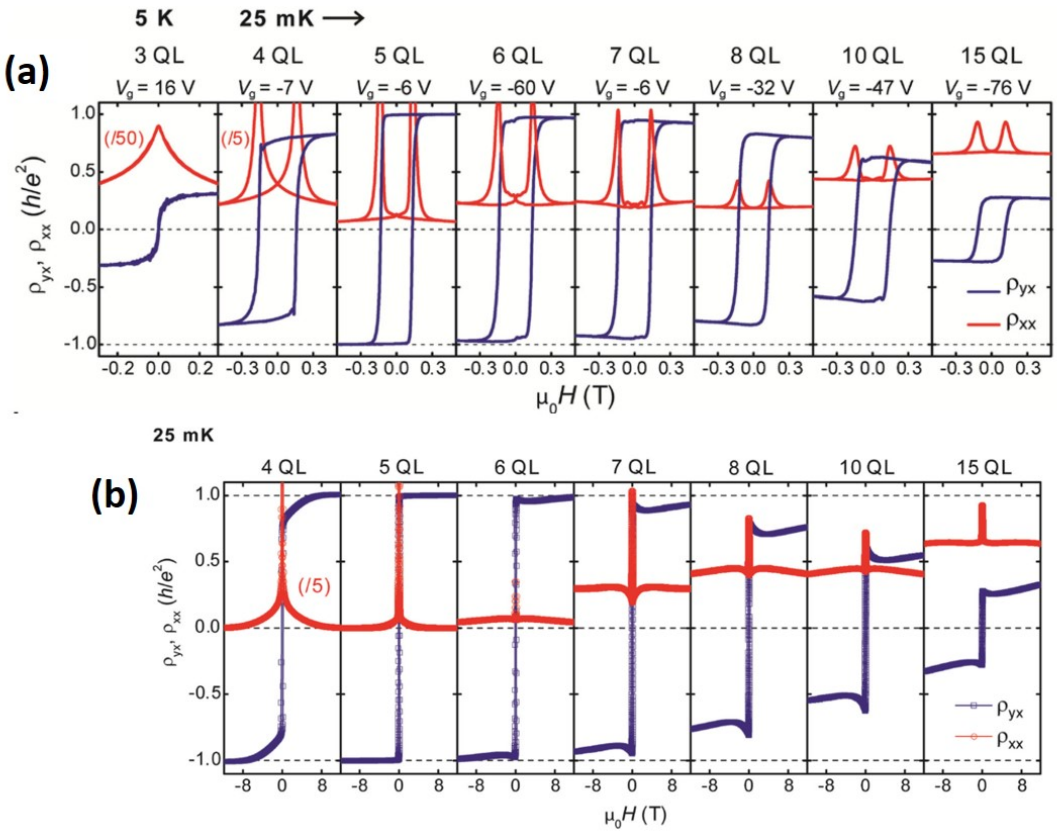

Figure 5.3: Field-dependent ρ_{yx} and ρ_{xx} of $Cr_{0.15}(Bi_{0.1}Sb_{0.9})Te_3$ films of different thicknesses. (a) Field was swept from -0.5 T to 0.5 T. (b) Field was swept from -12 T to 12 T. Adapted from Ref.[16].

Figure 5.2(b), the non-linear Hall effect is invisible in raw Hall data. The anomalous Hall loop with linear background subtracted (slope between -1 T and -0.5 T) shows no signatures of the THE.

By searching the literature regarding Hall measurements of ultrathin magnetic films, we found some indications of the fTHE in the magnetic TI films. For Cr-doped BST films with various thickness (4∼15 QL), the low-field Hall loops (-0.5 T to 0.5 T) exhibits typical square-like hysteresis loops[16]. However, the large magnetic field measurements, as shown in Figure 5.3(b), exhibits obvious non-linear effect at high field for 4 ∼ 15 QL films, which possibly originates from the fTHE. This fTHE exists at low temperature well below T_C, possibly due to the superparamagnetism in Cr-doped BST films.

The large effective DMI in the 2D ferromagnetic film leads to wide THE peaks, which

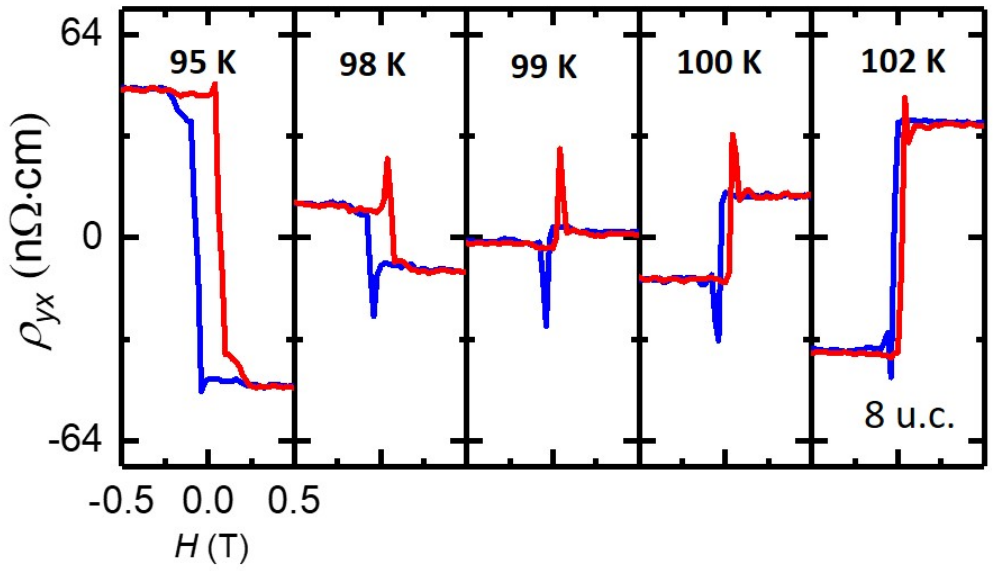

Figure 5.4: Field-dependent Hall resistance (ρ_{yx}) (OHE subtracted) measured at various temperature from 95 K to 102 K of STO capped 8 u.c. SRO film.

require high magnetic fields to probe. On the other hand, small DMI may lead to very sharp THE peaks, which require small magnetic field steps to probe. For instance, the effective DMI in 8 u.c. SRO films is largely suppressed. As shown in Figure 5.4, very shape THE peaks with a width of ~ 0.05 T are visible between 95 K and 102 K, possibly originating from magnetic disorders. It requires very fine magnetic field steps to capture these dTHE peaks. At higher temperatures, the THE peaks are invisible, possibly because the enhanced AHE overwhelms the THE. Above T_C, the anomalous Hall loops can be fitted by Langevin function $L(H)$, as shown in Fig. 5.5(a). Fig. 5.5(b) shows the temperature Ts as a function of fitting parameter hs. The linear relation gives the $T_C \sim 121$ K. The residual Hall resistivity $\Delta\rho_{yx} = \rho_{yx}^A - L(H)$, as shown in Fig. 5.5(c), is largely suppressed at elevated temperatures, indicating the anomalous Hall loops can be better fitter by Langevin function at elevated temperatures. This is qualitatively consistent with the temperature dependence of the fTHE. Thus, the fTHE is very likely to still exist in the capped 8 u.c. SRO film. However, it is difficult to accurately extract the fTHE from the Hall data in this case, because the Hall data is dominated by the AHE.

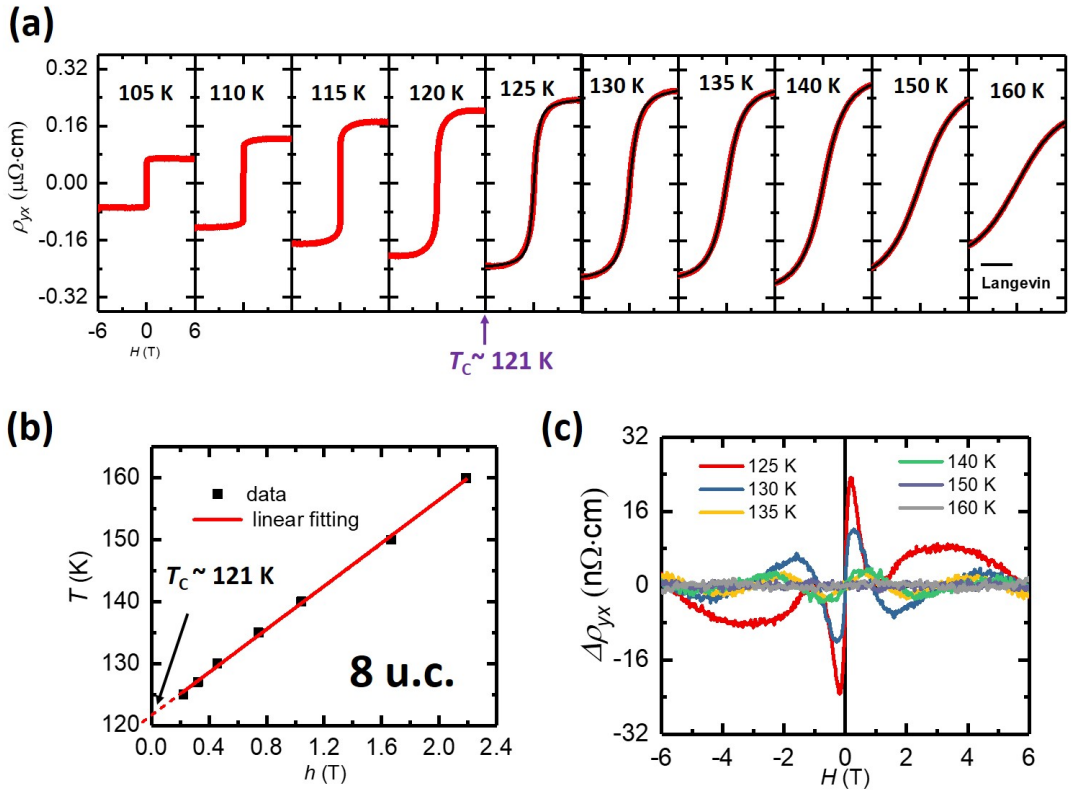

Figure 5.5: (a) Field-dependent Hall resistance (ρ_{yx}) (OHE subtracted) measured at various temperature from 105 K to 160 K of STO capped 8 u.c. SRO film. Black lines are Langevin fittings of ρ_{yx} above T_C. (b) Temperature as a function of Langevin fitting parameter h gives $T_C \sim 121$ K. (c) Residual Hall resistivity ($\Delta\rho_{yx}$) above T_C.

Due to the easily missed THE peaks, those well studied magnetic thin films are worth revisiting for more careful measurements. Recently, some 2D itinerant ferromagnets have been discovered, *i.e.*, Fe_3GeTe_2[154, 155] and VSe_2[153]. It is very likely that the fTHE exists in these systems. In addition to magnetic films with perpendicular anisotropy, this chiral fluctuation driven THE is theoretically allowed in magnetic films with in-plane anisotropy as well, although it has not been experimentally confirmed yet. It might be more interesting if this effect also exists in antiferromagnets. To address these issues, more theoretical and experimental works need to be done by condensed matter physicists.

Appendix A

List of abbreviations

2D	two-dimensional
2DEG	2D electron gas
AFM	atomic force microscopy
AFMI	antiferromagnetic insulator
AHE	anomalous Hall effect
ARPES	angle-resolved photoemission spectroscopy
BST	$(Bi,Sb)_2Te_3$
cAFM	conductive atomic force microscopy
CBM	conduction band minimum
DMI	Dzyaloshinskii-Moria interaction
DMS	diluted magnetic semiconductor
dTHE	disorder driven THE
EFM	electrostatic force microscopy
FMI	ferromagnetic insulator
FT	Fourier transformation
fTHE	chiral fluctuation driven THE
FWHM	full-width-half-maximum
IQHE	integer quantum Hall effect
IS	inversion symmetry
LL	Landau level
MBE	molecular beam epitaxy
MC	Monte Carlo
ME	magnetoelectric
MFM	magnetic force microscopy
MOKE	magneto-optical Kerr effect

MR	magnetoresistance
MRD	Materials Research Diffractometer
NV	nitrogen-vacancy
OHE	ordinary Hall effect
OOP	out-of-plane
PFM	piezoresponse force microscopy
PLD	pulsed laser deposition
QAHE	quantum anomalous Hall effect
QL	quintuple layer
QSHE	quantum spin Hall effect
RHEED	reflection high-energy electron diffraction
RKKY	Ruderman-Kittel-Kasuya-Yosida
RSM	reciprocal space mapping
SOC	spin-orbital coupling
SQUID	superconducting quantum interference device
SS	surface state
STM	scanning tunneling microscopy
STXM	scanning transmission X-ray microscopy
TC	topological charge
TEM	transmission electron microscopy
THE	topological Hall effect
TIG	$Tm_3Fe_5O_{12}$
TI	topological insulator
TME	topological magneto-electric effect
TRS	time reversal symmetry
u.c.	unit cell
VBM	valence band maximum
XRD	X-ray diffraction
YSZ	yttria-stabilized cubic zirconia
ZFC	zero-field cooling
ZHP	zero Hall plateau

Bibliography

[1] M. König, S. Wiedmann, C. Brüne, A. Roth, H. Buhmann, L. W. Molenkamp, X. Qi, and S. Zhang, "Quantum spin Hall insulator state in HgTe quantum wells markus," *Science*, vol. 318, pp. 766–771, 2007.

[2] C. Jozwiak, Y. L. Chen, A. V. Fedorov, J. G. Analytis, C. R. Rotundu, A. K. Schmid, J. D. Denlinger, Y. D. Chuang, D. H. Lee, I. R. Fisher, R. J. Birgeneau, Z. X. Shen, Z. Hussain, and A. Lanzara, "Widespread spin polarization effects in photoemission from topological insulators," *Phys. Rev. B*, vol. 84, no. 16, p. 165113, 2011.

[3] C.-Z. Chang, J. S. Zhang, X. Feng, J. Shen, Z. C. Zhang, M. H. Guo, K. Li, Y. B. Ou, P. Wei, L. L. Wang, Z. Q. Ji, Y. Feng, S. H. Ji, X. Chen, J. F. Jia, X. Dai, Z. Fang, S. C. Zhang, K. He, Y. Y. Wang, L. Lu, X. C. Ma, and Q. K. Xue, "Experimental observation of the quantum anomalous Hall effect in a magnetic topological insulator," *Science*, vol. 340, no. 6129, pp. 167–170, 2013.

[4] E. O. Lachman, A. F. Young, A. Richardella, J. Cuppens, H. R. Naren, Y. Anahory, A. Y. Meltzer, A. Kandala, S. Kempinger, Y. Myasoedov, M. E. Huber, N. Samarth, and E. Zeldov, "Visualization of superparamagnetic dynamics in magnetic topological insulators," *Sci. Adv.*, vol. 1, no. 10, p. e1500740, 2015.

[5] I. Lee, C. K. Kim, J. Lee, S. J. L. Billinge, R. D. Zhong, J. A. Schneeloch, T. S. Liu, T. Valla, J. M. Tranquada, G. D. Gu, and J. C. S. Davis, "Imaging Dirac-mass disorder from magnetic dopant atoms in the ferromagnetic topological insulator $Cr_x(Bi_{0.1}Sb_{0.9})_{2-x}Te_3$," *Proc. Natl. Acad. Sci. U. S. A.*, vol. 112, no. 5, pp. 1316–1321, 2015.

[6] I. Kezsmarki, S. Bordacs, P. Milde, E. Neuber, L. M. Eng, J. S. White, H. M. Rønnow, C. D. Dewhurst, M. Mochizuki, K. Yanai, H. Nakamura, D. Ehlers, V. Tsurkan, and A. Loidl, "Neel-type skyrmion lattice with confined orientation in the polar magnetic semiconductor GaV_4S_8," *Nat. Mater.*, vol. 14, no. 11, pp. 1116–1122, 2015.

[7] X. Z. Yu, Y. Onose, N. Kanazawa, J. H. Park, J. H. Han, Y. Matsui, N. Nagaosa, and Y. Tokura, "Real-space observation of a two-dimensional skyrmion crystal," *Nature*, vol. 465, no. 7300, pp. 901–904, 2010.

[8] X. Z. Yu, N. Kanazawa, Y. Onose, K. Kimoto, W. Z. Zhang, S. Ishiwata, Y. Matsui, and Y. Tokura, "Near room-temperature formation of a skyrmion crystal in thin-films of the helimagnet FeGe," *Nat. Mater.*, vol. 10, no. 2, pp. 106–109, 2011.

[9] A. Fert, N. Reyren, and V. Cros, "Magnetic skyrmions: advances in physics and potential applications," *Nat. Rev. Mater.*, vol. 2, no. 7, p. 17031, 2017.

[10] S. Heinze, K. von Bergmann, M. Menzel, J. Brede, A. Kubetzka, R. Wiesendanger, G. Bihlmayer, and S. Blügel, "Spontaneous atomic-scale magnetic skyrmion lattice in two dimensions," *Nat. Phys.*, vol. 7, no. 9, pp. 713–718, 2011.

[11] Y. Taguchi, Y. Oohara, H. Yoshizawa, N. Nagaosa, and Y. Tokura, "Spin chirality, Berry phase, and anomalous Hall effect in a frustrated ferromagnet," *Science*, vol. 291, no. 5513, pp. 2573–2576, 2001.

[12] N. Nagaosa and Y. Tokura, "Topological properties and dynamics of magnetic skyrmions," *Nat. Nanotechnol.*, vol. 8, no. 12, pp. 899–911, 2013.

[13] Y. Li, N. Kanazawa, X. Z. Yu, A. Tsukazaki, M. Kawasaki, M. Ichikawa, X. F. Jin, F. Kagawa, and Y. Tokura, "Robust formation of skyrmions and topological hall effect anomaly in epitaxial thin films of MnSi," *Phys. Rev. Lett.*, vol. 110, no. 11, p. 117202, 2013.

[14] Y. Ou, C. Liu, G. Jiang, Y. Feng, D. Zhao, W. Wu, X.-X. Wang, W. Li, C. Song, L.-L. Wang, W. Wang, W. Wu, Y. Wang, K. He, X.-C. Ma, and Q.-K. Xue, "Enhancing the quantum anomalous Hall effect by magnetic codoping in a topological insulator," *Adv. Mater.*, vol. 1703062, p. 1703062, 2017.

[15] D. Xiao, J. Jiang, J. H. Shin, W. Wang, F. Wang, Y. F. Zhao, C. Liu, W. Wu, M. H. Chan, N. Samarth, and C. Z. Chang, "Realization of the Axion Insulator State in Quantum Anomalous Hall Sandwich Heterostructures," *Phys. Rev. Lett.*, vol. 120, no. 5, p. 56801, 2018.

[16] X. Feng, Y. Feng, J. Wang, Y. Ou, Z. Hao, C. Liu, Z. Zhang, L. Zhang, C. Lin, J. Liao, Y. Li, L. L. Wang, S. H. Ji, X. Chen, X. Ma, S. C. Zhang, Y. Wang, K. He, and Q. K. Xue, "Thickness dependence of the quantum anomalous Hall effect in magnetic topological insulator films," *Adv. Mater.*, pp. 6386–6390, 2016.

[17] H. Weng, R. Yu, X. Hu, X. Dai, and Z. Fang, "Quantum anomalous Hall effect and related topological electronic states," *Adv. Phys.*, vol. 64, pp. 227–282, 2015.

[18] D. Xiao, M. C. Chang, and Q. Niu, "Berry phase effects on electronic properties," *Rev. Mod. Phys.*, vol. 82, pp. 1959–2007, 2010.

[19] R. Karplus and J. M. Luttinger, "Hall effect in ferromagnetics," *Phys. Rev.*, vol. 95, no. 5, pp. 1154–1160, 1954.

[20] K. V. Klitzing, G. Dorda, and M. Pepper, "New method for high-accuracy determination of the fine-structure constant based on quantized hall resistance," *Phys. Rev. Lett.*, vol. 45, no. 6, pp. 494–497, 1980.

[21] D. J. Thouless, M. Kohmoto, M. P. Nightingale, and M. Den Nijs, "Quantized Hall conductance in a two-Dimensional periodic potential," *Phys. Rev. Lett.*, vol. 49, no. 6, pp. 405–408, 1982.

[22] F. D. M. Haldane, "Model for a quantum Hall effect without landau levels: condensed-matter realization of the "parity anomaly"," *Phys. Rev. Lett.*, vol. 61, no. 18, pp. 2015–2018, 1988.

[23] C. X. Liu, X. L. Qi, X. Dai, Z. Fang, and S. C. Zhang, "Quantum anomalous Hall effect in $Hg_{1-y}Mn_{1-y}Te$ quantum wells," *Phys. Rev. Lett.*, vol. 101, no. 14, p. 146802, 2008.

[24] L. Fu, C. L. Kane, and E. J. Mele, "Topological Insulators in Three Dimensions," vol. 98, no. March, p. 106803, 2007.

[25] D. Hsieh, D. Qian, L. Wray, Y. Xia, Y. S. Hor, R. J. Cava, and M. Z. Hasan, "A topological Dirac insulator in a quantum spin Hall phase," *Nature*, vol. 452, no. 7190, pp. 970–974, 2008.

[26] Y. Xia, D. Qian, D. Hsieh, L. Wray, A. Pal, H. Lin, A. Bansil, D. Grauer, Y. S. Hor, R. J. Cava, and M. Z. Hasan, "Observation of a large-gap topological-insulator class with a single Dirac cone on the surface," *Nat. Phys.*, vol. 5, no. 6, pp. 398–402, 2009.

[27] D. Hsieh, Y. Xia, D. Qian, L. Wray, J. H. Dil, F. Meier, J. Osterwalder, L. Patthey, J. G. Checkelsky, N. P. Ong, A. V. Fedorov, H. Lin, A. Bansil, D. Grauer, Y. S. Hor, R. J. Cava, and M. Z. Hasan, "A tunable topological insulator in the spin helical Dirac transport regime," *Nature*, vol. 460, no. 7259, pp. 1101–1105, 2009.

[28] Y. L. Chen, J. G. Analytis, J.-H. Chu, Z. K. Liu, S.-K. Mo, X. L. Qi, H. J. Zhang, D. H. Lu, X. Dai, Z. Fang, S. C. Zhang, I. R. Fisher, Z. Hussain, and Z.-X. Shen, "Experimental realization of a three-dimensional topological insulator, Bi_2Te_3," *Science*, vol. 325, p. 178, 2009.

[29] H. Zhang, C.-x. Liu, X.-l. Qi, X. Dai, Z. Fang, and S.-c. Zhang, "Topological insulators in Bi_2Se_3, Bi_2Te_3 and Sb_2Te_3 with a single Dirac cone on the surface," *Nat. Phys.*, vol. 5, no. 6, pp. 438–442, 2009.

[30] D. Hsieh, Y. Xia, D. Qian, L. Wray, F. Meier, J. H. Dil, J. Osterwalder, L. Patthey, A. V. Fedorov, H. Lin, A. Bansil, D. Grauer, Y. S. Hor, R. J. Cava, and M. Z. Hasan, "Observation of time-reversal-protected single-dirac-cone topological-insulator states in Bi_2Te_3 and Sb_2Te_3," *Phys. Rev. Lett.*, vol. 103, no. 14, pp. 2–5, 2009.

[31] Y. S. Hor, P. Roushan, H. Beidenkopf, J. Seo, D. Qu, J. G. Checkelsky, L. A. Wray, D. Hsieh, Y. Xia, S. Y. Xu, D. Qian, M. Z. Hasan, N. P. Ong, A. Yazdani, and R. J. Cava, "Development of ferromagnetism in the doped topological insulator Bi_{2-x} Mn_xTe_3," *Phys. Rev. B*, vol. 81, no. 19, p. 195203, 2010.

[32] J. S. Dyck, Č. Drašar, P. Lošt'ák, and C. Uher, "Low-temperature ferromagnetic properties of the diluted magnetic semiconductor $Sb_{2-x}Cr_xTe_3$," *Phys. Rev. B*, vol. 71, no. 11, p. 115214, 2005.

[33] Z. Zhou, Y.-J. Chien, and C. Uher, "Thin film dilute ferromagnetic semiconductors $Sb_{2-x}Cr_xTe_3$ with a Curie temperature up to 190 K," vol. 74, p. 224418, 2006.

[34] J. S. Dyck, P. Hájek, P. Lošt'ák, and C. Uher, "Diluted magnetic semiconductors based on Sb $_{2-x}$ V_x Te_3 ($0.01 \leq x \leq 0.03$)," *Phys. Rev. B*, vol. 65, p. 115212, 2002.

[35] P. P. J. Haazen, J.-B. Laloë, T. J. Nummy, H. J. M. Swagten, P. Jarillo-Herrero, D. Heiman, and J. S. Moodera, "Ferromagnetism in thin-film Cr-doped topological insulator Bi_2Se_3," *Appl. Phys. Lett.*, vol. 100, no. 2012, p. 082404, 2015.

[36] J. G. Checkelsky, R. Yoshimi, A. Tsukazaki, K. S. Takahashi, Y. Kozuka, J. Falson, M. Kawasaki, and Y. Tokura, "Trajectory of the anomalous Hall effect towards the quantized state in a ferromagnetic topological insulator," *Nat. Phys.*, vol. 10, p. 731, Aug 2014.

[37] X. Kou, S.-T. Guo, Y. Fan, L. Pan, M. Lang, Y. Jiang, Q. Shao, T. Nie, K. Murata, J. Tang, Y. Wang, L. He, T.-K. Lee, W.-L. Lee, and K. L. Wang, "Scale-invariant

quantum anomalous Hall effect in magnetic topological insulators beyond the two-dimensional limit," *Phys. Rev. Lett.*, vol. 113, p. 137201, Sep 2014.

[38] C.-Z. Chang, W. Zhao, D. Y. Kim, H. Zhang, B. A. Assaf, D. Heiman, S.-C. Zhang, C. Liu, M. H. W. Chan, and J. S. Moodera, "High-precision realization of robust quantum anomalous Hall state in a hard ferromagnetic topological insulator," *Nat. Mater.*, vol. 14, p. 473, 2015.

[39] C.-Z. Chang, P. Tang, Y.-L. Wang, X. Feng, K. Li, Z. Zhang, Y. Wang, L.-L. Wang, X. Chen, C. Liu, W. Duan, K. He, X.-C. Ma, and Q.-K. Xue, "Chemical-potential-dependent gap opening at the dirac surface states of Bi_2Se_3 induced by aggregated substitutional Cr atoms," *Phys. Rev. Lett.*, vol. 112, p. 056801, Feb 2014.

[40] S. Grauer, S. Schreyeck, M. Winnerlein, K. Brunner, C. Gould, and L. W. Molenkamp, "Coincidence of superparamagnetism and perfect quantization in the quantum anomalous Hall state," *Phys. Rev. B*, vol. 92, no. 20, p. 201304(R), 2015.

[41] M. Mogi, R. Yoshimi, A. Tsukazaki, K. Yasuda, Y. Kozuka, K. S. Takahashi, M.Kawasaki, and Y. Tokura, "Magnetic modulation doping in topological insulators toward higher-temperature quantum anomalous Hall effect," *Appl. Phys. Lett.*, vol. 107, no. 18, p. 182401, 2015.

[42] W. Li, M. Claassen, C.-Z. Chang, B. Moritz, T. Jia, C. Zhang, S. Rebec, J. J. Lee, M. Hashimoto, D.-H. Lu, R. G. Moore, J. S. Moodera, T. P. Devereaux, and Z.-X. Shen, "Origin of the low critical observing temperature of the quantum anomalous Hall effect in V-doped $(Bi, Sb)_2Te_3$ film," *Sci. Rep.*, vol. 6, p. 32732, 2016.

[43] P. W. Anderson, "Absence of diffusion in certain random lattices," *Phys. Rev.*, vol. 109, pp. 1492–1505, 1958.

[44] A. N. Andriotis and M. Menon, "Defect-induced magnetism: Codoping and a prescription for enhanced magnetism," *Phys. Rev. B*, vol. 87, no. 15, p. 155309, 2013.

[45] S. F. Qi, Z. H. Qiao, X. Z. Deng, E. D. Cubuk, H. Chen, W. G. Zhu, E. Kaxiras, S. B. Zhang, X. H. Xu, and Z. Y. Zhang, "High-temperature quantum anomalous Hall effect in n-p codoped topological insulators," *Phys. Rev. Lett.*, vol. 117, no. 5, p. 056804, 2016.

[46] X.-L. Qi, T. L. Hughes, and S.-C. Zhang, "Topological field theory of time-reversal invariant insulators," *Phys. Rev. B*, vol. 78, no. 19, p. 195424, 2008.

[47] J. Wang, B. Lian, X.-L. Qi, and S.-C. Zhang, "Quantized topological magnetoelectric effect of the zero-plateau quantum anomalous Hall state," *Phys. Rev. B*, vol. 92, no. 8, p. 081107(R), 2015.

[48] T. Morimoto, A. Furusaki, and N. Nagaosa, "Topological magnetoelectric effects in thin films of topological insulators," *Phys. Rev. B*, vol. 92, no. 8, p. 085113, 2015.

[49] W. K. Tse and A. H. MacDonald, "Giant magneto-optical kerr effect and universal faraday effect in thin-film topological insulators," *Phys. Rev. Lett.*, vol. 105, no. 5, p. 057401, 2010.

[50] L. Wu, M. Salehi, N. Koirala, J. Moon, S. Oh, and N. P. Armitage, "Quantized Faraday and Kerr rotation and axion electrodynamics of a 3D topological insulator," *Science*, vol. 354, no. 6316, pp. 1124–1127, 2016.

[51] X.-L. Qi, R. Li, J. Zang, and S.-C. Zhang, "Inducing a Magnetic Monopole with Topological Surface States," *Science*, vol. 323, pp. 1184–1187, 2009.

[52] M. Mogi, M. Kawamura, R. Yoshimi, A. Tsukazaki, Y. Kozuka, N. Shirakawa, K. S. Takahashi, M. Kawasaki, and Y. Tokura, "A magnetic heterostructure of topological insulators as a candidate for an axion insulator," *Nat. Mater.*, vol. 16, no. 5, pp. 516–521, 2017.

[53] X. Kou, L. Pan, J. Wang, Y. Fan, E. S. Choi, W.-L. Lee, T. Nie, K. Murata, Q. Shao,

S.-C. Zhang, and K. L. Wang, "Metal-to-insulator switching in quantum anomalous Hall states," *Nat. Commun.*, vol. 6, p. 8474, 2015.

[54] Y. Feng, X. Feng, Y. Ou, J. Wang, C. Liu, L. Zhang, D. Zhao, G. Jiang, S. C. Zhang, K. He, X. Ma, Q. K. Xue, and Y. Wang, "Observation of the Zero Hall Plateau in a Quantum Anomalous Hall Insulator," *Phys. Rev. Lett.*, vol. 115, no. 12, p. 126801, 2015.

[55] J. Wang, B. Lian, and S. C. Zhang, "Universal scaling of the quantum anomalous Hall plateau transition," *Phys. Rev. B*, vol. 89, no. 8, p. 085106, 2014.

[56] M. Mogi, M. Kawamura, A. Tsukazaki, R. Yoshimi, K. S. Takahashi, M. Kawasaki, and Y. Tokura, "Tailoring tricolor structure of magnetic topological insulator for robust axion insulator," *Sci. Adv.*, vol. 3, p. eaao1669, 2017.

[57] I. Dzyaloshinsky, "A thermodynamic theory of weak ferromagnetism of antiferromagnetics," *J. Phys. Chem. Solids*, vol. 4, no. 4, pp. 241–255, 1958.

[58] T. Moriya, "Anisotropic superexchange interaction and weak ferromagnetism," *Phys. Rev.*, vol. 120, no. 1949, pp. 91–98, 1960.

[59] S. Mühlbauer, B. Binz, F. Jonietz, C. Pfleiderer, A. Rosch, A. Neubauer, R. Georgii, and P. Böni, "Skyrmion Lattice in a Chiral Magnet," *Science*, vol. 323, pp. 915–920, 2009.

[60] W. Münzer, A. Neubauer, T. Adams, S. Mühlbauer, C. Franz, F. Jonietz, R. Georgii, P. Böni, B. Pedersen, M. Schmidt, A. Rosch, and C. Pfleiderer, "Skyrmion lattice in the doped semiconductor $Fe_{1-x}Co_xSi$," *Phys. Rev. B*, vol. 81, no. 4, p. 041203(R), 2010.

[61] S. Woo, K. Litzius, B. Krüger, M. Y. Im, L. Caretta, K. Richter, M. Mann, A. Krone, R. M. Reeve, M. Weigand, P. Agrawal, I. Lemesh, M. A. Mawass, P. Fischer, M. Kläui,

and G. S. Beach, "Observation of room-temperature magnetic skyrmions and their current-driven dynamics in ultrathin metallic ferromagnets," *Nat. Mater.*, vol. 15, no. 5, pp. 501–506, 2016.

[62] A. Soumyanarayanan, M. Raju, A. L. Oyarce, A. K. Tan, M. Y. Im, A. P. Petrovic, P. Ho, K. H. Khoo, M. Tran, C. K. Gan, F. Ernult, and C. Panagopoulos, "Tunable room-temperature magnetic skyrmions in Ir/Fe/Co/Pt multilayers," *Nat. Mater.*, vol. 16, no. 9, pp. 898–904, 2017.

[63] A. Neubauer, C. Pfleiderer, B. Binz, A. Rosch, R. Ritz, P. G. Niklowitz, and P. Böni, "Topological hall effect in the A phase of MnSi," *Phys. Rev. Lett.*, vol. 102, no. 18, p. 186602, 2009.

[64] S. X. Huang and C. L. Chien, "Extended skyrmion phase in epitaxial FeGe(111) thin films," *Phys. Rev. Lett.*, vol. 108, no. 26, p. 267201, 2012.

[65] K. Yasuda, R. Wakatsuki, T. Morimoto, R. Yoshimi, A. Tsukazaki, K. S. Takahashi, M. Ezawa, M. Kawasaki, N. Nagaosa, and Y. Tokura, "Geometric Hall effects in topological insulator heterostructures," *Nat. Phys.*, vol. 12, no. 6, pp. 555–559, 2016.

[66] C. Liu, Y. Y. Zang, W. Ruan, Y. Gong, K. He, X. C. Ma, Q. K. Xue, and Y. Y. Wang, "Dimensional crossover-induced topological Hall effect in a magnetic topological insulator," *Phys. Rev. Lett.*, vol. 119, no. 17, p. 176809, 2017.

[67] D. Zhao, L. Zhang, I. A. Malik, M. Liao, W. Cui, X. Cai, C. Zheng, L. Li, X. Hu, D. Zhang, J. Zhang, X. Chen, W. Jiang, and Q. Xue, "Observation of unconventional anomalous Hall effect in epitaxial CrTe thin films," *Nano Res.*, vol. 11, no. 6, pp. 3116–3121, 2018.

[68] J. Matsuno, N. Ogawa, K. Yasuda, F. Kagawa, W. Koshibae, N. Nagaosa, Y. Tokura, and M. Kawasaki, "Interface-driven topological Hall effect in $SrRuO_3$-$SrIrO_3$ bilayer," *Science Adv.*, vol. 2, no. 7, p. e1600304, 2016.

[69] Y. Ohuchi, J. Matsuno, N. Ogawa, Y. Kozuka, M. Uchida, Y. Tokura, and M. Kawasaki, "Electric-field control of anomalous and topological Hall effects in oxide bilayer thin films," *Nat. Commun.*, vol. 9, no. 1, p. 213, 2018.

[70] S. W. Cheong and M. Mostovoy, "Multiferroics: A magnetic twist for ferroelectricity," *Nat. Mater.*, vol. 6, no. 1, pp. 13–20, 2007.

[71] Y. Geng, H. Das, A. L. Wysocki, X. Wang, S. W. Cheong, M. Mostovoy, C. J. Fennie, and W. Wu, "Direct visualization of magnetoelectric domains," *Nat. Mater.*, vol. 13, no. 2, pp. 163–167, 2014.

[72] L. Balents, "Spin liquids in frustrated magnets," *Nature*, vol. 464, no. 7286, pp. 199–208, 2010.

[73] P. Bak, "Commensurate phases , incommensurate phases and the devil ' s staircase," *Rep. Prog. Phys.*, vol. 45, p. 587, 1982.

[74] U. Hartmann, "Magnetic Force Microscopy," vol. 29, pp. 53–87, 1999.

[75] D. Vasyukov, Y. Anahory, L. Embon, D. Halbertal, J. Cuppens, L. Neeman, A. Finkler, Y. Segev, Y. Myasoedov, M. L. Rappaport, M. E. Huber, and E. Zeldov, "A scanning superconducting quantum interference device with single electron spin sensitivity," *Nat. Nanotechnol.*, vol. 8, no. 9, pp. 639–644, 2013.

[76] "Probing condensed matter physics with magnetometry based on nitrogen-vacancy centres in diamond," *Nat. Rev. Mater.*, vol. 3, p. 17088, 2018.

[77] M. Yamanouchi, D. Chiba, F. Matsukura, T. Dietl, and H. Ohno, "Velocity of domain-wall motion induced by electrical current in the ferromagnetic semiconductor (Ga,Mn)As," *Phys. Rev. Lett.*, vol. 96, no. 9, pp. 10–13, 2006.

[78] F. J. Giessibl, "Advances in atomic force microscopy," *Rev. Mod. Phys.*, vol. 75, no. 3, pp. 949–983, 2003.

[79] G. Binnig and C. F. Quate, "Atomic force microscope," *Phys. Rev. Lett.*, vol. 56, no. 9, pp. 930–933, 1986.

[80] G. Binnig, H. Rohrer, C. Gerber, and E. Weibel, "Surface studies by scanning tunneling microscopy," *Phys. Rev. Lett.*, vol. 49, no. 1, pp. 57–61, 1982.

[81] P. Girard, "Electrostatic force microscopy: principles and some applications to semiconductors," *Nanotechnology*, vol. 12, no. 4, pp. 485–490, 2001.

[82] D. Rugar, H. J. Mamin, P. Guethner, S. E. Lambert, J. E. Stern, I. McFadyen, and T. Yogi, "Magnetic force microscopy: General principles and application to longitudinal recording media," *J. Appl. Phys.*, vol. 68, no. 3, pp. 1169–1183, 1990.

[83] H. Takahashi, K. Ando, and Y. Shirakawabe, "Self-sensing piezoresistive cantilever and its magnetic force microscopy applications," *Ultramicroscopy*, vol. 91, no. 1-4, pp. 63–72, 2002.

[84] M. Itoh, R. Wang, Y. Inaguma, T. Yamaguchi, Y. J. Shan, and T. Nakamura, "Ferroelectricity induced by oxygen isotope exchange in strontium titanate perovskite," *Phys. Rev. Lett.*, vol. 82, no. 17, pp. 3540–3543, 1999.

[85] N. A. Spaldin and M. Fiebig, "The renaissance of magnetoelectric multiferroics," *Science*, vol. 309, no. 5733, pp. 391–392, 2005.

[86] W. Eerenstein, N. D. Mathur, and J. F. Scott, "Multiferroic and magnetoelectric materials," *Nature*, vol. 442, no. 7104, pp. 759–765, 2006.

[87] R. Ramesh and N. A. Spaldin, "Multiferroics: progress and prospects in thin films," *Nat. Mater.*, vol. 6, no. 1, pp. 21–29, 2007.

[88] S. Dong, J. M. Liu, S. W. Cheong, and Z. F. Ren, "Multiferroic materials and magnetoelectric physics: symmetry, entanglement, excitation, and topology," *Adv. Phys.*, vol. 64, no. 5-6, pp. 519–626, 2015.

[89] M. Fiebig, "Revival of the magnetoelectric effect," *J. Phys. D: Appl. Phys.*, vol. 38, no. 8, pp. R123–R152, 2005.

[90] J. P. Rivera, "A short review of the magnetoelectric effect and related experimental techniques on single phase (multi-) ferroics," *Eur. Phys. J. B*, vol. 71, no. 3, pp. 299–313, 2009.

[91] K. F. Wang, J. M. Liu, and Z. F. Ren, "Multiferroicity: the coupling between magnetic and polarization orders," *Adv. Phys.*, vol. 58, no. 4, pp. 321–448, 2009.

[92] M. Bibes and A. Barthelemy, "Multiferroics: Towards a magnetoelectric memory," *Nat. Mater.*, vol. 7, no. 6, pp. 425–426, 2008.

[93] N. Hur, S. Park, P. A. Sharma, J. S. Ahn, S. Guha, and S. W. Cheong, "Electric polarization reversal and memory in a multiferroic material induced by magnetic fields," *Nature*, vol. 429, no. 6990, pp. 392–395, 2004.

[94] S. Dong, J. Zhai, F. Bai, J. F. Li, and D. Viehland, "Push-pull mode magnetostrictive/piezoelectric laminate composite with an enhanced magnetoelectric voltage coefficient," *Appl. Phys. Lett.*, vol. 87, no. 6, p. 062502, 2005.

[95] J. Ryu, S. Priya, K. Uchino, and H. E. Kim, "Magnetoelectric effect in composites of magnetostrictive and piezoelectric materials," *J. Electroceram.*, vol. 8, no. 2, pp. 107–119, 2002.

[96] S. Shastry, G. Srinivasan, M. I. Bichurin, V. M. Petrov, and A. S. Tatarenko, "Microwave magnetoelectric effects in single crystal bilayers of yttrium iron garnet and lead magnesium niobate-lead titanate," *Phys. Rev. B*, vol. 70, no. 6, p. 064416, 2004.

[97] A. S. Tatarenko, V. Gheevarughese, and G. Srinivasan, "Magnetoelectric microwave bandpass filter," *Electron. Lett.*, vol. 42, no. 9, pp. 540–541, 2006.

[98] G. A. Smolenskii and I. E. Chupis, "Ferroelectromagnets," *Phys.-Usp.*, vol. 25, no. 7, p. 475, 1982.

[99] J. Wang, J. B. Neaton, H. Zheng, V. Nagarajan, S. B. Ogale, B. Liu, D. Viehland, V. Vaithyanathan, D. G. Schlom, U. V. Waghmare, N. A. Spaldin, K. M. Rabe, M. Wuttig, and R. Ramesh, "Epitaxial $BiFeO_3$ multiferroic thin film heterostructures," *Science*, vol. 299, no. 5613, pp. 1719–1722, 2003.

[100] C. Ederer and C. J. Fennie, "Electric-field switchable magnetization via the Dzyaloshinskii-Moriya interaction: $FeTiO_3$ versus $BiFeO_3$," *J. Phys.: Condens. Matter*, vol. 20, no. 43, p. 434219, 2008.

[101] C. J. Fennie, "Ferroelectrically induced weak ferromagnetism by design," *Phys. Rev. Lett.*, vol. 100, no. 16, p. 167203, 2008.

[102] G. Catalan and J. F. Scott, "Physics and Applications of Bismuth ferrite," *Adv. Mater.*, vol. 21, no. 24, pp. 2463–2485, 2009.

[103] T. Katsufuji, S. Mori, M. Masaki, Y. Moritomo, N. Yamamoto, and H. Takagi, "Dielectric and magnetic anomalies and spin frustration in hexagonal $RMnO_3$ (R = Y, Yb, and Lu)," *Phys. Rev. B*, vol. 64, no. 10, p. 104419, 2001.

[104] M. Fiebig, T. Lottermoser, D. Frohlich, A. V. Goltsev, and R. V. Pisarev, "Observation of coupled magnetic and electric domains," *Nature*, vol. 419, no. 6909, pp. 818–820, 2002.

[105] B. B. V. Aken, T. T. M. Palstra, A. Filippetti, and N. A. Spaldin, "The origin of ferroelectricity in magnetoelectric $YMnO_3$," *Nat. Mater.*, vol. 3, no. 3, pp. 164–170, 2004.

[106] F. Yen, C. dela Cruz, B. Lorenz, E. Galstyan, Y. Y. Sun, M. Gospodinov, and C. W. Chu, "Magnetic phase diagrams of multiferroic hexagonal $RMnO_3$ (R = Er, Yb, Tm, and ho)," *J. Mater. Res.*, vol. 22, no. 8, pp. 2163–2173, 2007.

[107] Y. Geng, H. Das, A. L. Wysocki, X. Wang, S. W. Cheong, M. Mostovoy, C. J. Fennie, and W. Wu, "Direct visualization of magnetoelectric domains," *Nat. Mater.*, vol. 13, no. 2, pp. 163–167, 2014.

[108] A. R. Akbashev, A. S. Semisalova, N. S. Perov, and A. R. Kaul, "Weak ferromagnetism in hexagonal orthoferrites $RFeO_3$ (R = Lu, Er-Tb)," *Appl. Phys. Lett.*, vol. 99, no. 12, p. 122502, 2011.

[109] Y. K. Jeong, J.-H. Lee, S.-J. Ahn, and H. M. Jang, "Epitaxially Constrained Hexagonal Ferroelectricity and Canted Triangular Spin Order in $LuFeO_3$ Thin films," *Chem. Mater.*, vol. 24, no. 13, pp. 2426–2428, 2012.

[110] H. Iida, T. Koizumi, Y. Uesu, K. Kohn, N. Ikeda, S. Mori, R. Haumont, P. E. Janolin, J. M. Kiat, M. Fukunaga, and Y. Noda, "Ferroelectricity and Ferrimagnetism of Hexagonal $YbFeO_3$ Thin films," *J. Phys. Soc. Jpn.*, vol. 81, no. 2, p. 024719, 2012.

[111] W. B. Wang, J. Zhao, W. B. Wang, Z. Gai, N. Balke, M. F. Chi, H. N. Lee, W. Tian, L. Y. Zhu, X. M. Cheng, D. J. Keavney, J. Y. Yi, T. Z. Ward, P. C. Snijders, H. M. Christen, W. D. Wu, J. Shen, and X. S. Xu, "Room-temperature Multiferroic Hexagonal $LuFeO_3$ films," *Phys. Rev. Lett.*, vol. 110, no. 23, p. 237601, 2013.

[112] J. A. Moyer, R. Misra, J. A. Mundy, C. M. Brooks, J. T. Heron, D. A. Muller, D. G. Schlom, and P. Schiffer, "Intrinsic magnetic properties of hexagonal $LuFeO_3$ and the effects of nonstoichiometry," *APL Mater.*, vol. 2, no. 1, p. 012106, 2014.

[113] X. S. Xu and W. B. Wang, "Multiferroic hexagonal ferrites (h-$RFeO_3$, R = Y, Dy-Lu): a brief experimental review," *Mod. Phys. Lett. B*, vol. 28, no. 21, p. 1430008, 2014.

[114] S. M. Disseler, J. A. Borchers, C. M. Brooks, J. A. Mundy, J. A. Moyer, D. A. Hillsberry, E. L. Thies, D. A. Tenne, J. Heron, M. E. Holtz, J. D. Clarkson, G. M. Stiehl, P. Schiffer, D. A. Muller, D. G. Schlom, and W. D. Ratcliff, "Magnetic Structure

and Ordering of MultiferroicHexagonal $LuFeO_3$," *Phys. Rev. Lett.*, vol. 114, no. 21, p. 217602, 2015.

[115] H. Das, A. L. Wysocki, Y. N. Geng, W. D. Wu, and C. J. Fennie, "Bulk magnetoelectricity in the hexagonal manganites and ferrites," *Nat. Commun.*, vol. 5, p. 2998, 2014.

[116] W. Wang, J. A. Mundy, C. M. Brooks, J. A. Moyer, M. E. Holtz, D. A. Muller, D. G. Schlom, and W. Wu, "Visualizing weak ferromagnetic domains in multiferroic hexagonal ferrite thin film," *Phys. Rev. B*, vol. 95, no. 13, p. 134443, 2017.

[117] V. Gehanno, A. Marty, B. Gilles, and Y. Samson, "Magnetic domains in epitaxial ordered FePd(001) thin films with perpendicular magnetic anisotropy," *Phys. Rev. B*, vol. 55, no. 18, pp. 12552–12555, 1997.

[118] A. Hubert and R. Schafer, *Magnetic domains*. Springer Berlin Heidelberg, 1998.

[119] G. Koster, L. Klein, W. Siemons, G. Rijnders, J. S. Dodge, C. B. Eom, D. H. A. Blank, and M. R. Beasley, "Structure, physical properties, and applications of $SrRuO_3$ thin films," *Rev. Mod. Phys.*, vol. 84, no. 1, pp. 253–298, 2012.

[120] W. Wang, F. Yang, C. Gao, J. Jia, G. D. Gu, and W. Wu, "Visualizing ferromagnetic domains in magnetic topological insulators," *APL Mater.*, vol. 3, no. 8, p. 083301, 2015.

[121] H. Li, Y. R. Song, M.-Y. Yao, F. Yang, L. Miao, F. Zhu, C. Liu, C. L. Gao, D. Qian, X. Yao, J.-F. Jia, Y. J. Shi, and D. Wu, "Carriers dependence of the magnetic properties in magnetic topological insulator $Sb_{1.95x}Bi_xCr_{0.05}Te_3$," *Appl. Phys. Lett.*, vol. 101, no. 7, p. 072406, 2012.

[122] W. Wang, C.-Z. Chang, J. S. Moodera, and W. Wu, "Visualizing ferromagnetic domain behavior of magnetic topological insulator thin films," *npj Quantum Mater.*, vol. 1, no. 1, p. 16023, 2016.

[123] A. Schwarz, M. Liebmann, U. Kaiser, R. Wiesendanger, T. W. Noh, and D. W. Kim, "Visualization of the Barkhausen effect by magnetic force microscopy," *Phys. Rev. Lett.*, vol. 92, no. 7, p. 077206, 2004.

[124] A. J. Bestwick, E. J. Fox, X. Kou, L. Pan, K. L. Wang, and D. Goldhaber-Gordon, "Precise quantization of the anomalous Hall effect near zero magnetic field," *Phys. Rev. Lett.*, vol. 114, no. 18, p. 187201, 2015.

[125] S. Grauer, S. Schreyeck, M. Winnerlein, K. Brunner, C. Gould, and L. W. Molenkamp, "Coincidence of superparamagnetism and perfect quantization in the quantum anomalous Hall state," *Phys. Rev. B*, vol. 92, no. 20, p. 201304, 2015.

[126] J. F. Gregg, W. Allen, K. Ounadjela, M. Viret, M. Hehn, S. M. Thompson, and J. M. D. Coey, "Giant magnetoresistive effects in a single element magnetic thin film," *Phys. Rev. Lett.*, vol. 77, no. 8, pp. 1580–1583, 1996.

[127] A. D. Kent, J. Yu, U. Rudiger, and S. S. P. Parkin, "Domain wall resistivity in epitaxial thin film microstructures," *J. Physics-condensed Matter*, vol. 13, no. 25, pp. R461–R488, 2001.

[128] W. Wang, Y. Ou, C. Liu, Y. Wang, K. He, Q. K. Xue, and W. Wu, "Direct evidence of ferromagnetism in a quantum anomalous Hall system," *Nat. Phys.*, vol. 14, no. August, p. 791, 2018.

[129] N. Nagaosa, J. Sinova, S. Onoda, A. H. MacDonald, and N. P. Ong, "Anomalous Hall effect," *Rev. Mod. Phys.*, vol. 82, no. 2, pp. 1539–1592, 2010.

[130] R. Yu, W. Zhang, H. J. Zhang, S. C. Zhang, X. Dai, and Z. Fang, "Quantized anomalous Hall effect in magnetic topological insulators," *Science*, vol. 329, no. 5987, pp. 61–64, 2010.

[131] M. Li, C.-Z. Chang, L. Wu, J. Tao, W. Zhao, M. H. W. Chan, J. S. Moodera, J. Li, and

Y. Zhu, "Experimental verification of the Van Vleck nature of long-range ferromagnetic order in the vanadium-doped three-dimensional topological insulator Sb_2Te_3," *Phys. Rev. Lett.*, vol. 114, p. 146802, Apr 2015.

[132] P. Sessi, F. Reis, T. Bathon, K. A. Kokh, O. E. Tereshchenko, and M. Bode, "Signatures of Dirac fermion-mediated magnetic order," *Nat. Commun.*, vol. 5, p. 5349, 2014.

[133] C.-Z. Chang, W. Zhao, D. Y. Kim, P. Wei, J. K. Jain, C. Liu, M. H. W. Chan, and J. S. Moodera, "Zero-field dissipationless chiral edge transport and the nature of dissipation in the quantum anomalous hall state," *Phys. Rev. Lett.*, vol. 115, p. 057206, Jul 2015.

[134] S. Grauer, K. M. Fijalkowski, S. Schreyeck, M. Winnerlein, K. Brunner, R. Thomale, C. Gould, and L. W. Molenkamp, "Scaling of the quantum anomalous Hall effect as an indicator of axion electrodynamics," *Phys. Rev. Lett.*, vol. 118, no. 24, p. 246801, 2017.

[135] Y. Zhang, K. He, C.-Z. Chang, C.-L. Song, L.-L. Wang, X. Chen, J.-F. Jia, Z. Fang, X. Dai, W.-Y. Shan, S.-Q. Shen, Q. Niu, X.-L. Qi, S.-C. Zhang, X.-C. Ma, and Q.-K. Xue, "Crossover of the three-dimensional topological insulator Bi2Se3 to the two-dimensional limit," *Nat. Phys.*, vol. 6, no. 8, pp. 584–588, 2010.

[136] Y. Jiang, Y. Wang, M. Chen, Z. Li, C. Song, K. He, L. Wang, X. Chen, X. Ma, and Q. K. Xue, "Landau quantization and the thickness limit of topological insulator thin films of Sb_2Te_3," *Phys. Rev. Lett.*, vol. 108, no. 1, p. 016401, 2012.

[137] P. Walser, M. Hunziker, T. Speck, and M. Landolt, "Heat-induced antiferromagnetic coupling in multilayers with ZnSe spacers," *Phys. Rev. B*, vol. 60, no. 6, pp. 4082–4086, 1999.

[138] J. Faure-Vincent, C. Tiusan, C. Bellouard, E. Popova, M. Hehn, F. Montaigne, and

A. Schuhl, "Interlayer magnetic coupling Iinteractions of two ferromagnetic layers by spin polarized tunneling," *Phys. Rev. Lett.*, vol. 89, no. 10, pp. 107206–1, 2002.

[139] P. Matl, N. P. Ong, Y. F. Yan, Y. Q. Li, D. Studebaker, T. Baum, and G. Doubinina, "Hall effect of the colossal magnetoresistance manganite $La_{1-x}Ca_xMnO_3$," *Phys. Rev. B*, vol. 57, no. 17, pp. 10248–10251, 1998.

[140] J. W. Ye, Y. B. Kim, A. J. Millis, B. I. Shraiman, P. Majumdar, and Z. Tesanovic, "Berry phase theory of the anomalous Hall effect: Application to colossal magnetoresistance manganites," *Phys. Rev. Lett.*, vol. 83, no. 18, pp. 3737–3740, 1999.

[141] S. H. Chun, M. B. Salamon, Y. Lyanda-Geller, P. M. Goldbart, and P. D. Han, "Magnetotransport in manganites and the role of quantal Phases: Theory and experiment," *Physical Review Letters*, vol. 84, no. 4, pp. 757–760, 2000.

[142] W.-T. Hou, J.-X. Yu, M. Daly, and J. Zang, "Thermal driven topology in chiral magnets," *Phys. Rev. B*, vol. 96, p. 140403(R), 2017.

[143] S. H. Chun, M. B. Salamon, Y. Tomioka, and Y. Tokura, "Breakdown of the lattice polaron picture in $La_{0.7}Ca_{0.3}MnO_3$ single crystals," *Phys. Rev. B*, vol. 61, pp. R9225–R9228, Apr 2000.

[144] S. Thomas, B. Kuiper, J. Hu, J. Smit, Z. Liao, Z. Zhong, G. Rijnders, A. Vailionis, R. Wu, G. Koster, and J. Xia, "Localized control of Curie temperature in perovskite oxide film by capping-layer-induced octahedral distortion," *Phys. Rev. Lett.*, vol. 119, no. 17, p. 177203, 2017.

[145] L. Klein, J. S. Dodge, C. H. Ahn, J. W. Reiner, L. Mieville, T. H. Geballe, M. R. Beasley, and A. Kapitulnik, "Transport and magnetization in the badly metallic itinerant ferromagnet $SrRuO_3$," *J. Phys. Condens. Matter*, vol. 8, no. 48, pp. 10111–10126, 1996.

[146] P. B. Allen, H. Berger, O. Chauvet, L. Forro, T. Jarlborg, A. Junod, B. Revaz, and G. Santi, "Transport properties, thermodynamic properties, and electronic structure of $SrRuO_3$," *Phys. Rev. B*, vol. 53, no. 8, pp. 4393–4398, 1996.

[147] M. E. Fisher and J. S. Langer, "Resistive anomalies at magnetic critical points," *Phys. Rev. Lett.*, vol. 20, no. 13, pp. 665–668, 1968.

[148] X. Shen, X. Qiu, D. Su, S. Zhou, A. Li, and D. Wu, "Thickness-dependent metal-insulator transition in epitaxial $SrRuO_3$ ultrathin films," *J. Appl. Phys.*, vol. 117, no. 1, p. 015307, 2015.

[149] J. Xia, W. Siemons, G. Koster, M. R. Beasley, and A. Kapitulnik, "Critical thickness for itinerant ferromagnetism in ultrathin films of $SrRuO_3$," *Phys. Rev. B*, vol. 79, no. 14, p. 140407(R), 2009.

[150] Z. Fang, N. Nagaosa, K. S. Takahashi, H. Yamada, M. Kawasaki, and Y. Tokura, "The anomalous Hall effect and magnetic monopoles in momentum space.," *Science*, vol. 302, no. October, pp. 92–96, 2003.

[151] X. G. Wen, F. Wilczek, and A. Zee, "Chiral spin states and superconductivity," *Phys. Rev. B*, vol. 39, pp. 11413–11423, Jun 1989.

[152] S. Hyun and K. Char, "Effects of strain on the dielectric properties of tunable dielectric $SrTiO_3$ thin films," *Appl. Phys. Lett.*, vol. 79, no. 2, p. 254, 2001.

[153] M. Bonilla, S. Kolekar, Y. Ma, H. C. Diaz, V. Kalappattil, R. Das, T. Eggers, H. R. Gutierrez, M.-H. Phan, and M. Batzill, "Strong room-temperature ferromagnetism in VSe_2 monolayers on van der Waals substrates," *Nat. Nanotechnol.*, vol. 13, pp. 289–293, 2018.

[154] Z. Fei, B. Huang, P. Malinowski, W. Wang, T. Song, J. Sanchez, and W. Yao, "Two-Dimensional itinerant Ising ferromagnetism in atomically thin Fe_3GeTe_2," *arXiv:1803.02559*, 2018.

[155] Y. Deng, Y. Yu, Y. Song, J. Zhang, N. Wang, Y. Wu, and J. Zhu, "Gate-tunable room-temperature ferromagnetism in two-dimensional Fe_3GeTe_2," *arXiv:1803.02038*, 2018.

[156] Y. Machida, S. Nakatsuji, S. Onoda, T. Tayama, and T. Sakakibara, "Time-reversal symmetry breaking and spontaneous Hall effect without magnetic dipole order," *Nature*, vol. 463, no. 7278, pp. 210–213, 2010.

[157] C. Mann, D. West, I. Miotkowski, Y. P. Chen, S. Zhang, and C. K. Shih, "Mapping the 3D surface potential in Bi_2Se_3," *Nat. Commun.*, vol. 4, pp. 1–6, 2013.

[158] J. Dai, D. West, X. Wang, Y. Wang, D. Kwok, S. W. Cheong, S. B. Zhang, and W. Wu, "Toward the intrinsic Limit of the topological insulator Bi_2Se_3," *Phys. Rev. Lett.*, vol. 117, no. 10, pp. 31–33, 2016.

[159] J. Moon, N. Koirala, M. Salehi, W. Zhang, W. Wu, and S. Oh, "Solution to the hole-doping problem and tunable quantum Hall effect in Bi_2Se_3 thin Films," *Nano Lett.*, vol. 18, no. 2, pp. 820–826, 2018.

[160] F. Katmis, V. Lauter, F. S. Nogueira, B. A. Assaf, M. E. Jamer, P. Wei, B. Satpati, J. W. Freeland, I. Eremin, D. Heiman, P. Jarillo-Herrero, and J. S. Moodera, "A high-temperature ferromagnetic topological insulating phase by proximity coupling," *Nature*, vol. 533, no. 7604, pp. 513–516, 2016.

[161] C. Tang, C. Z. Chang, G. Zhao, Y. Liu, Z. Jiang, C. X. Liu, M. R. McCartney, D. J. Smith, T. Chen, J. S. Moodera, and J. Shi, "Above 400-K robust perpendicular ferromagnetic phase in a topological insulator," *Sci. Adv.*, vol. 3, no. 6, pp. 2–7, 2017.

[162] W. Luo and X. L. Qi, "Massive Dirac surface states in topological insulator/magnetic insulator heterostructures," *Phys. Rev. B*, vol. 87, no. 8, p. 085431, 2013.